

**MAGNESIUM DIBORIDE JOSEPHSON JUNCTIONS FOR
SUPERCONDUCTING DEVICES AND CIRCUITS**

A Dissertation
in Partial Fulfillment
of the Requirements for the Degree
DOCTOR OF PHILOSOPHY

By

Daniel Cunnane

August 2013

Thesis Examination Committee

Dr. Xiaoxing Xi, Chair, Temple University Physics Department

Dr. Ke Chen, Co-Chair, Temple University Physics Department

Dr. Maria Iavarone, Temple University Physics Department

Dr. Svetlana Neretina, External Examiner, Temple University Mechanical Engineering
Department

ABSTRACT

Superconductivity in magnesium diboride (MgB_2) was first discovered in 2001. It is unique in that it has two superconducting gaps. The transition temperature of 39 K exceeded the maximum transition temperature thought to be possible through phonon mediated superconductivity. Through the study of MgB_2 , a general paradigm is being formulated to describe multi-gap superconductors. The paradigm includes inter-band and intra-band scattering between the gaps which can cause a smearing of the gap parameter over a distribution instead of a single value. Although each gap is individually thought to be well described by the BCS theory, the interaction between the two gaps causes complications in describing the overall superconducting properties of MgB_2 . The focus of this work was to lay the groundwork for an MgB_2 -based Josephson junction technology. This includes improving on a previously established baseline for all- MgB_2 Josephson junctions, utilizing the Josephson Effect to experimentally verify a model pertaining to the two-gap nature of MgB_2 , specifically the magnetic penetration depth, and designing, fabricating, and testing multi-junction devices and circuits.

The experiments in this work included fabrication of Josephson Junctions, DC superconducting quantum interference devices (SQUIDs), Josephson junction arrays, and a rapid single flux quantum (RSFQ) circuit. The junctions were all made utilizing the hybrid physical-chemical vapor deposition method, with an MgO sputtered barrier. The current process consists of three superconducting layers which are patterned using

standard UV photolithography and etched with Ar ion milling. There were SQUIDS made with sensitivity to magnetic fields parallel to the film surface, which were used to measure the inductance of MgB₂ microstrips. This inductance was used in design of more complicated devices as well as in calculating the magnetic penetration depth of MgB₂, found to be about 40 nm at low temperature, in good agreement with a previously published theoretical model. Planar-type DC SQUIDS were also made to present the feasibility of the technology for application purposes. The large voltage modulation of over 500 μ V at 15 K for these devices along with operation up to 37 K shows that MgB₂ is a potential replacement for low temperature devices. The junction series arrays were fabricated with 100 junctions of equal size to present the ever-increasing robustness of the technology. The devices served well to measure the large property spread associated with these junctions and have been well established as a diagnostic tool for improving this spread. The culmination of this work was a basic RSFQ toggle flip flop circuit. A DC measurement of these circuits yielded digital operation up to 180 GHz at low temperature and about 63 GHz at 20 K. This is not yet near the potential limit of MgB₂ established by the value of the superconducting gap parameters, but a huge success in showing that MgB₂ is a viable option for pursuing superconducting digital electronics suitable for low power, cryogen-free operation.

ACKNOWLEDGMENT

I would like to show my appreciation to all the people in my life who are in some way responsible for helping me to complete this work. First I would like to thank my advisor, Dr. Xiaoxing Xi, whose experience, guidance, and persistence kept me on track for a very successful graduate career. I would also like to thank my co-advisor, Dr. Ke Chen, who gave me so much of his time and knowledge over the years. His in-depth knowledge of superconducting devices and exquisite eye for details has helped me to create research which I never thought myself capable to produce. I would also like to thank all the other members of the research group who have made my graduate experience so productive. These members include Dr. Chenggang Zhuang, Mr. Alex Krick, Mr. Wenqing Dai, Mr. Teng Tan, Mrs. Qingyu Lei, Mrs. Maryam Golalikhani, and Mr. Elias Galan. I am eternally grateful to Mr. Edward Kaczanowicz for his generous help and wealth of knowledge about vacuum systems and Mr. Matthew M^cCormick for his willingness to help in machining any time he was able. I would like to thank Mr. Richard J. Harris for his electronics expertise and vast overstock of electronic components.

Though I could never express enough gratitude, I would like to thank my parents. My father, Mr. Brian Cunnane, has never doubted me in my entire life, even when given sufficient criterion, and has given me motivation at every step of my life. My mother, Mrs. Adrian Cunnane, has blindly and unconditionally given me the love I needed on a daily basis. I would also like to thank my sister, Ms. Erin Cunnane, who has been a

source of inspiration to me both in difficult times as well as in good times. I would like to express my appreciation to all of my friends. More specifically, I would like to thank Mr. Charles Swartz, who has spent countless hours listening to my frustrations throughout graduate school. I would also like to thank Mr. Sandip Shah and Mr. John Gentile, who have been there to pull me away from work when I needed it most and always seemed to give me a reason to have a good time. Of course, none of this work would have been successful if it were not for my fiancé Daiya. Her love and companionship has provided me with an unlimited source of happiness, even in my most trying times.

TABLE OF CONTENTS

	Page
ABSTRACT.....	i
ACKNOWLEDGEMENTS.....	iii
LIST OF FIGURES	viii
LIST OF TABLES.....	xiii
CHAPTER 1: INTRODUCTION	
1.1 Superconductivity.....	1
1.2 Magnesium Diboride.....	8
1.3 Josephson Junctions	12
1.4 Resistively and Capacitively Shunted Junction Model and Analogs	18
1.5 Applications of Josephson Junctions.....	21
CHAPTER 2: EXPERIMENTAL TECHNIQUES	
2.1 Hybrid Physical-Chemical Vapor Deposition of Magnesium Diboride	28
2.2 Magnetron Sputtering.....	33
2.3 Atomic Force Microscopy, X-ray Diffractometry, and Scanning Electron Microscopy	35
2.4 Microfabrication Techniques	38

2.5 Low Temperature Measurement Systems	40
2.6 Electronics and Computer Interface	46
CHAPTER 3: MAGNESIUM DIBORIDE JOSEPHSON JUNCTIONS AND RELATED DEVICES	
3.1 MgB ₂ Josephson Junctions.....	48
3.2 MgB ₂ Planar Washer-Type DC SQUIDS	64
3.3 MgB ₂ Josephson Junction Series Array	70
CHAPTER 4: STUDY OF COMPONENTS FOR MAGNESIUM DIBORIDE RSFQ DIGITAL CIRCUITS	
4.1 Introduction	77
4.2 Experiment	78
4.3 Results and Discussion.....	80
4.4 Conclusion.....	90
CHAPTER 5: PENETRATION DEPTH MEASUREMENTS OF MGB ₂ USING JOSEPHSON JUNCTIONS AND DC SQUIDS	
5.1 Introduction	91
5.2 Experiment	93
5.3 Results and Discussion.....	94
5.4 Conclusion.....	104

CHAPTER 6: A MAGNESIUM DIBORIDE RSFQ TOGGLE FLIP FLOP CIRCUIT

6.1 Introduction	105
6.2 Experiment	107
6.3 Results and Discussion.....	110
6.4 Conclusion.....	117

CHAPTER 7: CONCLUSION AND FUTURE WORK

7.1 Conclusion	118
7.2 Future Work	121

REFERENCES	124
------------------	-----

APPENDIX A: TRILAYER PROCESS.....	133
-----------------------------------	-----

LIST OF FIGURES

Figure	Page
1.1. Kamerlingh Onnes' data showing the transition of Mercury to the superconducting state at 4.2 K (ref 1).....	2
1.2. Magnetic field lines for a material in the normal state (left) and in the superconducting state(right).....	3
1.3. Density of states of quasi-particles in a superconductor from Ref. 3. Dotted line shows the density of states for electrons in a normal metal.....	5
1.4. The electron density of states of MgB ₂ measured by scanning tunneling microscopy from ref. 15.....	8
1.5. The Fermi surface of MgB ₂ . Blue and green region represents the 3D π band while red and orange region represents the quasi-2D σ band (ref. 13).....	10
1.6. The comparison of calculated energy gap distribution by H.J. Choi, et al (top) to the experimental tunneling spectroscopy by K. Chen, et al (ref. 22).....	11
1.7. Schematic drawing of a typical sandwich-type Josephson junction with measurement points.....	12
1.8. Schematic diagram of how a magnetic field is introduced to a sandwich-type Josephson junction.....	15
1.9. Ideal curve of a square Josephson junction in an applied magnetic field.....	16
1.10. The RCSJ Model equivalent circuit.....	18
1.11. Picture of the washboard analog. It can be described as a ball rolling down a decline with many small oscillations.....	20
1.12. A schematic of a DC SQUID from ref. 40.....	21
1.13. The IV characteristic of a DC SQUID at the minimum (dotted line) and maximum (solid line) of the voltage modulation.....	23
1.14. Schematic diagram of an RSFQ pulse splitter. The loops represent inductors and the crosses represent Josephson junctions.....	26
2.1. Mg-B phase diagram. Growth region is indicated by "Gas + MgB ₂ ".	29

2.2. Set-up for the HPCVD process.	30
2.3. Photograph of the HPCVD system.	31
2.4. Resistivity versus temperature for a 120 nm MgB ₂ film grown on SiC substrate.	32
2.5. Photograph of the DC Sputtering system used to deposit Cr, Au, Mo, and Nb.	34
2.6. X-ray diffraction results for MgB ₂ film on SiC substrate. The existence of the 001 and 002 peaks imply epitaxial growth along the <i>c</i> -axis direction.	36
2.7. Atomic Force Microscope image of MgB ₂ film. The left image is a 2 μm scan and the left image is a 20 μm scan. The hexagonal structures are MgB ₂ grains. The peak to valley height across the line in the left image has a maximum of 5 nm.	37
2.8. Scanning electron microscope image of square junctions with length 5 μm (left) and 2 μm (right).	38
2.9. Photograph of the Karl Suss MJB-4 Mask Aligner. Yellow tinted light is to avoid exposing the photoresist.	39
2.10. Photograph of the Quantum Design PPMS system. Empty rack on the left hand side can be used to interchange measurement electronics.	41
2.11. Photograph of the Janis Research pulse tube Cryocooler inside of dual layer of magnetic shielding. Connections directly to the unit avoid unwanted ground loops.	43
2.12. Temperature verse time comparison of closed loop PID controller and a manual output heater. Similarities in period and amplitude indicate that modulation is a product of gas compression.	44
2.13. Voltage across a DC SQUID verse time comparison of PID controller and manual output heater. Similarities indicate the temperature dependence, not flux from the heater, is responsible for modulation.	45
3.1. Optical image of an MgB ₂ /Native Oxide/Pb Junction.	50
3.2. AFM comparison of 100nm-thick MgO thin films on SiC substrate using reactive sputtering of an Mg target (left), and RF sputtering of an MgO target (right). Scan size is 20 μm for both images.	52
3.3. IV characteristics of a MgB ₂ /Native Oxide/Pb junction (top), MgB ₂ /Native Oxide/Nb (middle), and MgB ₂ /MgO/MgB ₂ (bottom) Josephson Junction.	54
3.4. Conductance curve of a MgB ₂ /Native Oxide/Pb junction (top), MgB ₂ /Native Oxide/Nb (middle), and MgB ₂ /MgO/MgB ₂ (bottom) Josephson Junction.	55

3.5. Temperature dependence of the critical current of a MgB ₂ /MgO/MgB ₂ Josephson junction.....	57
3.6. Magnetic field dependence of an MgB ₂ /Native Oxide/Pb junction.....	59
3.7. Magnetic field dependence of an MgB ₂ /Native Oxide/Nb junction. Dashed line depicts a theoretical fit.....	59
3.8. Magnetic field dependence of an MgB ₂ /MgO/MgB ₂ junction. Dashed line depicts a theoretical fit.....	60
3.9. Comparison of MgB ₂ /MgO/MgB ₂ Josephson junctions before (bottom) some process design changes and after (top).....	63
3.10. Optical image of a washer-type DC SQUID. The scale of the whole device (left) can be seen by the 0.1 × 0.1 mm square at the center. The scale of the zoomed in image (right) can be seen by the circular junctions with 8 μm diameter.....	66
3.11. IV characteristic of a working planar-type DC SQUID with and without flux through the loop.....	67
3.12. Voltage modulation of the planar-type SQUID referred to in Fig. 3.10.....	69
3.13. The IV characteristic of a 100-junction array. Inset shows a larger voltage scale with an equal current scale.....	71
3.14. dV/dI verse current for the 100-junction array described in Fig. 3.12. Each vertical spike indicates a junction transition. (Note the logarithmic scale).....	73
3.15. dV/dI verse current for the 100-junction array described in Fig. 3.12. The array has been measured as 4 sub-arrays with the number of junctions in each sub-array indicated.....	75
3.16. A histogram generated from the data collected using the dI/dV curves in Fig. 3.15.....	76
4.1. Temperature dependence of the $I_c R_n$ product for a typical MgB ₂ Josephson Junction.....	81
4.2. Parameter spreads of MgB ₂ Josephson Junctions from a single chip after the introduction of a superconducting wiring	82
4.3. Voltage modulation of an MgB ₂ DC SQUID using the microstrip to generate the field. Inset shows IV curves for maximum and minimum flux in the loop using an external field.	84

4.4. Temperature dependence of L_{sq} for two devices with different thickness insulating layer. Triangles show data from a chip with 45nm of MgO and circles show data from a chip with 70nm of MgO.....	85
4.5. Temperature dependence comparison of different materials with good potential for MgB ₂ devices.....	86
4.6. Resistivity comparison at 4.2 K for different growth parameters of Mo. Black squares and red circles represent depositions at 0.01 and 0.02 mbar Ar partial pressure.....	87
4.7. Resistance vs Temperature of an MgB ₂ film as grown on top of a Mo substrate.....	89
4.8. IV curve of MgB ₂ /Mo intersection for <i>ex situ</i> grown Mo and <i>in situ</i> grown Mo after ion milling through the native oxide.....	89
5.1. The critical current of an MgB ₂ /Native Oxide/Nb junction modulated by applied magnetic field (solid line) fitted by a theoretical fit with $\lambda = 37$ nm (dotted line). Inset shows a schematic of the junction in an external magnetic field \vec{B}	95
5.2. (left) Schematic and (right) optical image of DC SQUID.....	98
5.3. Fabrication process of a SQUID.....	98
5.4. Voltage across a DC SQUID modulated by microstrip current at 3.2 K. The SQUID is biased at various current from 0.4 mA to 2 mA.....	100
5.5. Temperature dependence of normalized inverse-squared penetration depth from the SQUIDs measurement compared with the theory proposed by Golubov <i>et al.</i> for the clean (dashed line) and dirty (dashed double dotted line) limits in the <i>c</i> -axis and dirty limit (dashed-dotted line) in the <i>ab</i> -axis. Also plotted is the result of a mutual inductance measurement (solid line) on a 20 nm-thick MgB ₂ film.....	101
6.1. (top) Optical image and (bottom) schematic diagram of the TFF circuit. The junction J ₁ is circled in both by a dashed circle and the interferometer loop is circled by a dotted circle.....	107
6.2. (left) Voltage modulation across J ₁ and J ₂ at different temperatures and constant current bias as a current is scanned across the inductor L ₁ . (right) Temperature dependence of the inductance for L ₁ and L ₅ calculated from the period of voltage oscillations. Dotted line shows expected dependence.....	109
6.3. Input voltage V_{in} and twice the output voltage $2V_{out}$ versus input current I_{in} for (top) Circuit A at 3.2 K, and (bottom) Circuit B at 12.5 K.....	111

6.4. Difference $2V_{\text{out}} - V_{\text{in}}$ for Circuit B (left) at 8, 12, 15, and 20 K, all biased optimally; and (right) at 20 K and $I_{\phi} = 260 \mu\text{A}$ for $I_{b2} = 600, 640, 690,$ and $740 \mu\text{A}$	113
6.5. $2V_{\text{out}}$ versus I_{b2} for different operating frequencies ranging from about 10 GHz ($V_{\text{in}} = 0.021 \text{ mA}$) to 50 GHz ($V_{\text{in}} = 0.103 \text{ mA}$). Shaded area shows the region of operation.....	116
A.1. First lithography step mask patterns.....	137
A.2. Second lithography step mask pattern.....	138
A.3. Third and final lithography step mask patterns.....	140

LIST OF TABLES

Table	Page
5.1. Penetration depth of MgB_2 calculated from 12 square-shaped junctions of different length and top electrode materials.....	97

CHAPTER 1

INTRODUCTION

1.1 Superconductivity

Superconductivity was discovered in 1911 by Kamerlingh Onnes[1]. His breakthrough in liquefying helium allowed for temperatures in single digits on the Kelvin scale. As a result he found that Mercury became a perfect conductor at 4.2 K as his results show in Fig. 1.1. Soon after, many other metals showed this perfect conductivity below a specific critical temperature, T_c , which is material dependent. The discovery led to over a century of outstanding physics and a discretely new field.

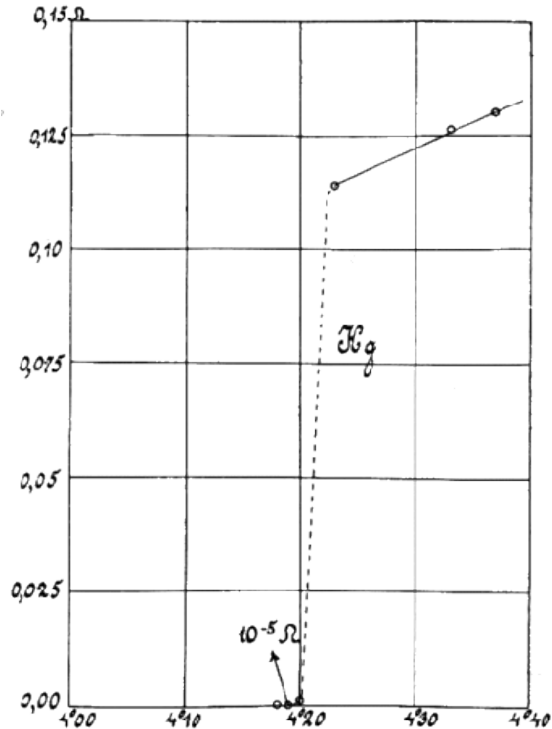


Figure 1.1. Kamerlingh Onnes' data showing the transition of Mercury to the superconducting state at 4.2 K (ref. 1).

The next big break in superconductivity came in 1933 when it was discovered that a magnetic field is expelled from normal metal as it transitions into the superconducting state. The phenomenon known as the meissner effect [2] changed the idea of superconductivity for the first, but certainly not the last time. Until this point a superconductor could be wholly described as a perfect conductor. The Meissner effect contradicted this idea because, though a perfect conductor would exclude a magnetic field, it would not expel it. Instead a perfect conductor would trap the pre-existing field

flux inside [3]. Fig.1. 2 shows the magnetic field lines about a sphere when the material is in both the normal and the superconducting state.

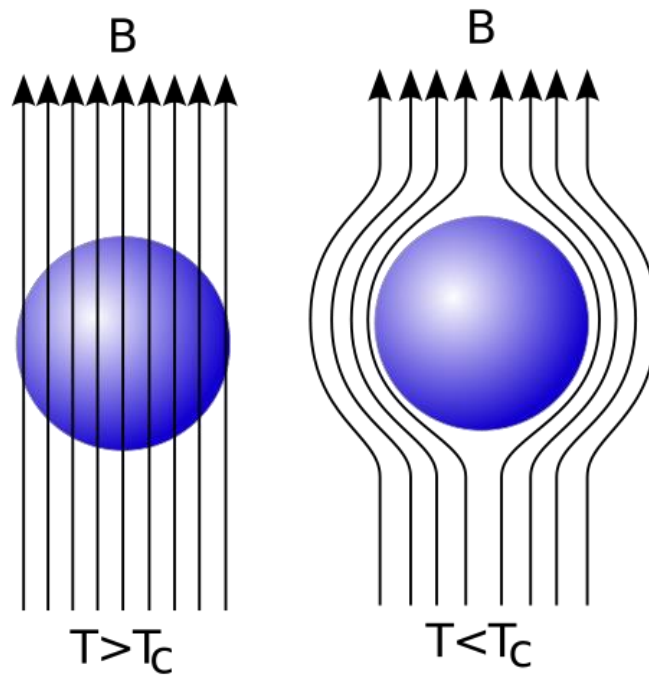


Figure 1.2. Magnetic field lines for a material in the normal state (left) and in the superconducting state(right).

The first theory to describe superconductivity was introduced in 1935 in the form of the London Equations [4]. The basic idea was to start with the Drude model of free electrons, which accurately describes Ohm's law, and include a superconducting electron density of particles with an infinite time constant[3]. The result is two distinct equations

which describe the local electrodynamics associated with superconductivity. The magnetic penetration depth, λ_0 , of a superconductor was first introduced by these equations.

By the end of the 1950's superconductivity was all but explained from a theoretical standpoint. In 1950, Ginzbergh and Landau introduced a characteristic length which is temperature dependent[5]. In 1953, Pippard introduced the not unrelated coherence length at low temperature[6]. Finally in 1957, the microscopic theory of superconductivity was introduced by Bardeen, Cooper, and Schreiffer[7]. In the BCS model, the superconducting electrons could be described by a single wave function including a pair of electrons, known as a cooper pair. The wave function consists of two parts, the spatial part and the phase, θ . It is energetically favorable for the electrons near the Fermi surface to pair together which leaves an energy gap in the electron density of states. The gap coincides exactly with the pairing energy of the electrons and the BCS theory describes this gap as

$$\Delta = \frac{\hbar\omega_D}{\sinh[1/N(0)V]} \approx 2\hbar\omega_D e^{-1/N(0)V} \quad (1.1)$$

Where ω_D is the Debye frequency, $N(0)$ is the density of states at the Fermi surface in the normal state and V describes the bonding energy. Fig.1.3 shows the density of quasi-particle states for a superconductor at $T=0$ K. All states below this gap energy are empty because these electrons are paired. Some smearing of the gap will occur with an increase in temperature.

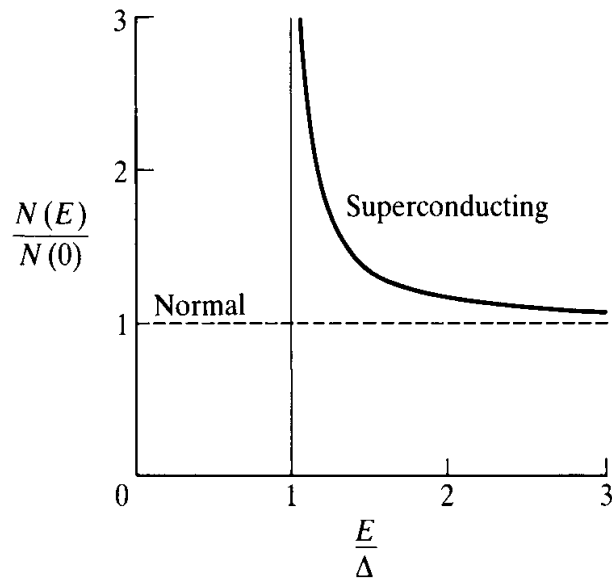


Figure 1.3. Density of states of quasi-particles in a superconductor from Ref. 3. Dotted line shows the density of states for electrons in a normal metal.

The most basic description of superconductivity at this point was that a single electron moved through a positively charged lattice and displaced it slightly shrinking the lattice spacing locally. The first electron moved away from the region before any real interaction took place but the smaller lattice spacing increased the charge in that region which in turn attracted a second electron. This second electron would then be bonded to the first as one moved in the other's positively charged wake. The distance between these two paired electrons is defined as the coherence length by Pippard at low temperature and

Ginzberg and Landau called it the characteristic length for temperatures closer to the T_c of a specific material.

During this time, another idea came about which theorized the flaws in perfect diamagnetism of superconductivity. In 1956, Abrikosov expanded on the work of Ginzberg and Landau to describe a situation where the penetration depth and the GL characteristic length had a relationship different than that described by Ginzberg and Landau[8]. This became known as Type II superconductivity. Though both type I and type II superconductors had a thermodynamic breakdown field H_c . A type II superconductor also contained a mixed state above some lower critical field H_{c1} . In this mixed state, there were regions of normal metal, known as vortices, where the field could penetrate.

The BCS theory satisfied all conditions of superconductivity until the discovery of high temperature superconductors in 1986[9]. The mechanism of superconductivity for these materials such as YBCO, has yet to be fully explained. It was the temperature dependence of the penetration depth that helped lead to the idea that the pairing symmetry was d-wave instead of the previous s-wave symmetry associated with the phonon interactions [10]. The attraction of these superconductors, specifically YBCO, was the critical temperature above the boiling point of liquid N_2 , which allowed operation without the expense of liquid He.

Magnesium Diboride (MgB_2) proved to be a curve ball to the superconducting community with the discovery of its superconductivity in 2001[11]. The common

metallic compound was found to have a T_c at 39 K. It also proved to be the first superconductor with multiple gaps[12, 13]. The physics surrounding MgB_2 became very popular in the last years of the first century of superconductivity. Since then, a new class of superconductors has been found in Iron-based materials which seem to have multiple gaps and a T_c up to 55 K[14].

Practical applications of superconductors have kept their popularity up despite the low temperature drawback associated with them. Applications of superconductors include large scale power transmission cables, superconducting high field magnets, transition edge sensors for radio astronomy and single photon detection, ultra-low magnetic field sensors for medical applications, and digital electronics.

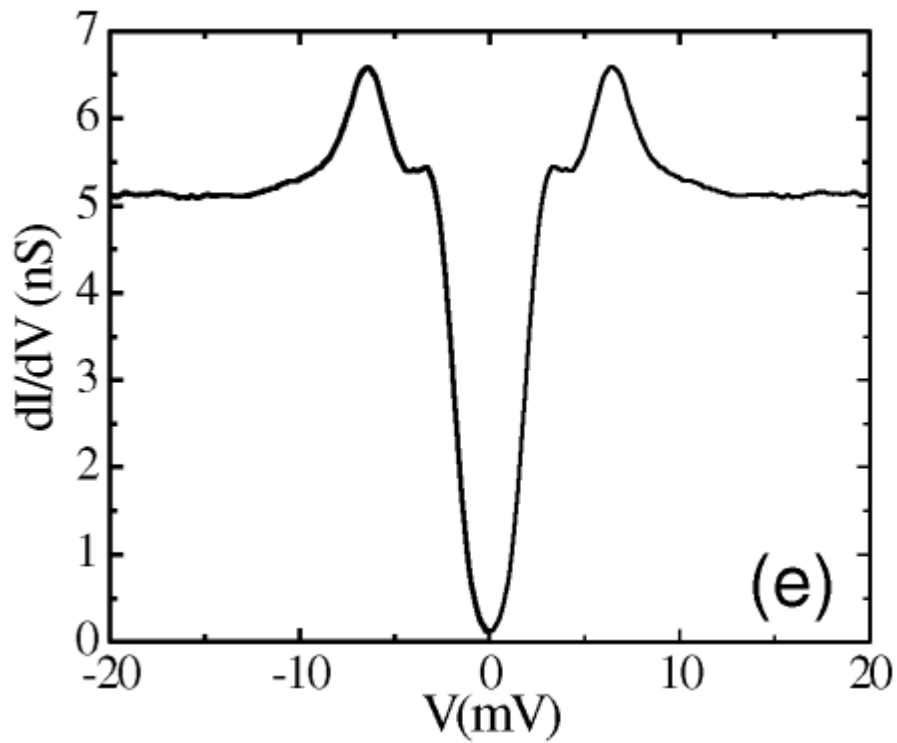


Figure 1.4. The electron density of states of MgB_2 measured by scanning tunneling microscopy from ref. 15.

1.2 Magnesium Diboride

Magnesium Diboride (MgB_2) is a simple metallic compound with a crystal structure consisting of hexagonal boron planes separated by magnesium atoms above the center of each hexagon. The superconductivity originates in both the σ and π bands of the boron electronic structure. This leads to two distinct energy gaps with values of about 7.1 meV and 2.1 meV respectively. Figure 1.4 shows a clear picture of the density of states of

MgB₂ from a Scanning Tunneling Microscope experiment[15]. The existence of the two gaps is also shown with experiments on the specific heat [16] as well as Raman spectroscopy [17]. The high T_c of about 39 K and the fact that superconductivity in MgB₂ is mediated by electron-phonon coupling make it very desirable for superconducting applications. Though the properties of MgB₂ still seem well described by the BCS theory[18-20], the two gaps and the interactions between them[21], make pinpointing the exact parameters such as the superconducting gaps, Δ_{σ} and Δ_{π} , the coherence length, ξ_0 , and the magnetic penetration depth, λ , controversial. A lot of the controversy comes from a variance of MgB₂ samples used in early measurements, but there is still difficulty in determining how each band gap contributes to the overall picture. Chapter 5 of this thesis goes into details of measuring the penetration depth of MgB₂.

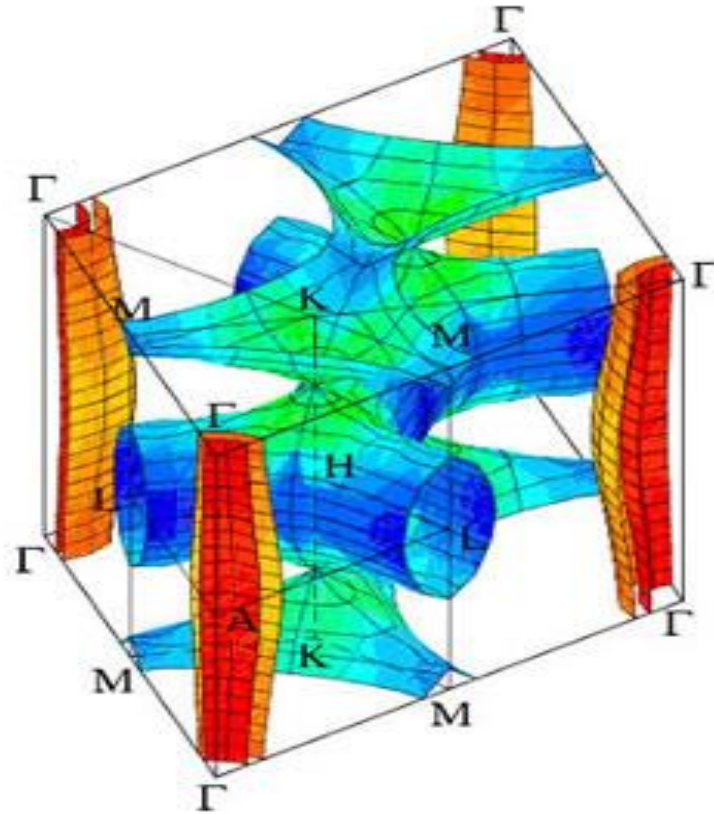


Figure 1.5. The Fermi surface of MgB_2 . Blue and green region represents the 3D π band while red and orange region represents the quasi-2D σ band (ref. 13).

A theoretical analysis has shown that scattering between the bands leads to a distribution of the energy gaps as opposed to the single value associated with classical superconductors. These calculations began with a beautiful depiction of the Fermi surface shown in Fig. 1.5[13]. The quasi-2D superconducting σ band is shown by the concentric cylinder-like shapes in the corners and the center depicts the 3D π band. An experimental study using tunnel junctions has further verified this idea[22]. Figure 1.6 compares the

numerical calculations of the gap conducted by Choi, et al, along with the experimental results from Chen, et al[22].

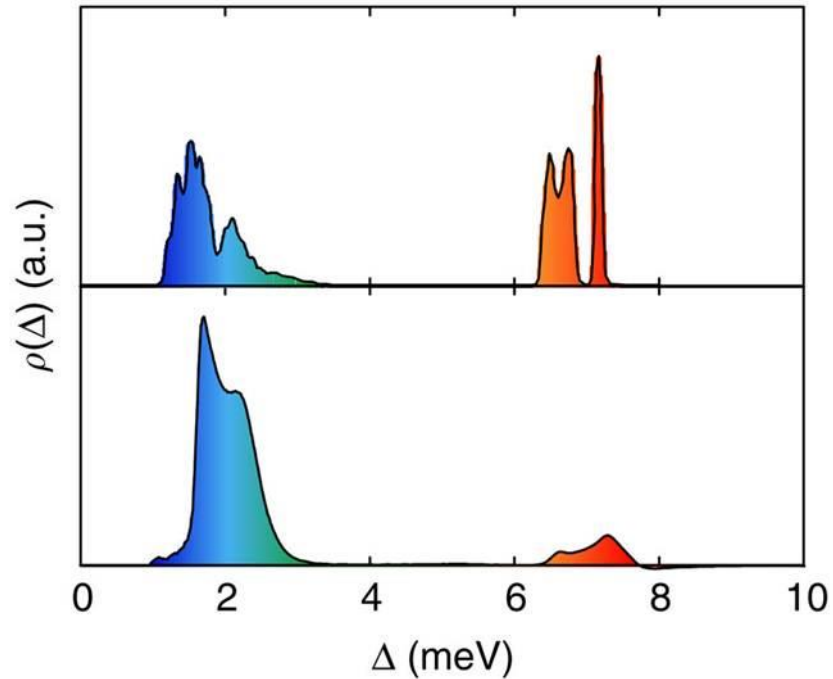


Figure 1.6. The comparison of calculated energy gap distribution by H.J. Choi, et al (top) to the experimental tunneling spectroscopy by K. Chen, et al (ref. 22).

Many studies have been done to obtain the anisotropic properties of MgB₂ like the penetration depth or upper critical field. Vortex imaging done by Eskildenson, et al shows a factor of just 1.2 taken from the ratio of the major axis to the minor axis of the vortex lattice[23]. The measurements of the magnetic penetration depth of MgB₂ have been particularly varied ranging from 40 nm to 150 nm [24] using the microwave resonator technique. Further reports of penetration depth measurements are done in chapter 5.

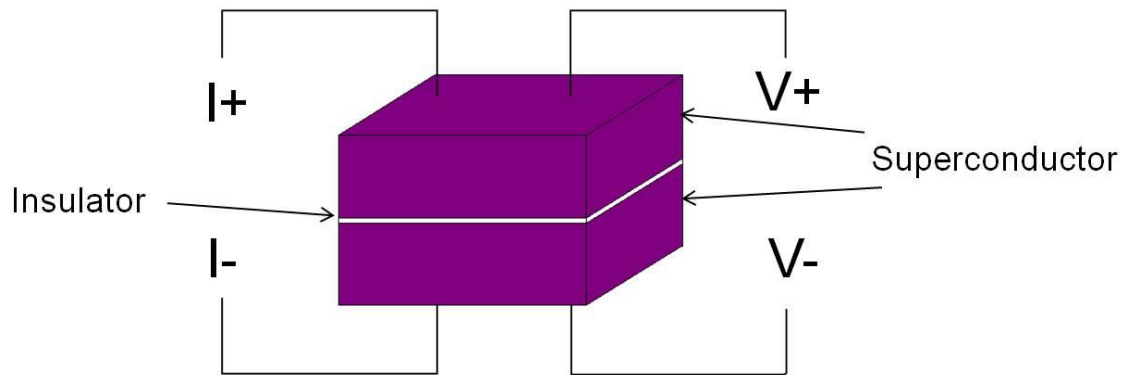


Figure 1.7. Schematic drawing of a typical sandwich-type Josephson junction with measurement points.

1.3 The Josephson Effect

The BCS theory paved the way for Brian Josephson to theorize that superconducting pairs could tunnel from one superconducting material to another across a weak link[25]. The theory was first experimentally verified by Anderson and Rowell one year later in 1963[26]. For this work, the structure will always be a sandwich type Josephson junction. In this case there are two superconducting electrodes separated by a barrier made up of either an ultra-thin insulator or a thin region of normal metal. Fig. 1.7 shows a schematic of a typical sandwich type junction. The supercurrent across the barrier is dominated by two relationships. The first, known as the DC Josephson effect states that the

supercurrent (a.k.a. Josephson current) is dependent on the change in the phase component of the cooper pair wave function. The relation is given by:

$$I_c = I_{c0} \sin(\theta_2 - \theta_1) \quad (1.2)$$

Where I_{c0} is the maximum super current and θ is the phase of the cooper pair wave function in either superconductor indicated by the subscript. The second relationship is called the AC Josephson effect. It makes sense to call this phase difference by a new variable $\theta_2 - \theta_1 = \phi$. Then the relation becomes:

$$\frac{\partial \phi}{\partial t} = 2eV/\hbar \quad (1.3)$$

Where V is the voltage across the barrier. The quantity $\hbar/2e = \Phi_0$ is a constant used often in superconducting devices and is coined the fluxon or flux quantum because the magnetic flux through a superconducting loop is quantized in integer quantities of Φ_0 [27]. These two relations have implications on how Josephson junctions will react with their environment, specifically in an external magnetic field.

There are a few different mechanisms which can support the Josephson Effect. The most controllable is a pure tunneling effect from a superconductor-insulator-superconductor (SIS) type junction. Here, both the superconducting pairs and the quasi-particles, or the single electrons filling the superconducting density of states, tunnel through a purely insulating barrier. Superconducting-normal metal-superconductor (SNS) type junctions utilize another common mechanism in the proximity effect[28], which is implemented by replacing the insulating barrier with a normal metal barrier. In this case

the superconducting pairs actually cross the normal metal region. This mechanism is used commonly with high temperature superconductor (HTS) materials as the anisotropic properties make pure tunneling nearly impossible to control. The thicker barriers used for SNS type junctions could prove to yield lower parameter spreads for applications where many junctions are required for a single sample, but also create complications on controlling temperature dependence of these junctions. Although a clear theoretical picture has been drawn for SNS junctions, this picture can easily be complicated if the junctions do not meet exact criterion such as barrier thickness not exceeding the mean-free path of electrons in the normal metal[29]. This can be particularly complicated if there is a large temperature dependence on the normal metal resistivity.

A third mechanism, not as common has particular relevance in this work. An insulating barrier with pinholes or any type of highly transparent regions can make up an overall weak-link across the barrier. The single particles will transfer energy across the barrier by means of Multiple Andreev Reflections (MAR) [30]. This mechanism can be identified by multiple peaks in the conductance curve of a junction occurring at integer divisions of $2\Delta/e$. This method of transport is has a disadvantage in controlling the J_c spread across the junctions, chips, and wafer to wafer runs, however a large benefit is achieved in very high values of J_c .

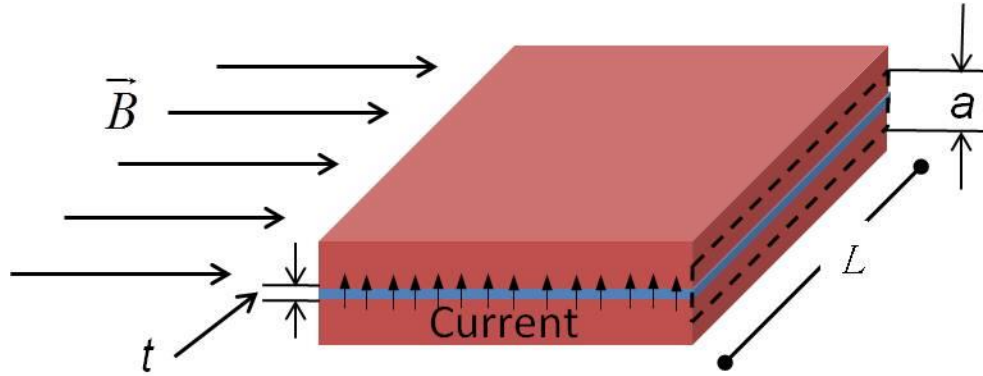


Figure 1.8. Schematic diagram of how a magnetic field is introduced to a sandwich-type Josephson junction.

For a Josephson junction in an external field which is perpendicular to the direction of current, gauge invariant phase difference, ϕ , across the barrier is related to the magnetic flux, Φ , through the barrier[31]. Fig. 1.8 shows a sandwich-type junction with the current and field direction as well as the area of flux defined by the dashed rectangle. Here the quantity a is not just the barrier thickness, t , but the sum of the barrier thickness and the magnetic penetration depth of each electrode, $a = \lambda_1 + \lambda_2 + t$. Integrating the maximum critical current density, J_c , over the entire junction area, using a field dependent flux gives the field dependence of the junction critical current, I_c . For the case of a rectangular or square junction the integration is less difficult and the field dependence becomes:

$$I_c(B) = I_{c0} \left| \frac{\sin(\pi\Phi/\Phi_0)}{\pi\Phi/\Phi_0} \right| \quad (1.4)$$

This is similar to the Fraunhofer pattern given by the single slit diffraction of light. An ideal case is shown in Fig. 1.9.

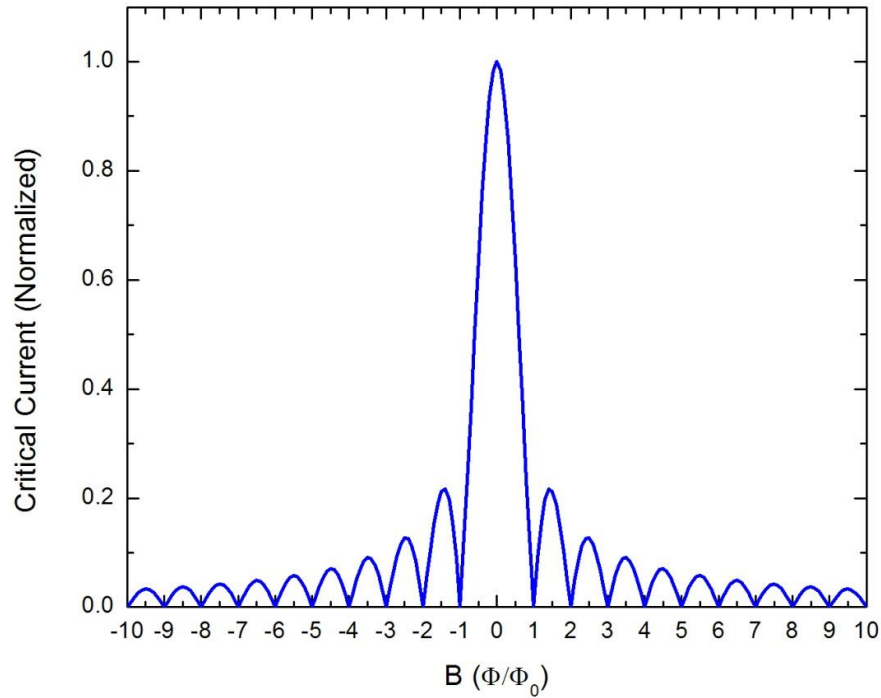


Figure 1.9. Ideal curve of a square Josephson junction in an applied magnetic field.

This field dependence is commonly used to verify the DC Josephson Effect and is also used to inspect the uniformity of J_c for a particular junction process. The more uniform the J_c , the closer the $I_c(B)$ curve will compare to the ideal case. It is important to point out that the penetration depth of the superconducting electrodes plays a large role in the period of oscillations of the I_c modulation. This fact has been used to calculate the

penetration depth, λ , of YBCO and compare it with theory [32]. The error in the calculation is not nearly as low as more typical methods of extracting the penetration depth, such as the microwave resonator technique [33], or magnetic force microscopy [34], and these other methods can measure thin films while this method requires device patterning and fabrication. The major advantage to using a Josephson junction to measure the penetration depth is that other methods can only measure a change in λ with temperature. Therefore known temperature dependence of the penetration depth is required for an exact λ value. The absolute value of the penetration depth can be found using the I_c modulation of a Josephson junction in a magnetic field, independent of temperature. A major drawback is that the electrode thickness can play a role in the measurement if the thickness is not much greater than the penetration depth. This can be compensated by using an effective λ which will make the period of oscillation:

$$\Delta H = \frac{\Phi_0}{L(\lambda_1 \tanh \frac{d_1}{2\lambda_1} + \lambda_2 \tanh \frac{d_2}{2\lambda_2} + t)} \quad (1.5)$$

Here L is the junction length, d_1 and d_2 are the film thickness, and λ_1 and λ_2 the penetration depth of the top and bottom electrode, respectively[35]. This is especially important for the case of MgB₂ as will be presented in chapter 5 of this work. The two gap nature of MgB₂ make a theoretical knowledge of the temperature dependence very controversial, and also make the value of λ very sample dependent.

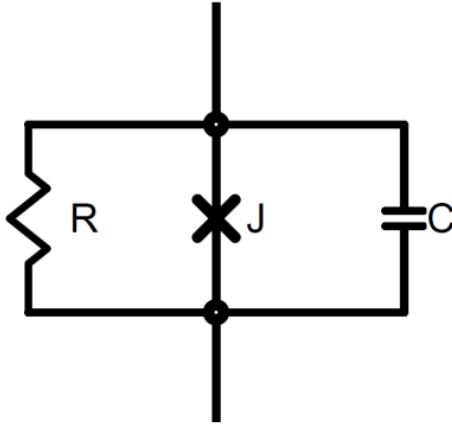


Figure 1.10. The RCSJ Model equivalent circuit.

1.4 The Resistively and Capacitively Shunted Junction Model and Useful Analogs

It is common to approximate a Josephson junction with the equivalent circuit shown in Fig. 1.10. This model takes advantage of the intrinsic capacitance and resistance of a junction by considering the three different devices in parallel. Summing the total current across these components gives:

$$I_{total} = G_n V + I_c \sin \phi + C \frac{dV}{dt} \quad (1.6)$$

Where G_n is the resistor conductance $1/R_n$ for the junction in the normal state, V is the voltage across the junction, and C is the capacitance of the junction. The term I_c refers to the zero field critical current. Using the AC Josephson relation (1.3.2) allows V to be

replaced with the phase change, ϕ . This yields a second order differential equation which is useful for characterizing junctions:

$$\frac{I_{total}}{I_c} = \beta_c \frac{d^2\phi}{dt^2} + \frac{d\phi}{dt} + \sin \phi \quad (1.7)$$

By rearranging constants, the new term $\beta_c = \left(\frac{I_c R_n}{\Phi_0}\right) (CR_n)$ called the Stewart-McCumber parameter[36-38] becomes a design parameter for specific applications. The value is defined by these two terms to show that β_c can be controlled by the junction capacitance as well as the normal resistance. The first term in the definition of β_c is a constant determined by the superconducting electrodes gap parameters, at least in the case of ideal tunneling. For most applications, hysteresis generated by the junction capacitance is undesirable. In this situation it is beneficial to lower the value of β_c to near unity (over-damped case). A sandwich-type Josephson junction in its most basic description is essentially a parallel plate capacitor, hence there is no way to significantly control the capacitance of the junction. The resistance, on the other hand, can be controlled easily with an external shunt resistor in parallel with the equivalent circuit. In low temperature superconductors this shunt resistor has been used to control β_c with fairly accurate precision [39].

The differential equation 1.4.2 has a mechanical analog in the damped driven oscillator.

$$M \frac{d^2\phi}{dt^2} + D \frac{d\phi}{dt} + mgl \sin \phi = T_a \quad (1.8)$$

Where M is the moment of inertia which is the analog of the capacitance, D is the damping constant which is the analog of conductance, and the angle ϕ is the analog of the pair wave function phase change which uses the same variable. This is useful in describing the physical results of some perturbation on a system of Josephson junctions, especially when talking about rapid single flux quantum (RSFQ) digital circuits, which utilize junctions and loops to achieve digital operations.

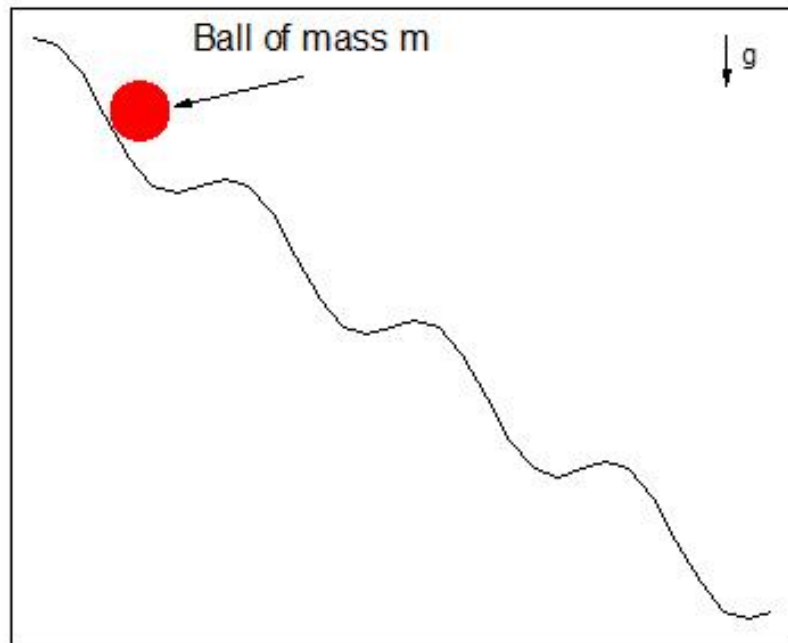


Figure 1.11. Picture of the washboard analog. It can be described as a ball rolling down a decline with many small oscillations.

Another analog which is useful when working with Josephson junctions is known as the washboard model. The equation of motion of a ball rolling down a hill with small oscillations, shown in Fig. 1.11[taken from ref. 31], can be put into the same form as the damped driven pendulum. In this case, the mass of the ball in gravity has some stored up energy which corresponds to the capacitance, and the drag on the ball is analogous to the resistance in a junction.

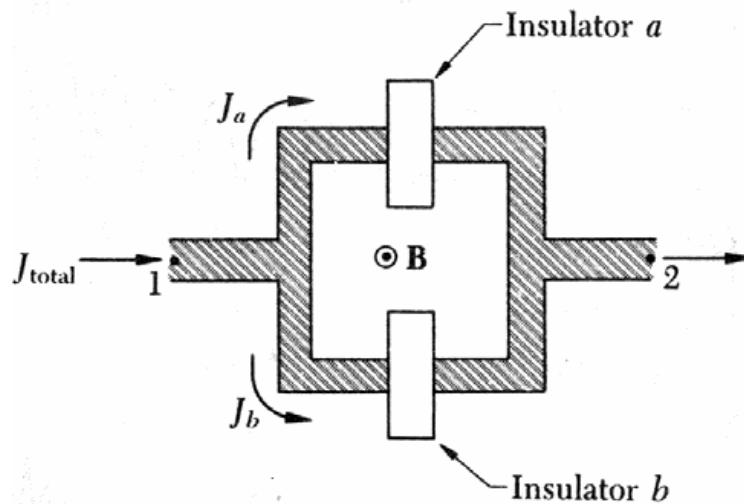


Figure 1.12. A schematic of a DC SQUID from ref. 40.

1.5 Applications Using Josephson Junctions

1.5.1 Superconducting Quantum Interference Devices

DC Superconducting quantum interference devices (DC SQUIDs) consist of two Josephson junctions in a parallel loop of inductance L . A schematic is shown Fig. 1.12 from ref [40]. A magnetic field through the loop will generate some current in the loop. If

a bias current is supplied across both junctions, then the total current through each junction will be the sum of the induced current and the applied bias. Notice that in the case of junction a, the two currents will add together and in the case of junction b, the currents will be in the opposite direction. This means that the induced current will have caused an effective phase change from the overall phase change across the loop. These two phases interfere and the total supercurrent through the device will be

$$I_{ctotal}^2 = (I_{c1} - I_{c2})^2 + 4I_{c1}I_{c2}\cos^2\left(\pi\Phi/\Phi_0\right) \quad (1.9)$$

This term has maxima at $\Phi/\Phi_0 = n$ and minima at $\Phi/\Phi_0 = n + 1/2$. This can be reflected in the voltage measured across the device. Fig. 1.13 shows an IV curve of a DC SQUID at both the integer value and half integer value of this flux ratio. It is evident that the voltage measured at the same bias point (above the critical current) will modulate with the critical current as seen from Fig. 1.13. In this way, a change in magnetic field can be measured by measuring the periodic voltage modulations of a DC SQUID biased just above the maximum I_c .

The usual design consideration of a SQUID is the unitless parameter

$$\beta_L = 2LI_c/\Phi_0 = 1 \quad (1.10)$$

L is the inductance of the SQUID loop, which usually requires other consideration, for example, the device sensitivity or focusing factor. The junction I_c is generally fitted to the inductance as long as the inductance is in a reasonable range.

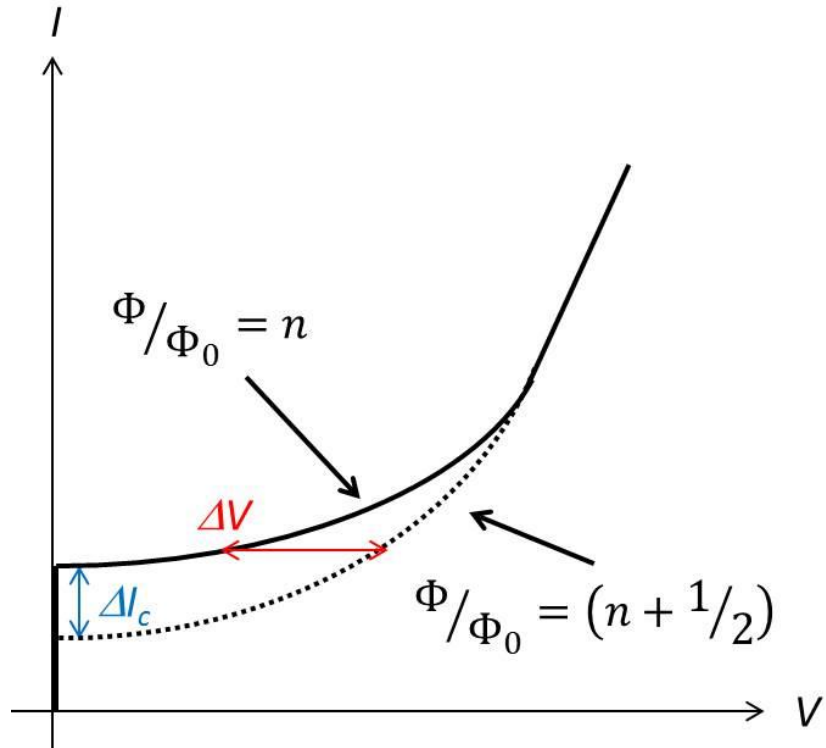


Figure 1.13. The IV characteristic of a DC SQUID at the minimum (dotted line) and maximum (solid line) of the voltage modulation.

1.5.2 Rapid Single Flux Quantum Circuits

Josephson junctions serve as the active components in RSFQ circuits. These superconducting integrated circuits (SICs) serve to emulate semiconducting digital devices with improved speed and decreased power consumption[41]. The dynamic

operation replaces high and low voltage binary representation of semiconducting circuits with the existence of a voltage pulse at a specific time, as compared to a clock signal. To consider a network of junctions working together to achieve some operation, it makes sense to first consider a single junction.

There are some stipulations as to the type of junction used in this technology. The small junction limit implies that the Josephson penetration depth, λ_J , must be much larger than the junction dimensions. Usually an order of magnitude here ensures that no field generated across the junction can have an effect on its operation. The junctions must also have no hysteresis. This of course makes sense as a double-valued voltage would be detrimental to digital operations. This is done by using an external resistive shunt to optimize β_c . Finally the junction parameters must be controllable. Although the parameter spreads are not as critical as semiconductor circuits, the better the overall spreads, the more complicated operations are achievable and repeatable.

Now we consider a significantly small RCSJ-like junction to be an analog to a damped driven pendulum. If the junction is biased near its critical current, this is the same as the pendulum oscillating close to the point that will cause it to flip over the top. A single external push, even with a small force, will push the pendulum over the top and it will return to its original state of oscillation near the flipping point. A short incoming pulse with small amplitude will have a similar effect on the junction. There will be a 2π flip in the phase change of the junction. The end result will be a reproduction of the incoming pulse.

In this way, it is possible to generate, amplify, split, and otherwise operate with these pulses. The DC voltage measured across a single junction would show oscillations in time with the oscillation frequency related to the voltage by the AC Josephson Effect. Therefore, a single junction can be used as a voltage controlled oscillator (VCO). For example, if the junction I_c is higher than the amplitude of the original pulse, the outgoing pulse will have an increased amplitude, where the additional energy comes from the constant bias current. Integrating the AC Josephson Effect yields a constant, which implies that the area under the curve of these pulses is always constant, as shown in equation 1.5.1.

$$\int V(t)dt = \Phi_0 \quad (1.11)$$

If the amplitude is increased, then the width of the pulse will be decreased. This is beneficial to increase the frequency of the pulses for operation. The AC Josephson Effect says also that the voltage across the junction corresponds to some frequency of oscillation or in this case pulses. In order to distinguish one pulse from the next, the space between pulses must be greater than the width of the pulses themselves. This means that increasing the amplitude increases the potential operating frequency by making pulses more discernible. The term for this device used to carry and amplify pulses is called a Josephson Transmission Line (JTL). The junction used to reproduce the pulse is impedance-matched to a microstrip inductor which will carry the pulse to the next RSFQ component. The inductance of the microstrip is another design parameter of RSFQ circuits.

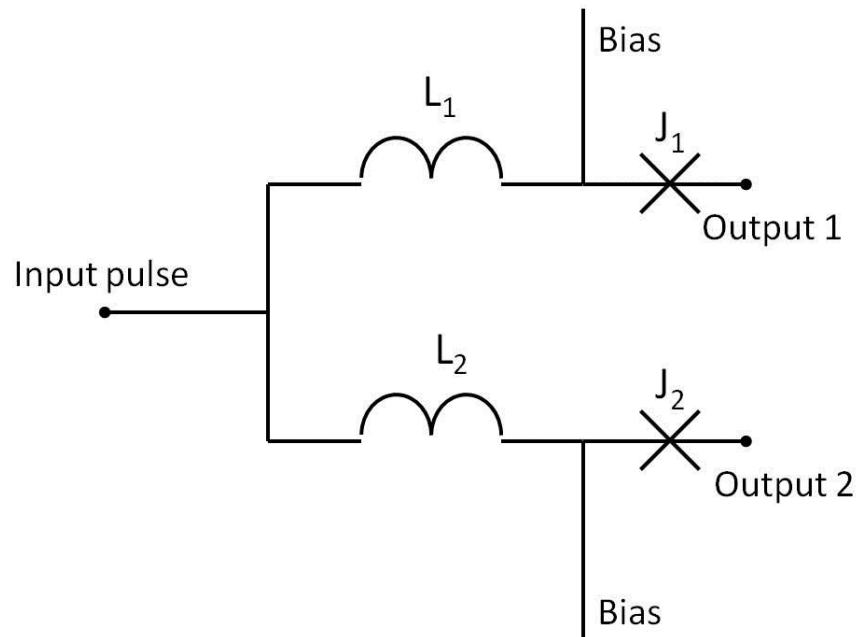


Figure 1.14. Schematic diagram of an RSFQ pulse splitter. The loops represent inductors and the crosses represent Josephson junctions.

Another elementary RSFQ cell is a pulse splitter. In this case the input of a single pulse is sent across two inductors as shown in figure 1.14. Then the pulses will enter the next junctions already biased near their respective I_c , causing them each to reproduce the pulse at two different outputs. An entire library has been established of RSFQ cells to perform a plethora of operations. It is common, when applying RSFQ technology to a new superconducting material or fabrication process, to first make a Toggle Flip Flop (TFF) circuit. This device can be measured without any DC/SFQ conversions, and shows the potential operating frequencies of a particular material or process. It consists of a

single junction, used as a pulse generator, a JTL, a pulse splitter which applies pulses to an interferometer. The interferometer is nothing more than a DC SQUID with inputs coming from both ends of a pulse splitter. When the interferometer loop has the proper inductance and the junctions have a designed I_c , the consecutive input pulses will only be reproduced at one of the two interferometer junctions. A subsequent pulse will trigger the other junction to have a 2π flip, and so on. This means that the frequency of pulses generated and supplied to the interferometer will be halved by measuring the output at a single junction inside the interferometer. If the DC voltage is measured, the AC Josephson Effect implies that the voltage will also be halved. The standard of RSFQ technology is set by a Nb process which has shown operation of a static voltage divider (TFF) up to 770 GHz[42]. Chapter 6 of this work will concentrate on the first MgB₂ TFF circuit and analysis.

CHAPTER 2

EXPERIMENTAL TECHNIQUES

2.1 Hybrid Physical-Chemical Vapor Deposition

In order to achieve high quality superconducting devices and circuits, it is necessary to first obtain high quality thin films. In the case of Nb and Nb compounds, DC sputtering has been successful in making smooth films with superconducting properties near the bulk values[43]. For the standard high temperature superconductor YBCO, films can be achieved by a pulsed laser deposition technique[44], E-beam evaporation[45], or a sputtering technique[46]. MgB₂ on the other hand, poses some issues for most methods of thin film growth. In the early years, there were attempts to make good films by a two-step process of annealing an Mg-B precursor film in an ambient magnesium atmosphere[47]. These films were a great achievement at the time, but still were not sufficient for Josephson devices or multilayer structures. The transition temperature was close to bulk, but not ideal like Nb or YBCO, and the residual resistivity ratio (RRR) less than 3 implied that the films were not very pure. Many other attempts at similar processes, both *ex situ* and *in situ* were made with varying degrees of success[48-50]. Other research led to a dual deposition of Mg and Boron using a rotating sample and sputtering sources[51-54], molecular beam epitaxy (MBE)[55-59], pulsed laser deposition[60-64], and E-beam evaporation[65, 66].

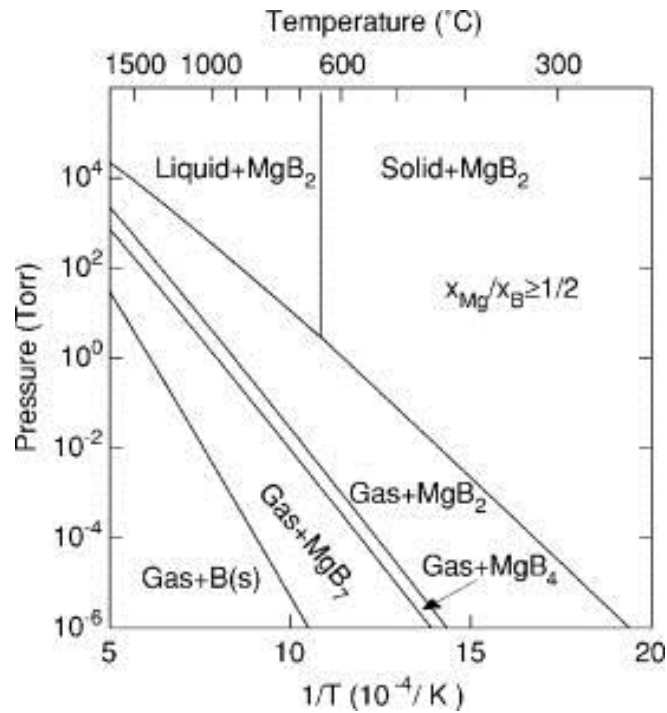


Figure 2.1. Mg-B phase diagram. Growth region is indicated by “Gas + MgB₂”.

Fig. 2.1 from ref [67] shows the magnesium vapor pressure versus temperature phase diagram for the correct ratio of Mg/B atoms. In order to ensure MgB₂ growth, the Mg vapor pressure must be sufficiently high, which is the main reason that other methods produce only satisfactory films at best. Hybrid physical-chemical vapor deposition (HPCVD) combines the physical evaporation of solid Mg with the high quality chemical vapor deposition of boron from Diborane (B₂H₆) gas[68]. The result is more than sufficient ambient Mg in the locality of the sample.

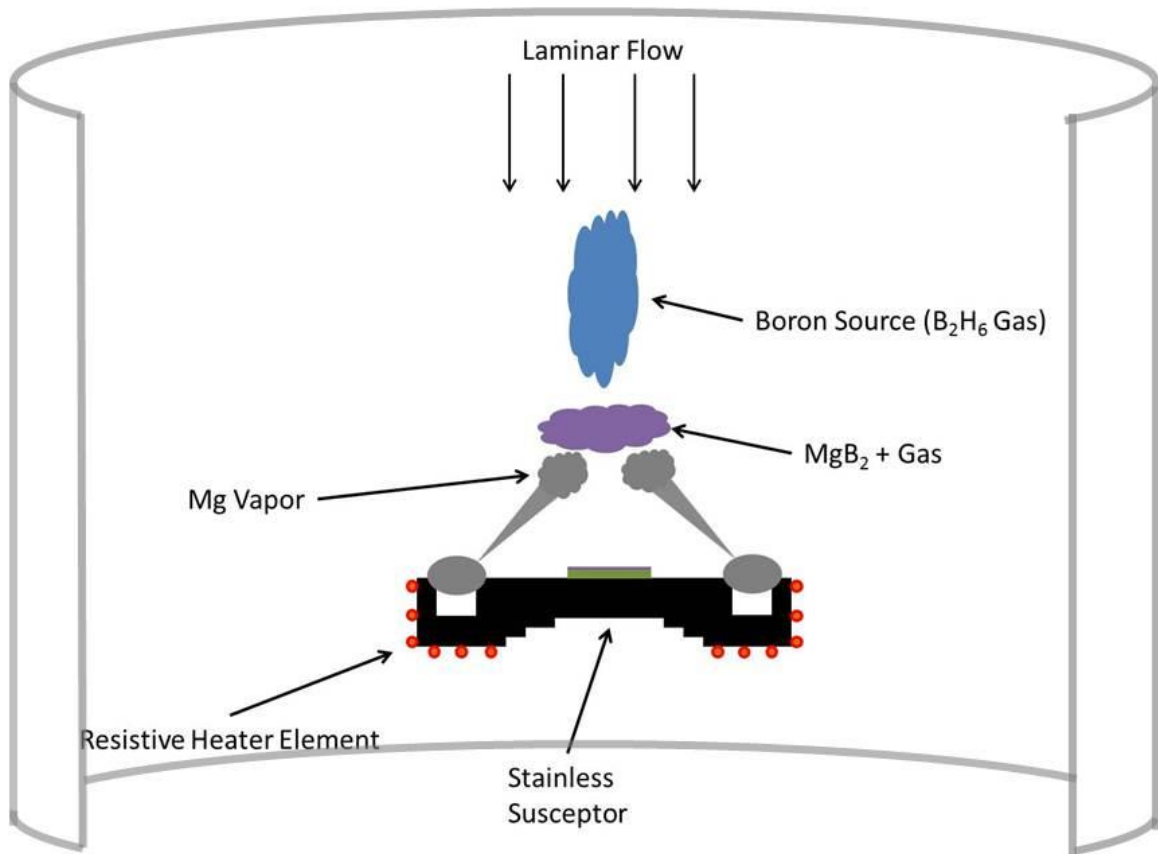


Figure 2.2. Set-up for the HPCVD process.

Fig. 2.2 shows the setup of the HPCVD reactor chamber. The substrate sits in the center of the susceptor and Mg pellets about 0.25" in diameter sit in the groove around the outside of the susceptor. The whole setup is then seated into a resistive heater wound into the shape of a cup to evenly heat the Mg. The susceptor has grooves in the bottom to give some separation from the heating element and the substrate. The stainless steel susceptor has poor thermal conductance which allows for a decent temperature gradient from the Mg to the sample.

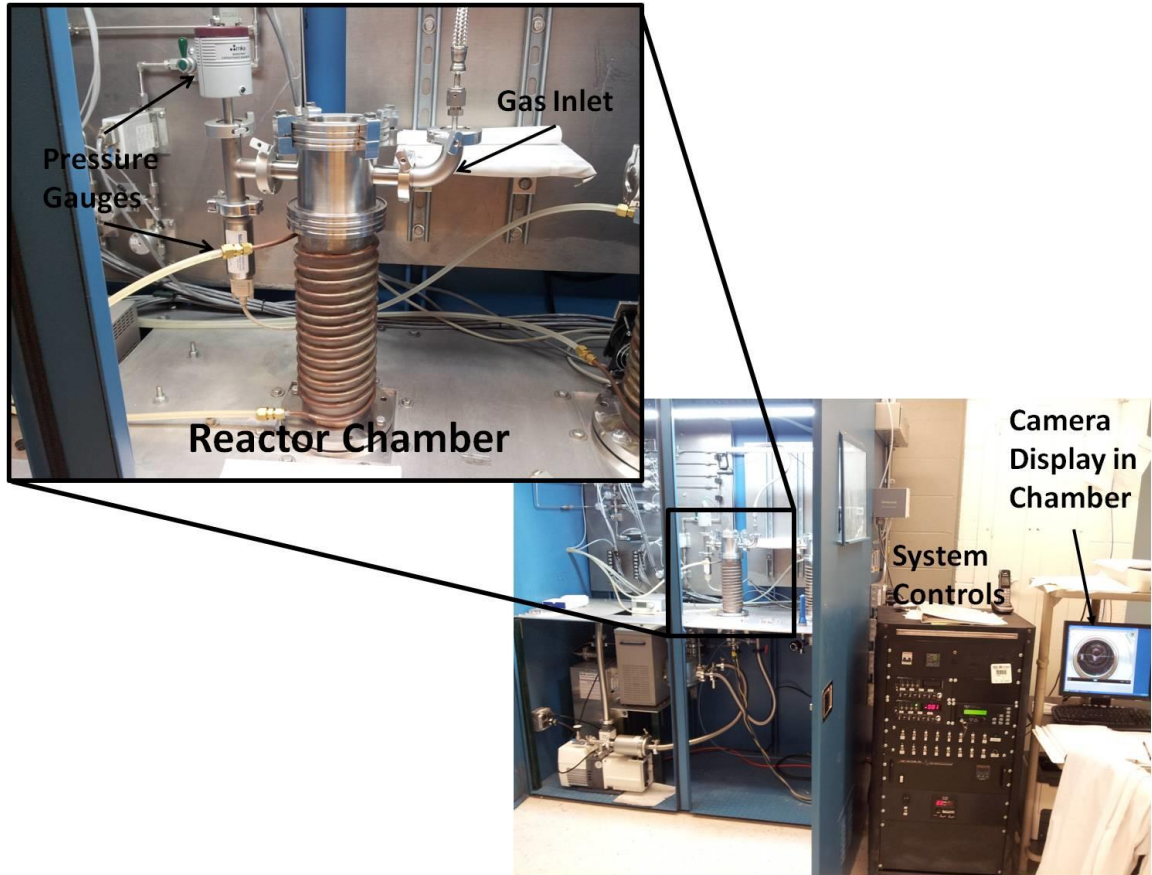


Figure 2.3. Photograph of the HPCVD system.

The standard deposition for device fabrication is on SiC substrate with root mean squared roughness of about 1 nm. The process pressure is 40 Torr using 400 sccm of ultra high purity H₂ carrier gas, and the deposition temperature ranges from 765 °C to 780 °C. The Diborane flow rate used is 20 sccm which is the main factor in controlling the deposition rate. 20 sccm N₂ is also used which helps to minimize the surface roughness without any degradation of the film qualities. The deposition rate is approximately 90

nm/min using this recipe within a deviation of 10 nm. Fig. 2.3 is a picture of the HPCVD setup used for this project. The system was built at Temple University and is currently one of only a handful capable of high quality MgB_2 thin films. Fig. 2.4 shows the resistivity as a function of temperature for a typical MgB_2 film grown on SiC substrate by the HPCVD method. The film measured is about 120 nm thick, the RRR ≈ 10 , and the $T_c = 41$ K.

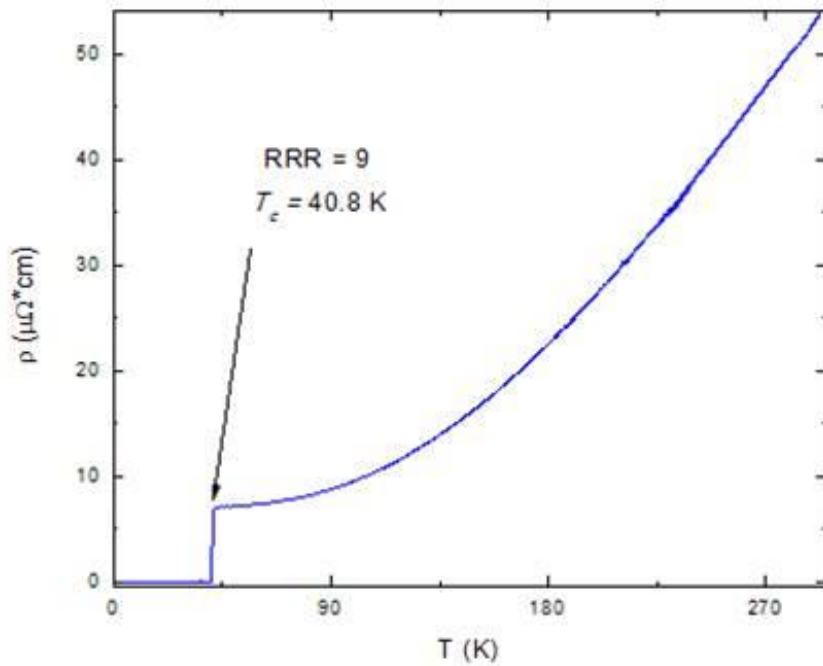


Figure 2.4 Resistivity versus temperature for a 120 nm MgB_2 film grown on SiC substrate.

2.2 Magnetron Sputtering

DC magnetron sputtering was used to fabricate metallic and semi-metallic thin films. The system used was a Kurt J. Lesker multisource system with a cryopump on the main chamber and a turbopump on a load lock chamber. A photograph of the system is shown in Fig. 2.5. A mechanical feedthrough allows for transport of samples from the load lock chamber to the main chamber. Each chamber has a viewport, a thermocouple gauge for higher pressure, and an ion gauge for low pressure. Once in the main chamber the sample can rotate around the center vertical axis of the chamber so that the sample can be exposed to multiple guns. A radiation type heater is capable of reaching temperatures above 400 °C. The maximum background vacuum achieved in the main chamber was 7×10^{-8} Torr. The system has three Torus sputtering guns which come directly vertical from the bottom, each equidistant from the center vertical axis. Each gun has an independent shutter to control deposition time. The system also has both a DC and RF power supply and is capable of supplying two separate process gases though only DC sputtering in Ar gas was utilized in this work.

The back to back in situ deposition of Cr and Au was necessary for gold wiring on devices because the Au films did not adhere well to the MgB₂ films without a thin Cr layer. This process was done with an argon flow rate of 10 sccm and argon partial pressure of 10 mTorr achieved by using a manual gate valve to control the pumping cross section of the cryopump. The Cr film was deposited for 30 seconds at 280 V and 93 mA

and the Au film was deposited at 490 V and 200 mA for different times depending on the application. Typically a 15 nm film is deposited for passivation of MgB₂ films for patterning purposes and a 120 nm film is used for device wiring layers.

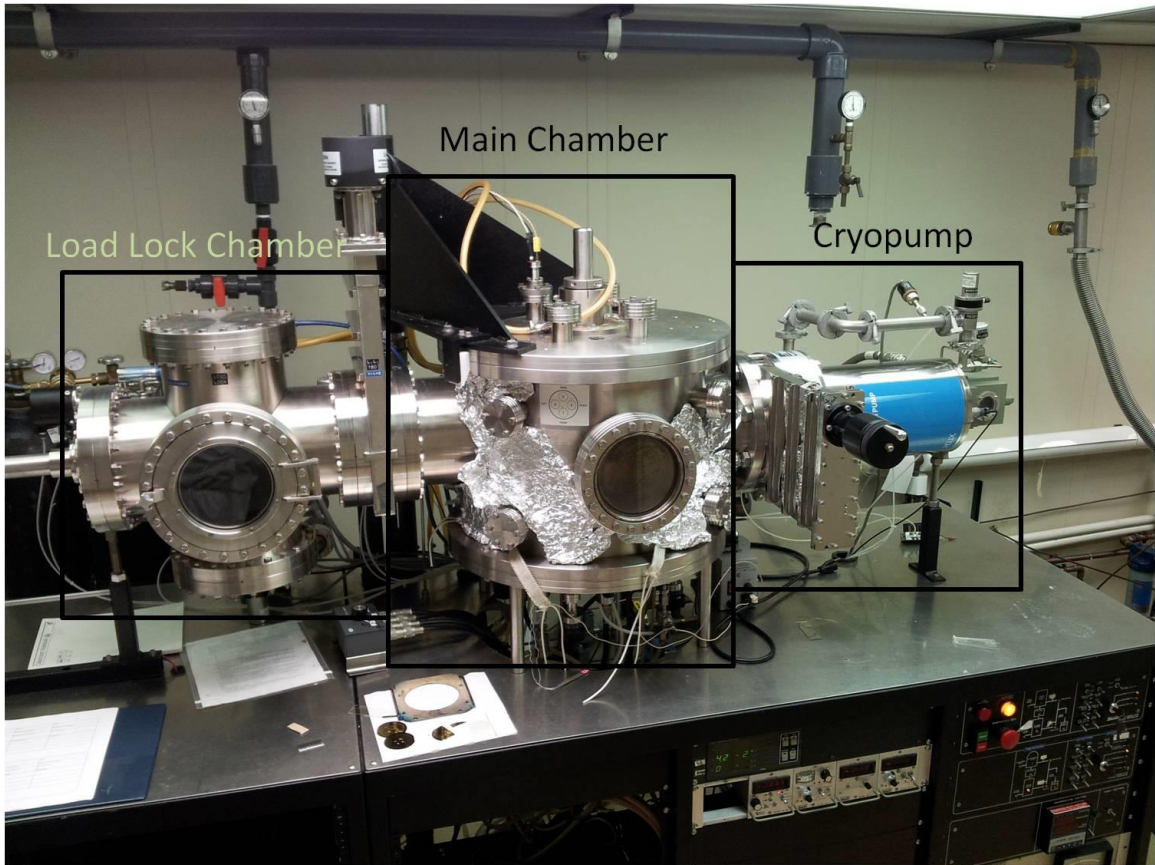


Figure 2.5. Photograph of the DC Sputtering system used to deposit Cr, Au, Mo, and Nb.

Nb films were used as a top electrode for Josephson devices which allowed use of the MgB₂ native oxide as the junction barrier. These films were deposited at room temperature at 270 V and 750 mA. Many other films such as TiB₂, ZrB₂, Mo, Ti, and Cr

were also grown via DC sputtering at varying growth parameters to achieve desired results for a thin film resistive layer.

2.3 Atomic Force Microscopy, X-ray Diffractometry, and Scanning Electron Microscopy

Both an atomic force microscope (AFM) and X-ray diffraction (XRD) machine were used to characterize the physical properties of thin films used in this work. While the AFM was constantly used to ensure good film roughness and surface morphology, the XRD was only used in the developmental stages of the HPCVD grown films. Once it was established that epitaxial MgB_2 films were grown on SiC substrate by a θ - 2θ scan, XRD was not used unless film properties were completely lost. Fig. 2.6 shows a θ - 2θ scan from 20° to 80° on a multilayer MgB_2/MgO structure grown on SiC substrate. The existence of the 001 and 002 peaks near 26° and 54° , respectively, show that the film is c-axis oriented or with the c-axis normal to the substrate surface. The sharp peaks denoted by the “*” are from the substrate. Additional peaks show up from MgO or other materials within the multilayer structure. This scan likely implies that only lower layers of MgB_2 are epitaxial because the peak height is significantly low for the MgB_2 peaks.

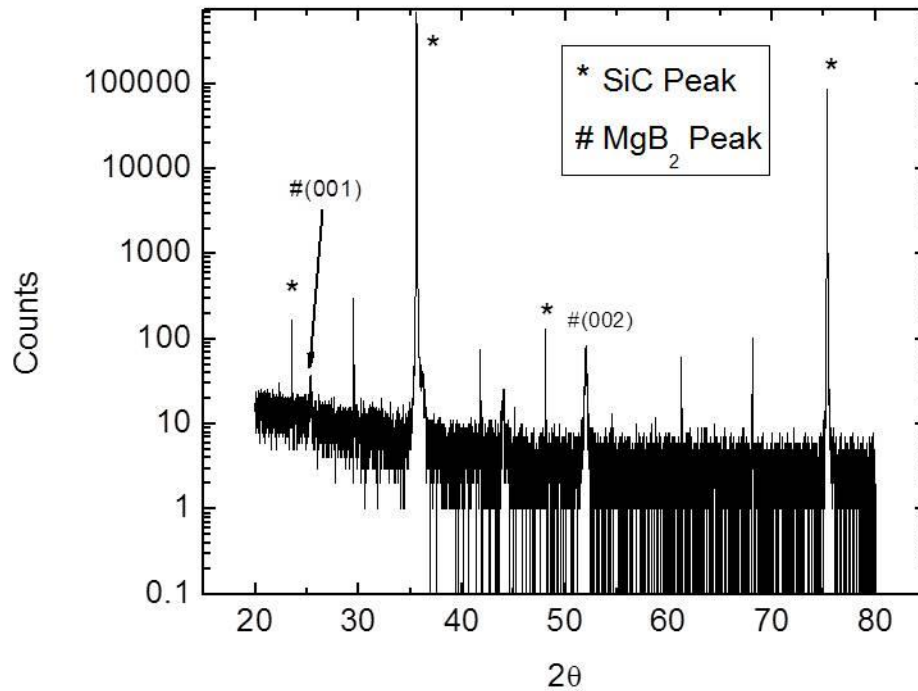


Figure 2.6. X-ray diffraction results for MgB₂ film on SiC substrate. The existence of the 001 and 002 peaks imply epitaxial growth along the *c*-axis direction.

The AFM was used constantly to verify that the roughness of films was as expected. Typical roughness of a 120 nm-thick MgB₂ film was about 2 nm with the addition of N₂ during the deposition. Fig. 2.7 shows an AFM scan of MgB₂ where hexagonal structures are visible which show good crystallinity and large grain sizes in the films. For junction application, the roughness of the films is the most important aspect. Each consecutive layer adds an additional degree of roughness and in the field of superconducting integrated circuits, the more layers is directly related to more complicated devices.

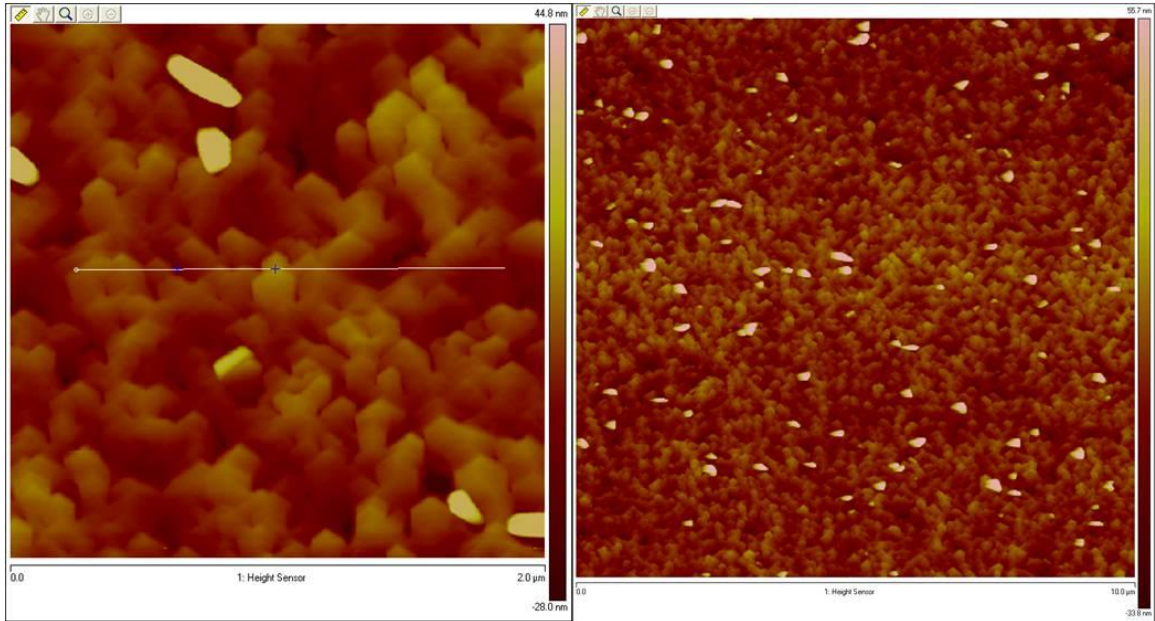


Figure 2.7. Atomic Force Microscope image of MgB_2 film. The left image is a $2\ \mu\text{m}$ scan and the right image is a $20\ \mu\text{m}$ scan. The hexagonal structures are MgB_2 grains. The peak to valley height across the white line in the left image has a maximum of 5 nm.

A Bruker table-top scanning electron microscope was also used to verify feature sizes after films were patterned. The images shown in Fig. 2.8 show a $5\ \mu\text{m} \times 5\ \mu\text{m}$ (left) and $2\ \mu\text{m} \times 2\ \mu\text{m}$ (right) square junctions which is the smallest working MgB_2 Josephson junction to date.

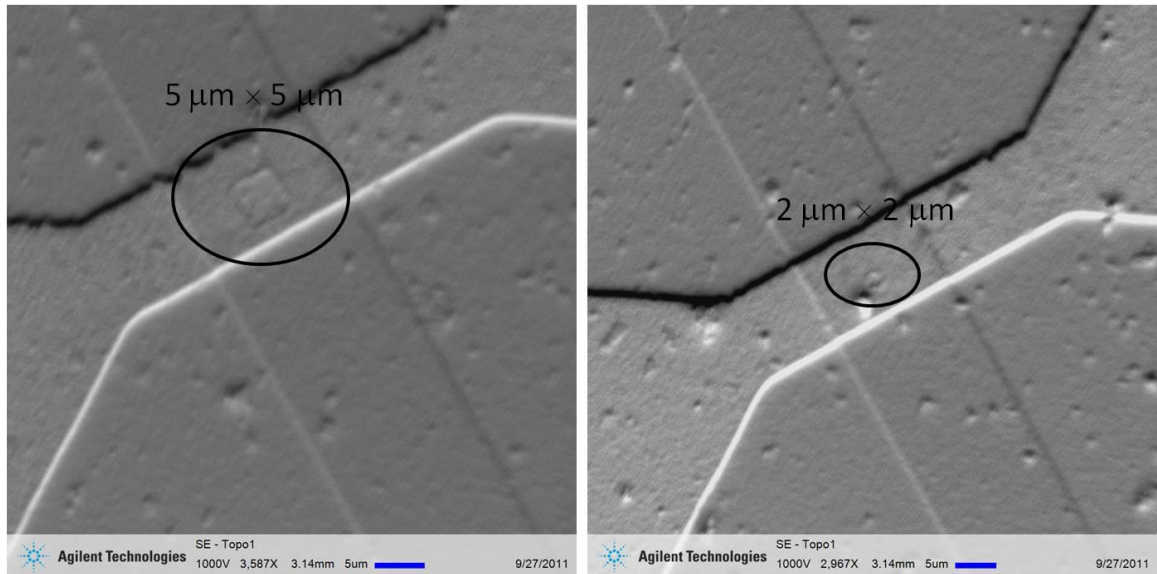


Figure 2.8. Scanning electron microscope image of square junctions with length 5 μm (left) and 2 μm (right).

2.4 Microfabrication Techniques

A standard ultraviolet photolithography process was realized in order to transfer patterns to the sample and Ar ion milling was used to etch the patterns into the films. For junctions, SQUIDs, and circuits, a 3-mask set was used. The recipe is described in detail in Appendix A. The Karl Suss MJB-4 mask aligner, shown in Fig. 2.9, was used to transfer the patterns onto the sample from a quartz mask with chrome patterns.

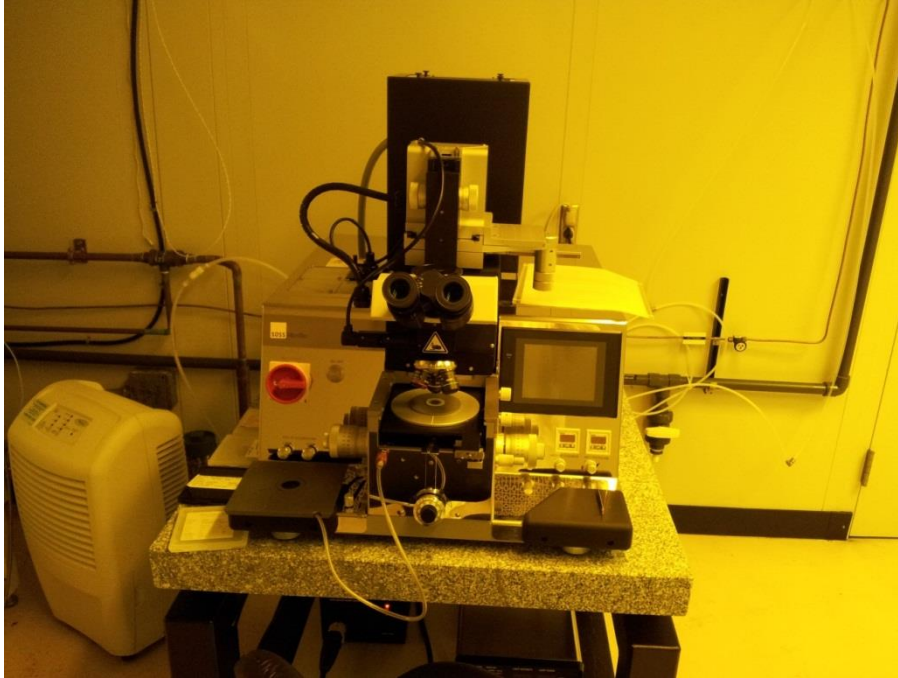


Figure 2.9. Photograph of the Karl Suss MJB-4 Mask Aligner. Yellow tinted light is to avoid exposing the photoresist.

The Intlvac Ar ion milling system contained a Maglev Turbo pump which could pump the large cylindrical chamber to better than 1×10^{-6} Torr in 15 minutes (about the time it took for the turbo to reach full speed). The system had a chilled sample stage which both rotated in the plane of the sample surface, as well as rotate around the center axis of the cylindrical chamber to change the incident angle of ions. The standard angle used was 45° from perpendicular to minimize resputtering of material onto the sample. The Kaufmann power supply and 8 cm source was set at 600 V and 200 mA to etch the MgB_2 at a rate of about 30 nm/min. Etching rate spread across the 4 inch sample stage was less than 2 %.

2.5 Low Temperature Measurement

There were three main techniques for low temperature measurement. These systems have a temperature diode which measures the temperature with a response curve calibrated with a Lakeshore Cryotronics temperature controller. The first method was a probe dipped in liquid helium. Two different probes were used depending on the application. For typical temperature dependence of thin film resistivity or low temperature *IV* scans, a simple 8-pin probe was used. For more complicated measurements a custom built junction measurement probe was made with 28 pins which connect to a sample puck which can then be wire bonded to the sample. The probe is vacuum sealed with Fields metal (alloy with low melting point) and pumped to approximately 1 mTorr before it is backfilled to about 1 Torr with helium gas. This allows for an internal heater to heat the sample without direct contact to the liquid helium. The helium gas allows some thermal conductivity to decrease the cooling time of the sample. This probe has a calibrated coil to generate a magnetic field, and an RF shielded cable which can supply up to 18 GHz of microwave radiation directly to the sample.



Figure 2.10. Photograph of the Quantum Design PPMS system. Empty rack on the left hand side can be used to interchange measurement electronics.

A Quantum Design physical property measurement system (PPMS), shown in Fig. 2.10, was used to measure some Josephson junctions with a custom designed sample puck. Four junctions could be measured maintaining a twisted pair of wires all the way to the necessary electronics. This is important to prevent ground loops which can contribute large amounts of noise and magnetic flux. The sample puck also had a calibrated superconducting NbTi coil to apply a magnetic field of about 1200 G/A. Magnetic

shielding outside the coil helped to prevent undesired flux through the junctions. The main benefits of this system was the ability to reach 1.8 K for junctions with very low I_c , as well as the ability to gain a larger magnetic field, needed for measurement of smaller junctions

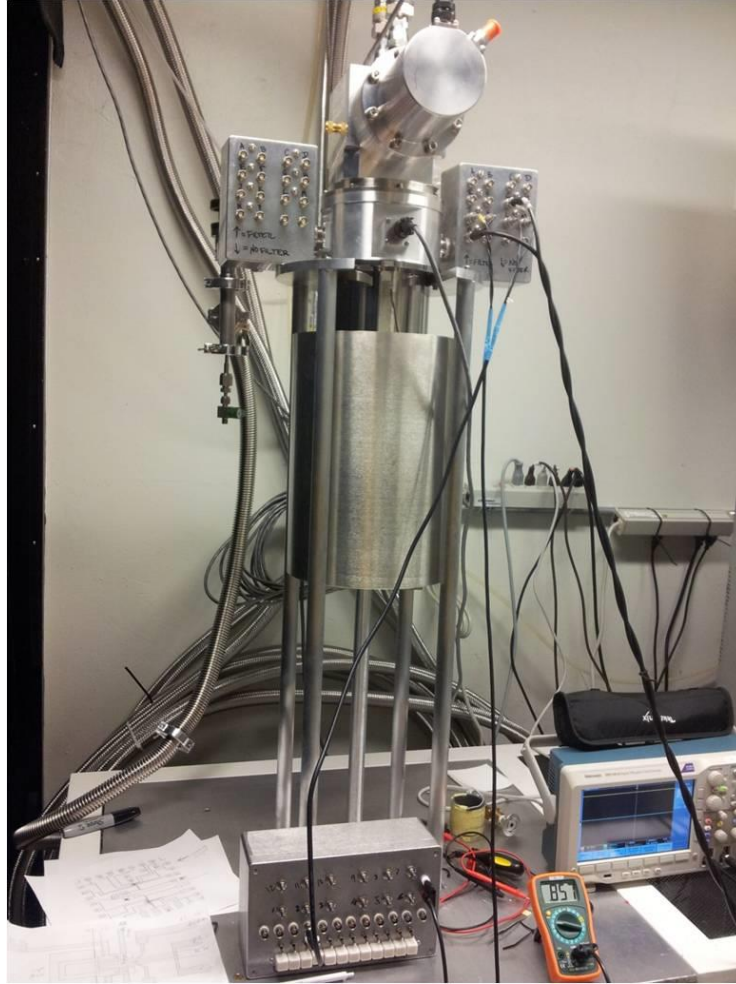


Figure 2.11. Photograph of the Janis Research pulse tube Cryocooler inside of dual layer of magnetic shielding. Connections directly to the unit avoid unwanted ground loops.

Most measurements were taken using a customized Janis Research pulse tube cryocooler. A photograph of the system is shown in Fig. 2.11. This system was built up to have the same abilities as the junction dipping probe. There are 28 pins connected to BNC connectors by 14 twisted wire pairs to minimize ground loops and eliminate noise. There are passive RC filters on each twist pair to filter out any unwanted frequencies

above 10 Hz. This frequency was chosen to ensure that the noise due to the 60 Hz signal from the power outlet is not measured in the devices. The filters are connected in such a way that they can be switched off and bypassed in the event that they are not necessary. The length of the the twist pairs in the cryocooler is much shorter than in a dipping probe and by making contacts directly to the unit with shielded BNC connectors the potential for a ground loop is much smaller than a dipping probe.

The ultimate temperature reached by this system is down to 2.8 K with a coil installed. Unlike a dipping probe, there is a bit more room available to expand the system for different measurements. Two coils were made so that a field can be applied both parallel and perpendicular to the film surface for measurements of new devices.

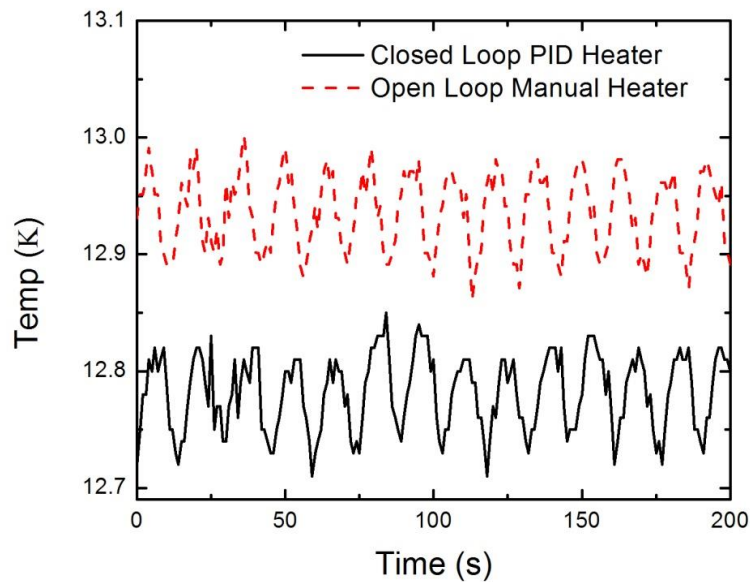


Figure 2.12. Temperature verse time comparison of closed loop PID controller and a manual output heater. Similarities in period and amplitude indicate that modulation is a product of gas compression.

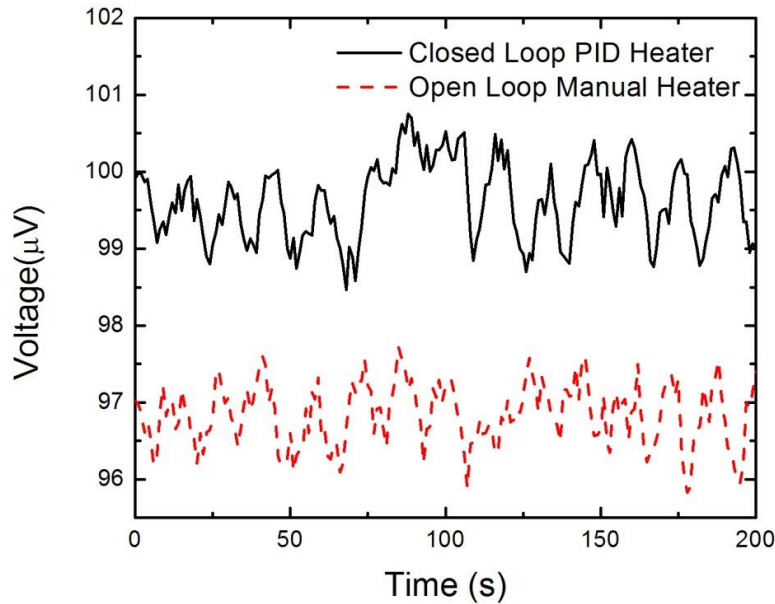


Figure 2.13. Voltage across a DC SQUID verse time comparison of PID controller and manual output heater. Similarities indicate the temperature dependence, not flux from the heater, is responsible for modulation.

The noise level of this system has been lowered significantly from the original setup. The first noise measurements gave a noise level above $10 \mu\text{V}$. The ultimate noise level of this system after modifications to minimize ground loops and add filters has been near 300 nV which is very reasonable for a cryocooler which has moving parts.

The temperature stability is not as ideal as a dip probe but has fluctuations of about $.1 \text{ K}$ below 30 K and at higher temperatures it is much more reasonable. These temperature fluctuations contribute additional noise at temperatures near the T_c of the devices. The temperature dependent properties of superconducting devices diverge near

T_c and so the signal can fluctuate much more with the temperature. Fortunately the fluctuations are slow and so a measurement that can be taken very quickly, will not see much fluctuation. Fig. 2.12 shows the thermal fluctuations as a function of time in the cryocooler. At first it was assumed that the fluctuations in voltage could be from the induced field of the fluctuating current through the heater element. Later it was established using a DC SQUID with very sensitive field dependence that there was no difference in noise from heating using a PID controller, or a constant heating current. Fig. 2.13 shows the voltage of the SQUID as a function of temperature using both a PID controller and manual current supply to maintain temperature. Notice that the period of oscillations match the temperature oscillations shown in figure 2.12. This implies that the temperature alone is responsible for the large voltage fluctuations.

A lot of effort went towards minimizing these thermal fluctuations, by manually controlling the heater, as well as tuning the PID controller, but the nature of the pulse tube cryocooler implies that they are unavoidable. One potential idea is to add a large thermal mass to the cold head, making the relaxation time to thermal equilibrium much larger than the period of oscillations. This will have a significant impact on the low temperature limit which can not be sacrificed at the current time. In the future, if devices are designed to work at 20 K or above, this may be a very viable option.

2.6 Electronics and Computer Interface

There were many electronics used to measure devices in this work. The most common measurement was an *IV* scan which utilizes a Keithley 2400 digital

multimeter/current source with at Stanford Research Systems SR560 preamplifier to increase the signal to noise ratio. A similar IV scan was also done using a Keithley 3390 function generator, two SR560 preamplifiers and an oscilloscope. The benefit of faster scans yielded less $1/f$ noise and eliminated self heating effects. This method also allowed for the IV curve to be observed in real time, so that the effects of an external influence such as magnetic field or current bias could be seen directly. For device resistivity and noise measurements either a Keithley 182 or 2182 nanovoltmeter was used to measure the voltage across the device while the current was supplied with either a Keithly current supply or a multisource battery current supply. All measurements are interfaced with the computer by National Instruments Labview programs.

CHAPTER 3

MAGNESIUM DIBORIDE JOSEPHSON JUNCTIONS AND RELATED DEVICES

3.1 MgB₂ Josephson Junctions

A good first step for any technology utilizing the Josephson Effect is to start by making junctions using a well-known superconductor, such as Pb for one of the electrodes. This was especially important for MgB₂ because of the unknown impact that a multi-gap superconductor could have in typical Josephson devices. Prior to this work, it was shown that MgB₂/Native Oxide/Pb junctions could be used to show that a Josephson junction was indeed possible using MgB₂[69]. There were many other attempts to make MgB₂ junctions using many different counter electrodes[70-77]. There were also many early attempts to make all-MgB₂ Josephson junctions[78-95]. Most of these junctions showed relatively low $I_c R_n$ product, a high leakage current, and maximum operating temperature near 20 K, well below the T_c of MgB₂. The most promising junctions utilized either an AlN barrier[89], or an MgO barrier[78]. Although the junctions with an MgO barrier did not utilize a tunneling effect[96], they had a low temperature $I_c R_n$ product over 3 mV and operated near the T_c of MgB₂. The goal of this work was to replicate and improve on these junctions utilizing all newly developed systems and take the technology one step further to create more complicated Josephson devices and circuits.

After the new HPCVD system was shown to produce films equal to those grown by other groups [68], the first step was to replicate the Pb junctions reported previously[69]. This ensured that the surface of the films was a similar quality to those films which produced good tunneling properties. A detailed description of the process is provided in ref. 70. The process included growing an MgB₂ film by HPCVD on SiC substrate. The sample was then “painted” with insulating glue which was dissolved in acetone to control the thickness of the insulating layer. The result was an exposed strip line of MgB₂ down the center of the sample which was about 0.25 mm wide. Pb stripes of similar width were then deposited, through a shadow mask, perpendicular to the MgB₂ stripe by thermal evaporation. The intersection of the strips was then measured as a tunnel junction. A picture of the sample can be seen in Fig. 3.1.

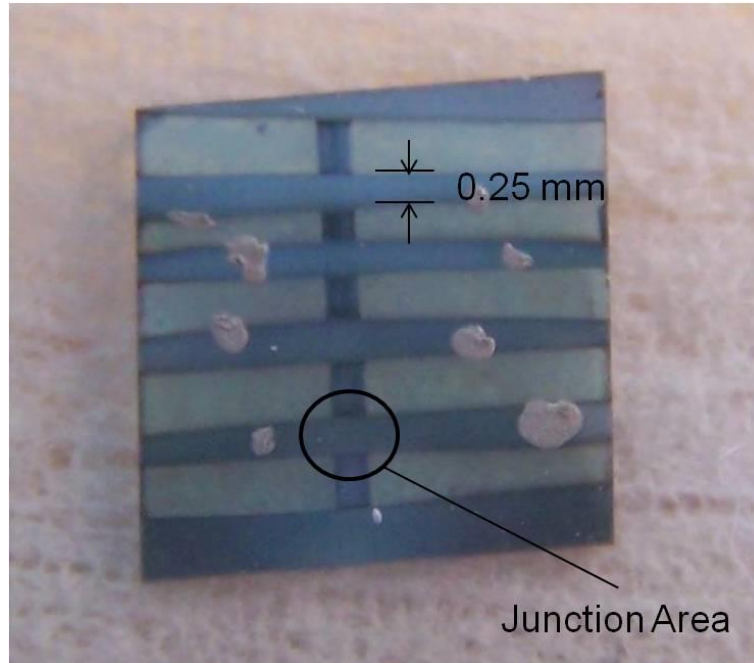


Figure 3.1. Optical image of an MgB₂/Native Oxide/Pb Junction.

Continued success with these types of junctions lead to the realization that some new physics related to MgB₂ was still achievable using the magnetic field dependence of the junction critical current. Up until this point the magnetic penetration depth of MgB₂ was controversial. An exact value could be extrapolated using the I_c-B modulation of the junctions as long as the junction size was known. A more in depth study of this research is presented in Chapter 5 of this work. The one issue with Pb junctions was that the junction size was not in the small junction limit, meaning that self-field effects could have a large impact on the results. Smaller junctions could be made using standard UV photolithography but Pb is too soft for this process. As a result, the Pb top electrode was replaced with Nb film deposited by DC sputtering. A few failed attempts proved that the

sputtering process was much more aggressive on the native oxide than thermal evaporation. This was eventually remedied by allowing the native oxide to grow at much higher temperatures. The fabrication process of these junctions required that first a bilayer be grown. A layer of MgB_2 was first grown by HPCVD which was removed from the system and exposed to air while the sample was still about 200°C . A layer of Nb was then grown *ex situ* on top of the MgB_2 . A passivation layer of Au was added later to protect these films during the lithography process. The full patterning process is described in Appendix A. The size of the square junctions ranged from $4\ \mu\text{m}$ to $70\ \mu\text{m}$ per side.

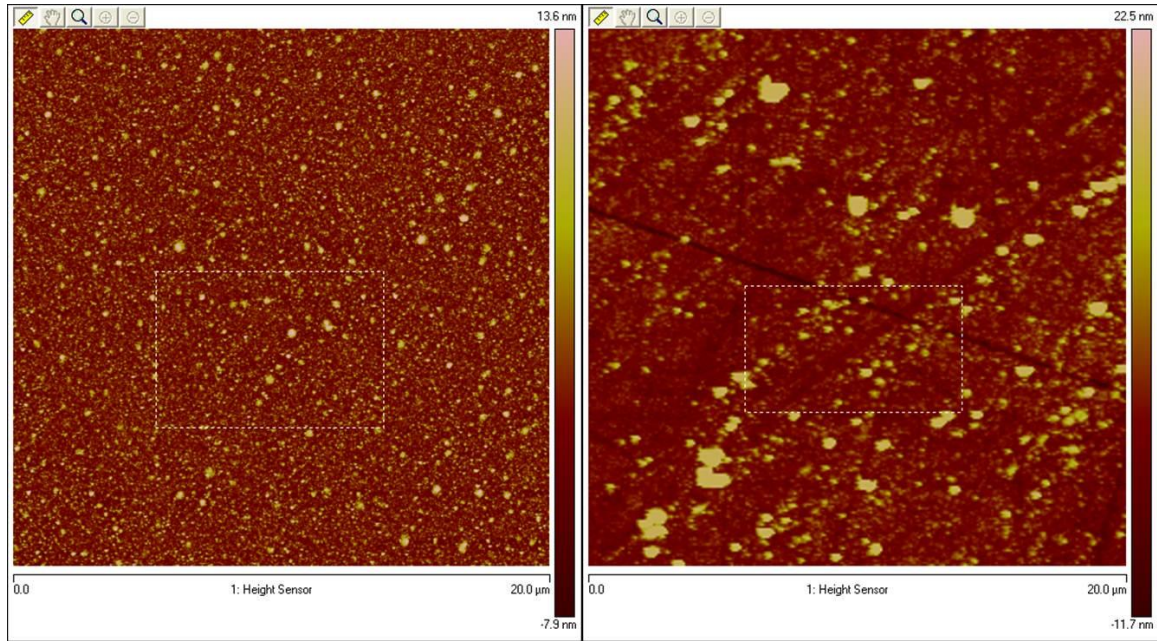


Figure 3.2. AFM comparison of 100nm-thick MgO thin films on SiC substrate using reactive sputtering of an Mg target (left), and RF sputtering of an MgO target (right). Scan size is 20 μm for both images.

Finally, the $\text{MgB}_2/\text{MgO}/\text{MgB}_2$ junctions from ref. 78 were also replicated. The process was originally developed and published by Chen, *et al.* although some changes were made throughout this work. Here I present the most recent results which epitomize the current status of the junction technology. The major differences include minimizing the top electrode thickness in the original trilayer so as to minimize the etching time needed for the definition of the junction area. This is in attempt to minimize the etching of the resist which causes the walls of the patterned features to be slanted, increasing the property spreads due to lithography error. Another major change includes the time taken to heat the sample to deposition temperature during the HPCVD process. Originally the sample was slowly heated from room temperature to a deposition temperature over a 20

minute period. After some experimentation, it was established that the heater element could withstand much quicker heating and the film suffered no drawbacks in quality. Now the system can be heated in about 8 minutes which reduces the time that the barrier layer is exposed to high temperatures and hydrogen gas, which can absorb some oxygen out of the barrier, especially at elevated temperatures. The final and most significant change made to the fabrication procedure was to change from an MgO barrier which was RF sputtered from an MgO composite target, to an MgO barrier which is deposited by DC reactive sputtering from an Mg target in an Oxygen environment. An AFM comparison between these two films is shown in Fig. 3.2. The RMS roughness is improved by about 50% from 2 nm to about 1 nm for a 100 nm film. The color scale of the RF sputtered film (right) is about 30 nm, while the scale of the reactive sputtered film (left) is only 20 nm. The uniformity of the reactive sputtered film is a large improvement. Not only did these changes improve junction parameters over the original presented results, it has also reduced the overall fabrication time by hours. A full step-by-step fabrication process of these junctions is described in Appendix A.

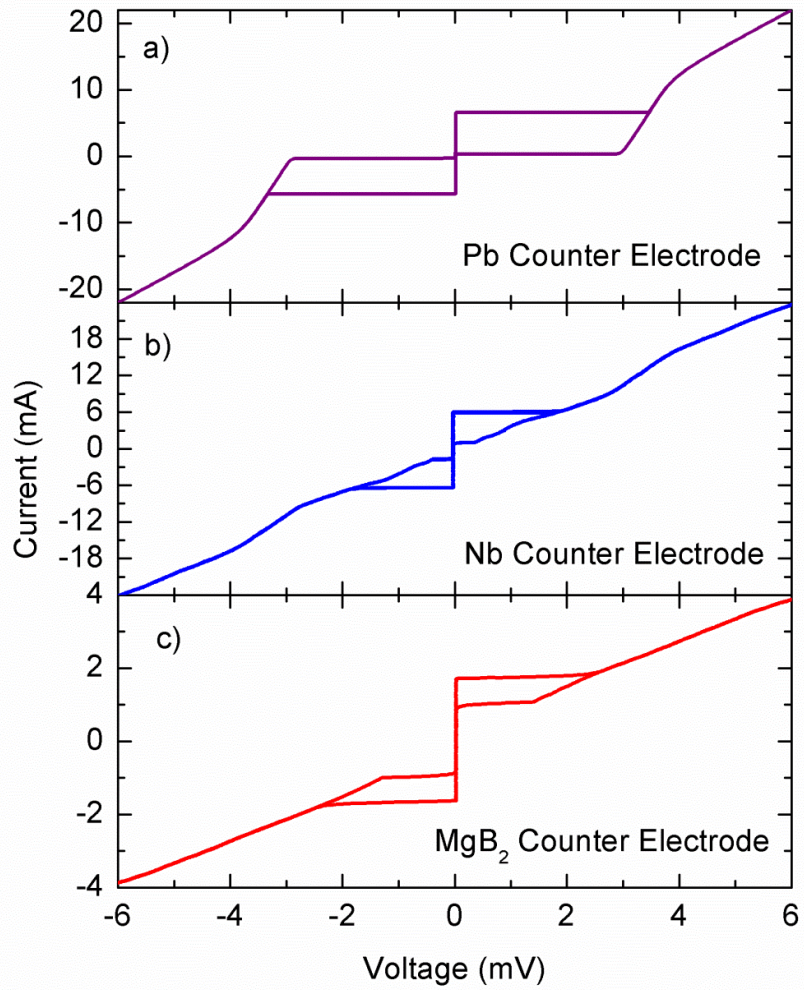


Figure 3.3. IV characteristics of a MgB₂/Native Oxide/Pb junction (top), MgB₂/Native Oxide/Nb (middle), and MgB₂/MgO/MgB₂ (bottom) Josephson Junction.

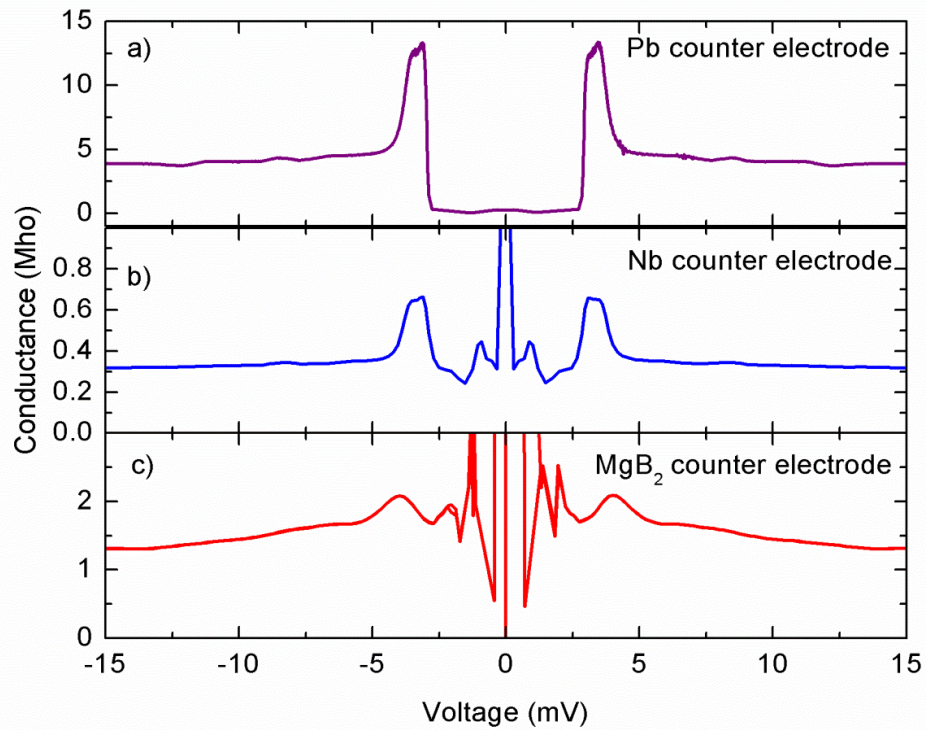


Figure 3.4. Conductance curve of a MgB₂/Native Oxide/Pb junction (top), MgB₂/Native Oxide/Nb (middle), and MgB₂/MgO/MgB₂ (bottom) Josephson Junction.

The measurements of these junctions were done in a custom cryogenic probe dipped in liquid helium, in a Quantum Design PPMS, or in a Janis Research pulse tube Cryocooler. The Pb junctions showed properties typical of SIS tunneling Josephson junctions while the junctions with Nb and MgB₂ counter electrodes both showed Josephson junctions in which the transport was dominated by MAR[96]. The HPCVD film is grown epitaxially along the *c*-axis. This meant that most junctions only show contributions from the 3-dimensional π -gap, though some junctions did show small

contributions from the quasi-2-dimensional σ -gap. Fig. 3.3(a), (b), and (c) show typical IV characteristics of a Pb, Nb, and MgB₂ junction, respectively. The conductance curve of each of these junctions, with the I_c suppressed as best as possible by a magnetic field, is shown in Fig. 3.4. The $I_c R_n$ of the Pb and Nb junctions were around 2 mV and for the MgB₂ junctions the $I_c R_n$ was near 3 mV, though some MgB₂/MgO/MgB₂ junctions have shown higher. While the Pb and Nb junctions had minimal temperature dependence until near T_c of the counter electrode, the MgB₂ junctions show unusual temperature dependence of the superconducting gap parameter as well as the $I_c R_n$ dependence which is indicative of the two gaps in MgB₂. Fig. 3.5 shows the $I_c R_n$ dependence on temperature for a typical MgB₂/MgO/MgB₂ junction. The most appreciable aspect of this temperature dependence is that the junctions can be self-shunted at a reasonable temperature while still exhibiting parameters which are suitable for device application. This means that the β_c parameter described in section 1.5 can be controlled by temperature. Even under conservative estimates, a reasonably high $I_c R_n$ of about 1 mV can be achieved at a temperature of 20 K without any hysteresis. Ultimately, an external shunt will be desirable for process control, and work is presented in Chapter 4 which expands on the use of a shunt. It should also be noted that there is an inflection point in this curve at about 14 K. This is evidence of the two gap nature of MgB₂ because the BCS calculated T_c of the π -gap would fall near this temperature. The effect is smeared due to interband scattering.

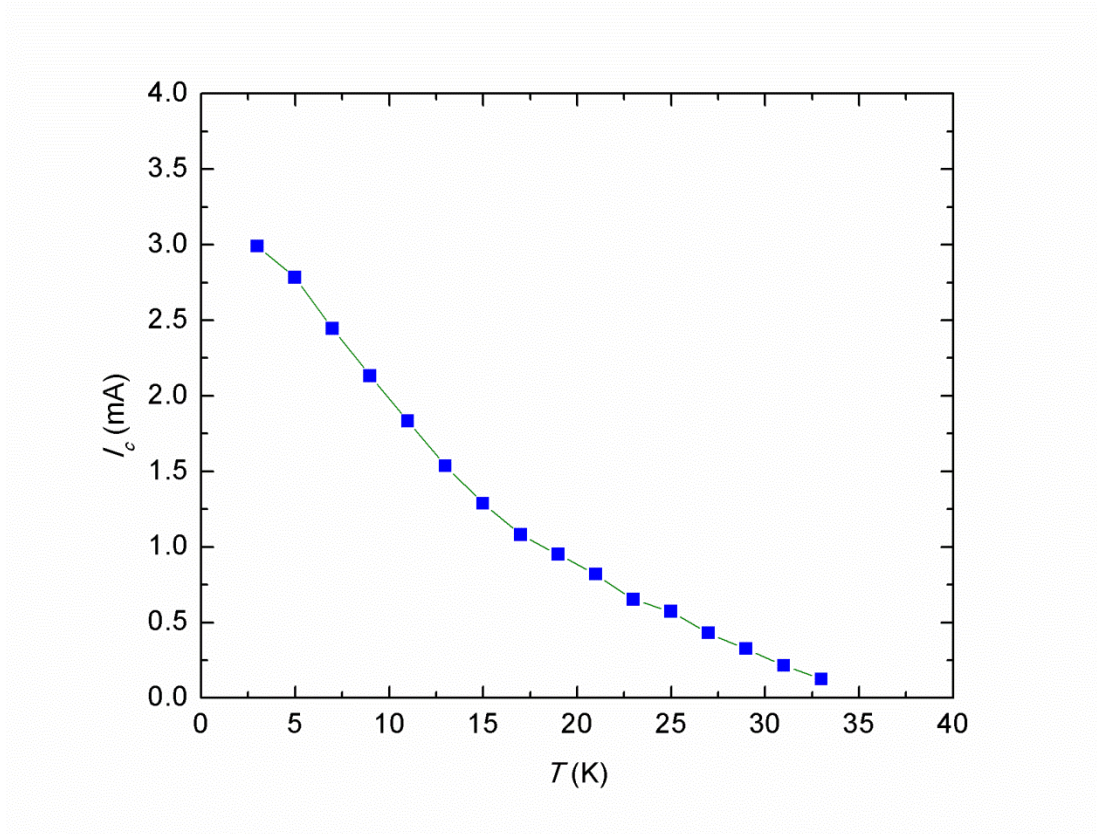


Figure 3.5. Temperature dependence of the critical current of a MgB₂/MgO/MgB₂ Josephson junction.

It is standard when presenting Josephson junctions to include either the magnetic field dependence of the I_c or the Shapiro steps resulting from radiating the junctions with a microwave source[97]. These verify that the junctions are truly following the two Josephson relations shown in section 1.3. The field dependence is verification of the DC Josephson relation, while the Shapiro steps confirm the AC Josephson Relation. All the junctions presented here were authenticated using the field dependence rather than the Shapiro steps because the experimental method used for measuring field dependence

requires only a magnetic coil, while the Shapiro steps require a microwave source and a cable which can carry the microwaves to the sample without dissipating the power.

Fig. 3.6 shows the I_c - B curve for the Pb junction (solid line) which show many minima with the I_c completely suppressed in the higher order minima, which is a good indication that there is no leaks in the barrier. The non-ideal pattern is difficult to fit both the amplitude and period to theory (dashed line) because of two main reasons. The first is the non-uniform J_c , which controls the amplitude of the maxima in the pattern. Some systematic calculations are given in ref. 35 for different J_c distributions. The abstract pattern obtained from the Pb junctions indicates a very random distribution of the J_c . The second reason is the size of the junctions. As previously stated, the dimensions of the Pb junctions are not very small when compared to the Josephson Penetration Depth, which means that self-field effects can have an impact on the I_c modulation in an external field. The inability of the lower order minima to reach zero suggests that there are self-field effects present.

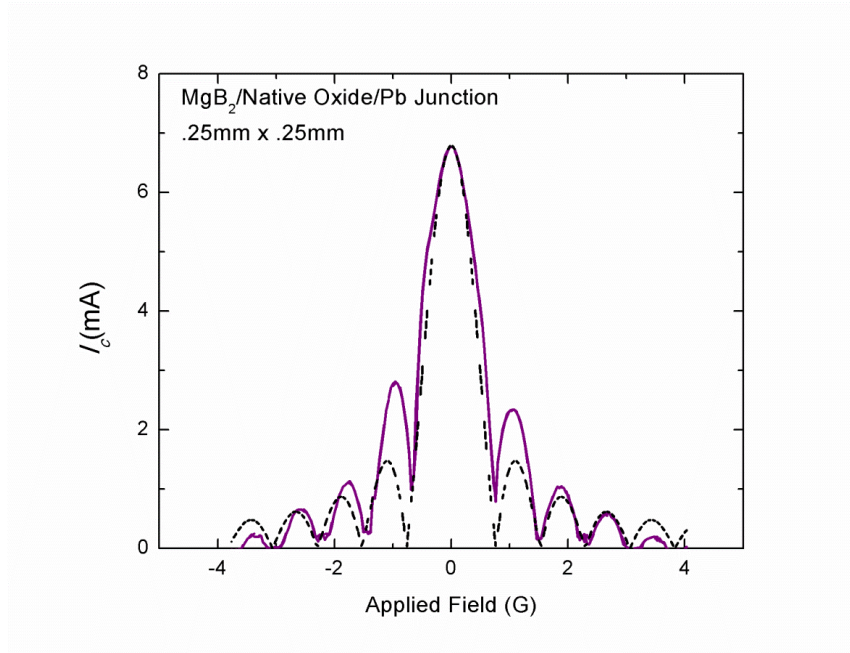


Figure 3.6. Magnetic field dependence of an MgB₂/Native Oxide/Pb junction. Dashed line depicts a theoretical fit.

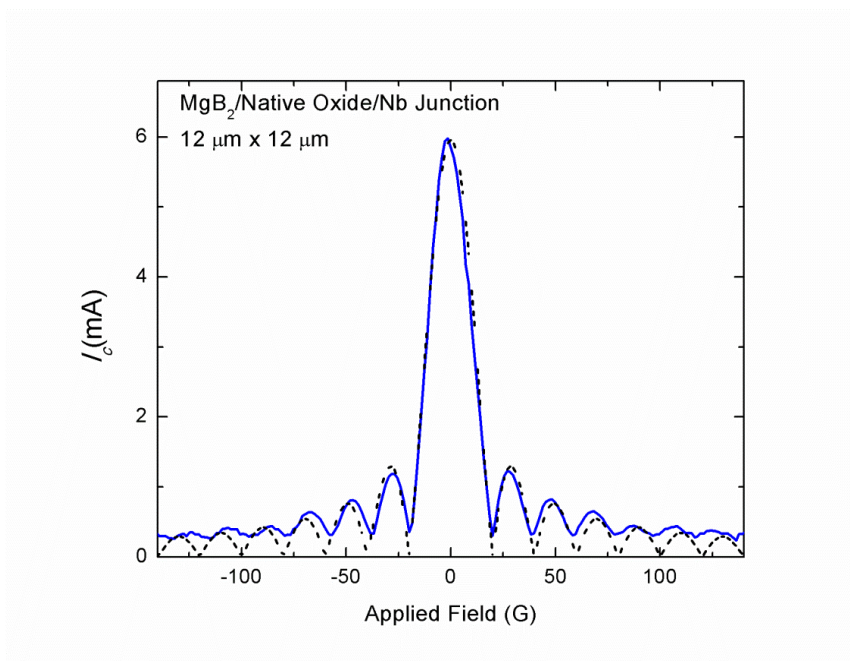


Figure 3.7. Magnetic field dependence of an MgB₂/Native Oxide/Nb junction. Dashed line depicts a theoretical fit.

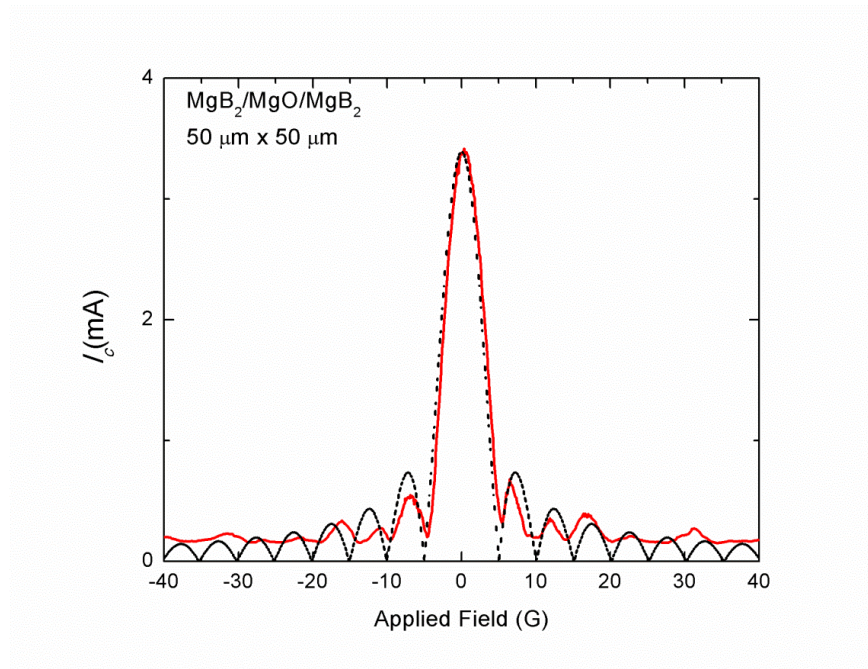


Figure 3.8. Magnetic field dependence of an $\text{MgB}_2/\text{MgO}/\text{MgB}_2$ junction. Dashed line depicts a theoretical fit.

The modulation of Nb junctions shown in Fig. 3.7 is nearly ideal, and fits very well to theory (dashed line). This is a good sign of low leakage and uniform J_c , in junctions well within the small junctions limit. This is actually a great result considering the fact that these junctions are not tunnel junctions but instead dominated by MAR as indicated by Fig. 3.4. In recent years, even the low temperature superconducting devices have moved towards more transparent barriers in an attempt to increase the J_c of the junctions[98, 99]. The good modulation of these junctions indicates that it may be possible to utilize MAR dominated junctions for Josephson applications. It could be very

useful to precede any work with all- MgB_2 junctions with these Nb junctions. The excess work of developing a shunt resistor, could prove to make low temperature devices which easily exceed the ability of all-Nb junctions, which may restore some faith of researchers into the applicability of MgB_2 which has been in decline over the last few years without significant progress on a junction technology. The work presented in Chapter 4 of this work shows that Mo, which is already used as a shunt resistor in Nb devices, is also compatible with MgB_2 .

The $\text{MgB}_2/\text{MgO}/\text{MgB}_2$ junctions have much more random modulation in a magnetic field as shown in Fig. 3.8. Although the I_c is completely suppressed, it is readily evident that the J_c uniformity is not ideal. This is also evident in the on-chip property spreads of these devices. Early measurements of this spread are presented in Chapter 4. With all the recent changes in this process, an improvement has been seen, with overall on-chip property spreads shrinking, and similar-size junction property spreads seeing an even better improvement. It is not clear at this time whether or not the improvements here are from patterning, or an intrinsic improvement in the barrier. It is likely that there is small improvement in both of these as each of the three process changes yields some small improvement. The I_c - B modulation seems to be more ideal than previous measurements, though that type of qualitative data is not conclusive. Fig. 3.9 is a comparison of the IV characteristic of $\text{MgB}_2/\text{MgO}/\text{MgB}_2$ junctions before these improvements (bottom) and after (top). Although reports of the $I_c R_n$ product for these junctions are always taken to be the product of the maximum I_c and the normal resistance of the junction as determined by the slope of the IV characteristic well outside the gap

region (about 20 mV), it could be argued that the amplitude of the voltage jump when the junction switches to the resistive state is also a good measure of the applicable $I_c R_n$ product. This jump has increased from less than 2 mV to as high as 2.5 mV using the improved process. More experiments are currently being carried out to verify these improvements on a more qualitative basis.

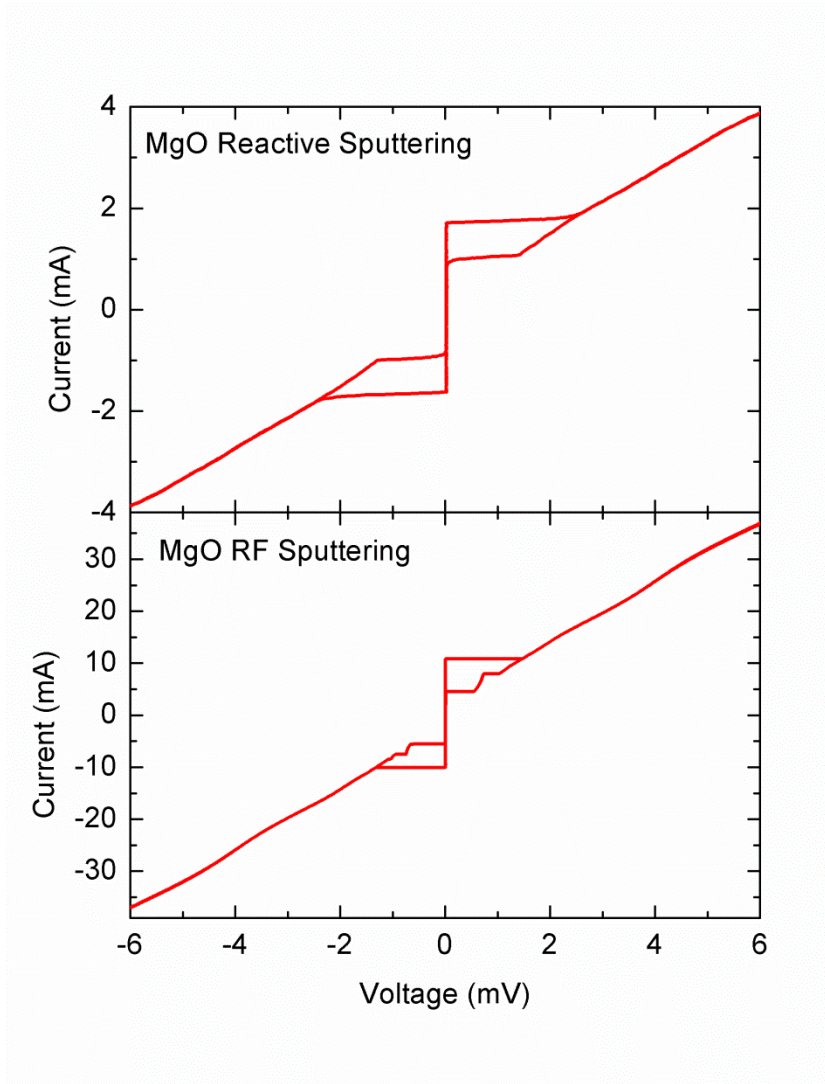


Figure 3.9. Comparison of $\text{MgB}_2/\text{MgO}/\text{MgB}_2$ Josephson junctions before (bottom) some process design changes and after (top).

To summarize, these results have achieved three main objectives. The first is to replicate the previous results of Josephson junctions utilizing a Pb counter electrode. This shows that the MgB_2 films prepared in the lab at Temple University are of the same quality of films used previously to make junctions. The second objective was to use a counter electrode which is more affable to fabrication than Pb. Sputtered Nb films were

used which produced junctions that were useful for studying the two gap nature of MgB_2 as well as a potential first step for more complicated MgB_2 Josephson devices. Finally, $\text{MgB}_2/\text{MgO}/\text{MgB}_2$ junctions were fabricated and improved upon. The enhancements to these junctions over previous work take the junctions closer to being a reasonable alternative to low temperature superconducting electronics, even though qualitative data on these improvements is still pending.

3.2 MgB_2 Planar Washer-Type DC SQUIDS

DC SQUIDS have the ability to measure extremely small changes in magnetic fields. This tremendous sensitivity makes these SQUIDS very useful for many applications, most commonly in biomagnetic purposes such as magnetoencephalography or magnetocardiography. They also have function in geomagnetism and most interestingly related to superconducting materials, non-destructive testing. SQUID magnetometers are used to study the physics of new materials. They can easily characterize the surface of a superconducting thin film, or measure a local magnetization in a material or object. The practical ability of these devices to measure changes in a magnetic field is dependent on the properties of the superconductors used to make the devices. The three SQUID properties used to determine the overall quality of the device are the operating temperature, the amplitude of the voltage modulation, and the noise inherent in the device. The first two of these are ultimately limited by the material used in making the device and the last can be improved with device optimization.

The first DC SQUID was developed in 1964 at Ford[100]. Since then, there has been an ever changing state of the art. The most abundant devices used now are made with low temperature superconductors such as Nb or Nb compounds. These devices have major advantages in the Josephson junction technology used to make the devices. Nb junctions work to the theoretical limit allowed by the material. HTS like YBCO have also been used to make DC SQUIDs with some success[101]. Though the fabrication of HTS Josephson junctions is difficult due to the very small coherence length and anisotropic nature, and pairing symmetry of the material[102], the high operating temperature of the device is a benefit which continues to outweigh the difficulties. MgB₂ offers an alternative with advantages over Nb devices in the operating temperature and ultimate limit while not having the same difficulties in fabrication of YBCO. There have been some attempts to make MgB₂ based SQUIDs but none are ideal for applications. Most attempts have been using nanobridges as the Josephson link[103-105]. The repeatability of these nanobridges is difficult and they only act as a weak link in the case when the device is at a sufficiently high temperature. Another type has been made by Zhang *et al.* but it was not shown to work above 19 K, though this device was useful in demonstrating that there are no noise issues specific to the MgB₂ itself [106]. The lack of a multilayer junction process for MgB₂ has kept it from showing its full capability, and the junctions in this work were the first capable of such a task.

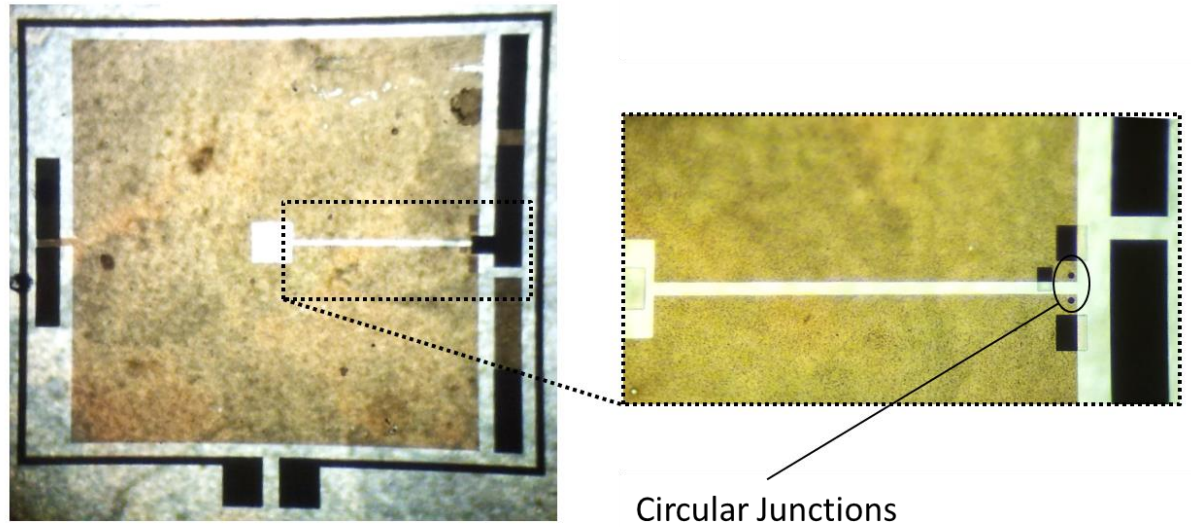


Figure 3.10. Optical image of a washer-type DC SQUID. The scale of the image (left) can be determined by the 0.1×0.1 mm square at the center. The zoomed in image (right) is without the wiring layer to show both circular junctions of $8 \mu\text{m}$ diameter.

The SQUIDs were fabricated in a similar way to the junctions using different mask patterns. The full process is again described in appendix A. Essentially the SQUID area is patterned into the bottom electrode and two square junctions are patterned in the second step. A wiring layer connects the top of these two junctions to the bonding pads used for measurement. An optical image of one device is shown in Fig. 3.10. The left hand side shows the full image while the right hand side shows a zoomed in image of the junctions before the wiring layer is deposited. The SQUID size is 1 mm per side on the outer loop and 0.1 mm on the inner loop. This particular device has a washer-type structure[107]. The junction sizes in Fig. 3.5 are circular junctions with $8 \mu\text{m}$ diameter.

The loop around the outside is used to generate a field for measurement, though an external coil was often used because it was easier to calibrate.

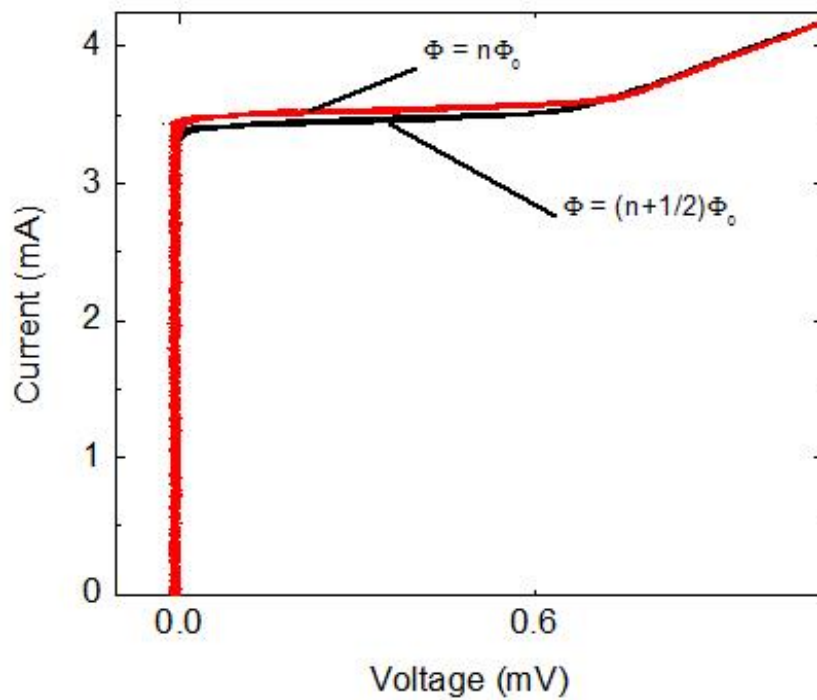


Figure 3.11. IV characteristic of a working planar-type DC SQUID with and without flux through the loop.

The measurement for these devices took place in the Cryocooler because it had the most efficient magnetic shielding and it was the only system with a coil for

generating a magnetic field perpendicular to the sample. The IV curve for one SQUID is shown in Fig. 3.11. This particular device did not exhibit any hysteresis above 15 K. The combined I_c of the two $4 \mu\text{m} \times 4 \mu\text{m}$ junctions was about $4 \text{ mA } \mu\text{A}$ while the $I_c R_n$ product was just below 2 mV . Using the change in I_c of the SQUID in a field and the formula for the design parameter of a SQUID,

$$\beta_L = 2I_0L/\Phi_0 \approx 1/(I_{cmax} - I_{cmin}) \quad (3.1)$$

where d is the length of the inside square, we get a β_L of 33. Using this parameter, we get an inductance of about 21 pH . Though not ideally designed we do see large voltage modulations with $\Delta V = 500 \mu\text{V}$ as shown in Fig. 3.12. Some modulation could be seen all the way up to 37 K with amplitude of a few μV . The period of modulations is about 20 mG which implies an effective area, A_{eff} , of about $1000 \mu\text{m}^2$. This is in good agreement with the geometry of the device, which has loop area of $900 \mu\text{m}^2$. The flux noise measurements are under way for these devices.

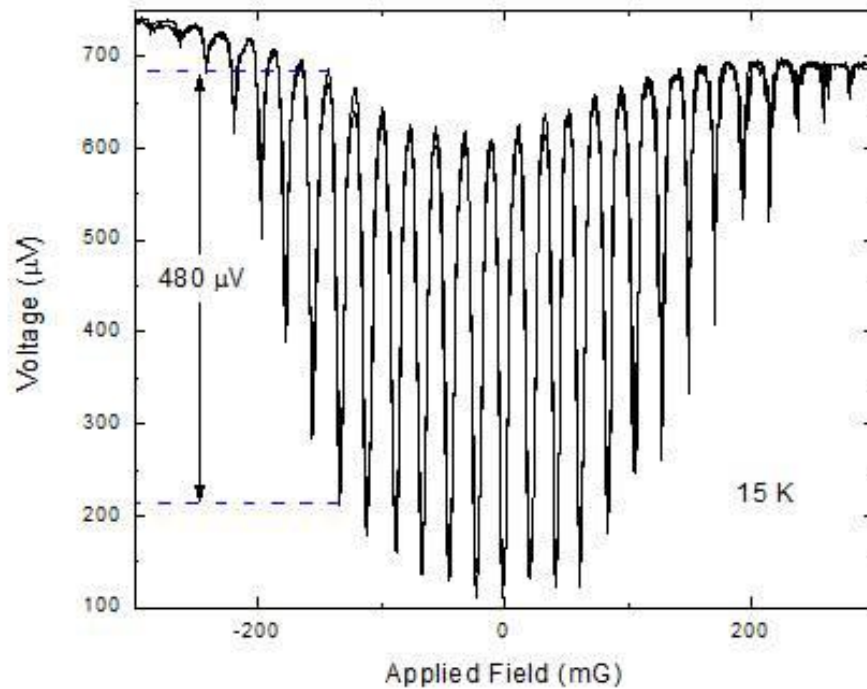


Figure 3.12. Voltage modulation of the planar-type SQUID referred to in Fig. 3.10.

The potential of MgB_2 to produce DC SQUIDs which perform better than low temperature devices calls for more investigation into this matter. The large inductance value of these devices leads to difficulties with the current junction process which has problems making junctions with lower J_c . The work done here is a big first step, along with the work in Chapter 4 and 5 to show that there is no intrinsic property of MgB_2 which makes it incongruous to SQUID applications. This means that the large gap parameters associated with MgB_2 which set the theoretical limit of the Josephson junction $I_c R_n$ product can likely be used to obtain devices with larger voltage modulations and

better sensitivity. Indeed the 500 μV modulations obtained in this work are already an achievement.

3.3 MgB_2 Josephson Junction Series Array

As with other devices presented in this thesis, the junction series array is another first step into the world of Josephson electronics. The applications of series arrays include the voltage standard [108], as well as microwave generators. Where the power radiated by a single junction is small, the power radiated by an array goes like the square of the number of junctions[109]. The latter application is especially interesting for MgB_2 because the frequency of the generated waves is limited by the value of the gap parameter. Any application which takes advantage of series of junctions requires that the parameter spreads for a single chip are very low. The current spread of MgB_2 junctions is not yet to the level it needs to be. As a result the series array can take on a new role of measuring this property spread without the need to measure many junctions individually.

Nb junction technology is advanced to the point of a junction density beyond 10,000 junctions/ cm^2 [110]. In order for MgB_2 to reach this advanced degree, a quick method of comparing results needs to be established. By measuring series arrays of junctions, the ability to qualitatively compare process changes becomes much easier.

The arrays were fabricated in a similar way to the single junctions and DC SQUIDS from previous sections of this thesis with another change in photomask patterns. The exact procedure and mask designs used are again outlined in Appendix A. Each sample consisted of three arrays of 100 junctions each. The square junctions of each of

the three arrays were 11 μm , 8 μm , and 4 μm per side. Analysis of the smallest junction array is presented here. The 100 junction array is broken into four sub-arrays of 10, 20, 30, and 40 junctions which can be measured individually. This allows for more precise measurements of the whole array.

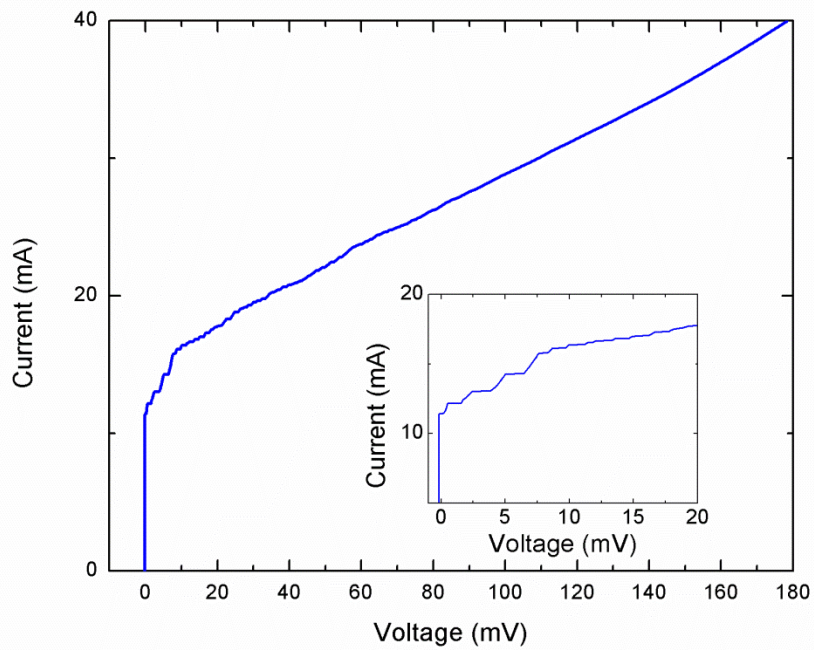


Figure 3.13. The IV characteristic of a 100-junction array. Inset shows a larger voltage scale with an equal current scale.

The measurement of these arrays was done in the Janis Research pulse tube cryocooler. The benefit of fabricating these arrays before the junction process is advanced

enough for application comes in the fact that the transition to the resistive state can be identified for every individual junction, giving a very precise measurement of junction I_c . This is a powerful tool to measure property spreads which can be used to judge a change in process design. An IV characteristic for a 100 junction array is shown in Fig. 3.13. The inset shows a zoomed in picture of the same Y-axis to exaggerate the features. Each perfectly horizontal section indicates the switching of a single junction to the resistive state. Instead of looking for the transition of each junction, further analysis can be done to measure the I_c spread much more easily. It is common to take the derivative of the current with respect to voltage when analyzing junctions. Here we take the derivative of the voltage with respect to the current and plot it as a function of current. The result is large peaks at the transition of each junction indicating a specific I_c . This derivative curve is shown in Fig. 3.14. A logarithmic scale is used on the y-axis to show the large peaks. An interesting feature to note here is that the height of the peaks generally diminish with increasing current. This is likely because the $I_c R_n$ product is decreasing for higher I_c . The average J_c of this chip is very high at 150 KA/cm^2 , so it is likely that the junctions with higher I_c are less dominated by MAR and likely moving into the strong link regime. Further analysis on more samples are needed to verify this.

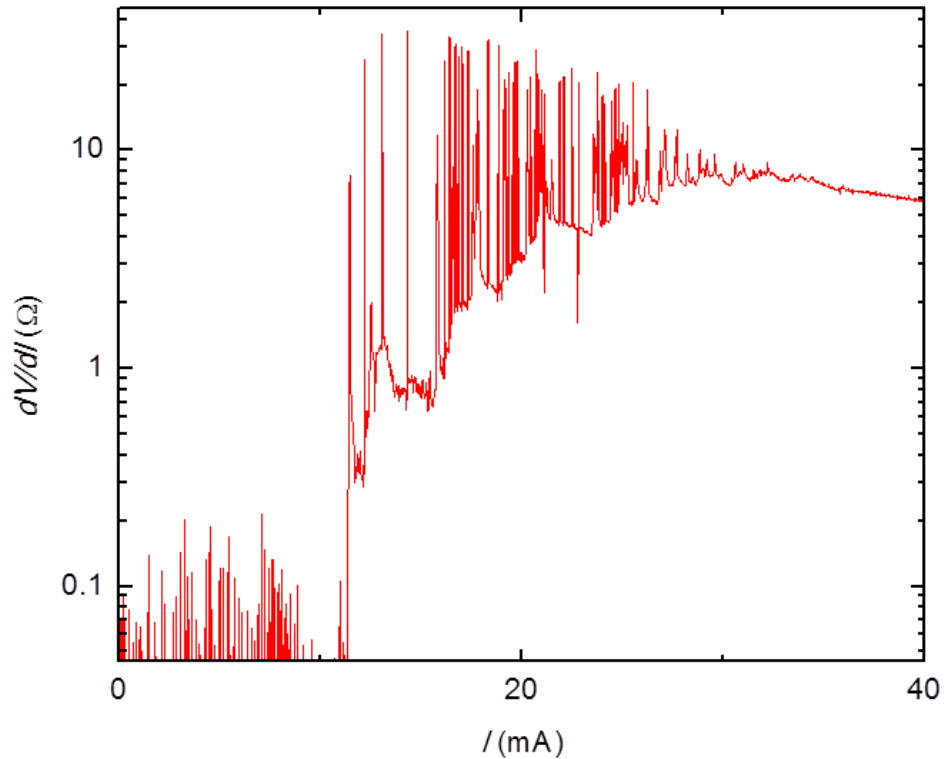


Figure 3.14. dV/dI verse current for the 100-junction array described in Fig. 3.12. Each vertical spike indicates a junction transition. (Note the logarithmic scale).

To improve on the easiness associated with this method of measuring property spreads, the array can be broken down and measured in its smallest components. This would be four sub-arrays, one each with 10, 20, 30, and 40 junctions. The transitions are much easier to spot this way and measurement becomes even more accurate. Fig. 3.15 shows four derivate curves which measure the same 100 junctions as in Fig. 3.14. Even

with 40 junctions being measured, the density of the transitions is much lower, allowing for more precise measurement of junction I_c . These four curves were used to generate the histogram in Fig. 3.16. The histogram shows a distribution where the average I_c for this array is 22.4 mA and the standard deviation is about 12 mA. The fact that the deviation is so large is not too discouraging considering that the I_c is so high. The thin barrier is more likely to have random shorts and be overall, less uniform. The poor property spread of this sample helps to validate this method as a means for calculating the spread. It is believed that making the barrier thicker will make a significant improvement for the property spreads. More investigation is necessary to prove this.

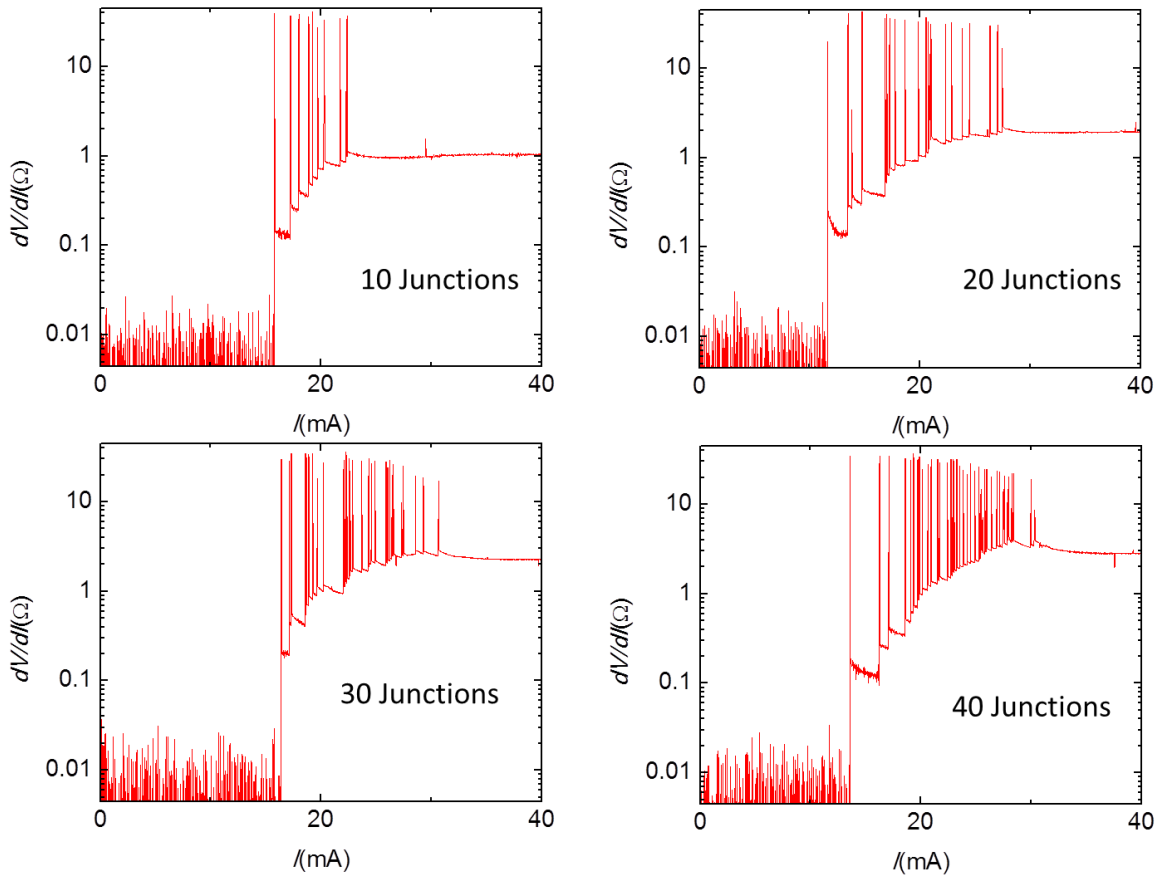


Figure 3.15. dV/dI versus current for the 100-junction array described in Fig. 3.12. The array has been measured as 4 sub-arrays with the number of junctions in each sub-array indicated.

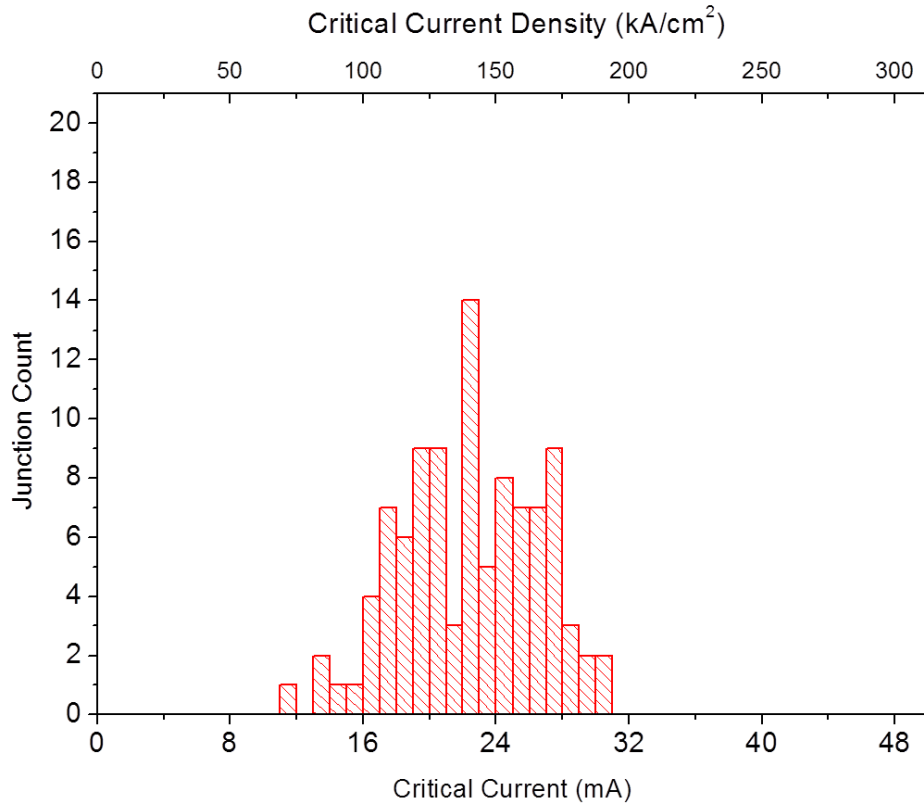


Figure 3.16. A histogram generated from the data collected using the dI/dV curves in Fig. 3.14.

CHAPTER 4

STUDY OF COMPONENTS FOR MAGNESIUM DIBORIDE RSFQ DIGITAL CIRCUITS

4.1 Introduction

Superconducting integrated circuits (SICs) outperform their semiconductor counterparts in maximum operating frequencies. In applications where high-performance is most desired, the benefit of increasing speed and decreasing power consumption may outweigh the cost of operating at cryogenic temperatures, especially as cooling technology improves and better superconductors with higher superconducting transition temperature, T_c , are developed [111]. Nb currently sets the standard for SIC [42] for established fabrication technique but has its drawbacks in its low critical temperature and relatively small superconducting gap parameter compared to YBCO, MgB₂, and other superconductors developed later. YBCO, a high temperature superconductor has also shown promise [112-114], but could not overcome the difficulties of a reliable multilayer process. In addition, their strong anisotropic properties and *d*-wave superconducting pairing symmetry also restrict the quality of Josephson junctions (JJs), an essential part of SICs [32]. MgB₂, a simple metallic compound and *s*-wave BCS superconductor with a

critical temperature over 39K and superconducting gaps larger than 2 meV at 4 K could prove to be a material superior than Nb for the future of SiCs.

All-MgB₂ Josephson junctions have been previously reported [78] with the critical current density, J_c , up to 275 kA/cm² and the product of the the critical current, I_c , and the normal resistance, R_n , near 3 mV at low temperature. The junctions have I_c above 35 K with hysteresis exhibited below 12-15 K. More recently an additional MgB₂ wiring layer has been utilized without any loss in junction performance. The absence of hysteresis above 12-15 K allows for a large range of temperatures at which circuits can be designed to work. To this end, an in-depth study has been carried out to obtain all parameters necessary for circuit design at many temperatures. The I_c and normal state resistance, R_n , of junctions are needed for design and simulation as well as the inductance of a superconducting MgB₂ microstrip. The additional superconducting layer has allowed for devices which help resolve design issues. Included in these devices are DC SQUIDS which can be used to measure the inductance of an MgB₂ thin film microstrip [115].

4.2 Experiment

4.2.1 Josephson Junctions

The MgB₂ JJs reported were fabricated using hybrid physical-chemical vapor deposition (HPCVD) which requires substrate temperatures near 700 °C for the most optimal films [116]. A trilayer was made on SiC substrate consisting of

MgB₂/MgO/MgB₂ layers which were then passivated by a, 30 nm-thick Au layer to protect it during patterning. Though the MgB₂ native oxide serves well as a tunnel barrier in MgB₂/I/Pb junctions [69], it does not survive the high temperature during the deposition of the counter electrode or wiring layer. An MgO barrier was deposited *ex situ* to the bottom MgB₂ electrode using RF magnetron sputtering. UV lithography and Ar ion milling were used to pattern the base electrode and define the junction area. MgO was sputtered as an insulating layer between the base electrode and the wiring layer. After removing the Au passivation layer by ion milling, another MgB₂ film was deposited followed by a new Au contact layer which was subsequently patterned into the wiring layer. Each chip contains 18 square-shaped junctions ranging in size from 16 μm² to 4900 μm².

4.2.2 DC SQUIDS to Measure Inductors

To measure the inductance of an MgB₂ microstrip, a DC SQUID is designed such that the only non-negligible contribution to the inductance is from the wiring layer. This layer is patterned into a microstrip connecting the counter electrodes of the two JJs of the SQUID. The common base electrode of the two junctions is a large square grounded conducting plane 300 μm per side. Mirror current generated in this layer will minimize the inductance of the microstrip [31]. Each chip contains 6 devices varying the SQUID loop area by changing the width and length of the microstrip. The SQUID loop is perpendicular to the surface of the film with the area determined by the distance between the two junctions and the thickness of the MgO insulating layer which separates the grounded conducting plane and the wiring layer. Included in the patterning are contacts to

apply a current across the microstrip as well as across the SQUID to apply a bias and measure the voltage.

4.2.3 Shunt Resistor

For MgB₂ circuits to work at low temperatures below 12-15 K, an external resistive shunt layer is needed for additional damping of the junctions. Using the resistively and capacitively shunted junction (RCSJ) model, the damping parameter, β_c , is dependent on I_c , R_n and capacitance, C , of the junction [35]. The easiest method to modify β_c is to add a resistance in parallel with the junction, essentially modifying R_n . This is done by adding a metallic layer of known sheet resistance into the fabrication process. This layer can be patterned to achieve an exact resistance and connected to junction electrodes in parallel with the junctions. A comparison was done of the temperature dependence of many materials to determine the best material for shunting MgB₂ JJs. The materials were all deposited using DC magnetron sputtering.

4.3 Results

All measurements were taken using either a Janis Research pulse tube cryocooler, or in a custom built cryoprobe. In the case of the cryocooler, magnetic shielding was inefficient, thus constant thermal cycling above T_c was performed to get rid of trapped flux in the film.

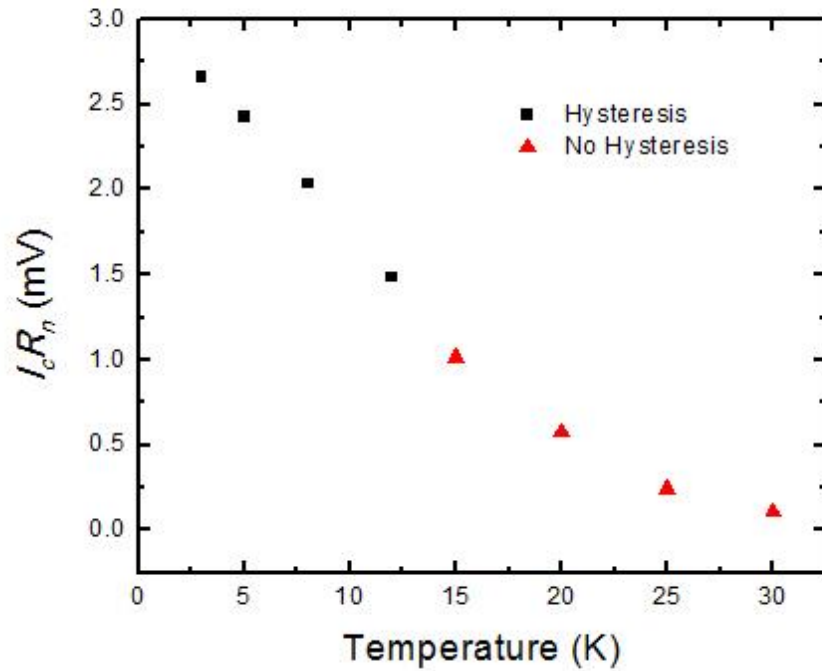


Figure 4.1. Temperature dependence of the $I_c R_n$ product for a typical MgB_2 Josephson Junction.

4.3.1 Josephson Junctions

The transport through the $\text{MgB}_2/\text{MgO}/\text{MgB}_2$ junctions is dominated by MAR which could be sufficient for the circuits if well under control [117]. The $I_c R_n$ product is much higher in the over damped (absence of hysteresis) state than typical SIS junctions. Fig. 4.1 shows the temperature dependence of the $I_c R_n$ product of a typical MgB_2 JJ with an MgB_2 wiring layer. For this process, the hysteresis disappears above 12-15 K which

still leaves $I_c R_n$ near 1.5 mV without hysteresis. A major drawback for these junctions is the large on-chip junction property spread. Fig. 4.2 shows the dependence of J_c on the designed junction area. The spread for area between $16 \mu\text{m}^2$ and $25 \mu\text{m}^2$ is below 15% which will suffice for initial circuit design and testing. Work is ongoing to further improve the parameter spread of the MgB_2 JJ devices.

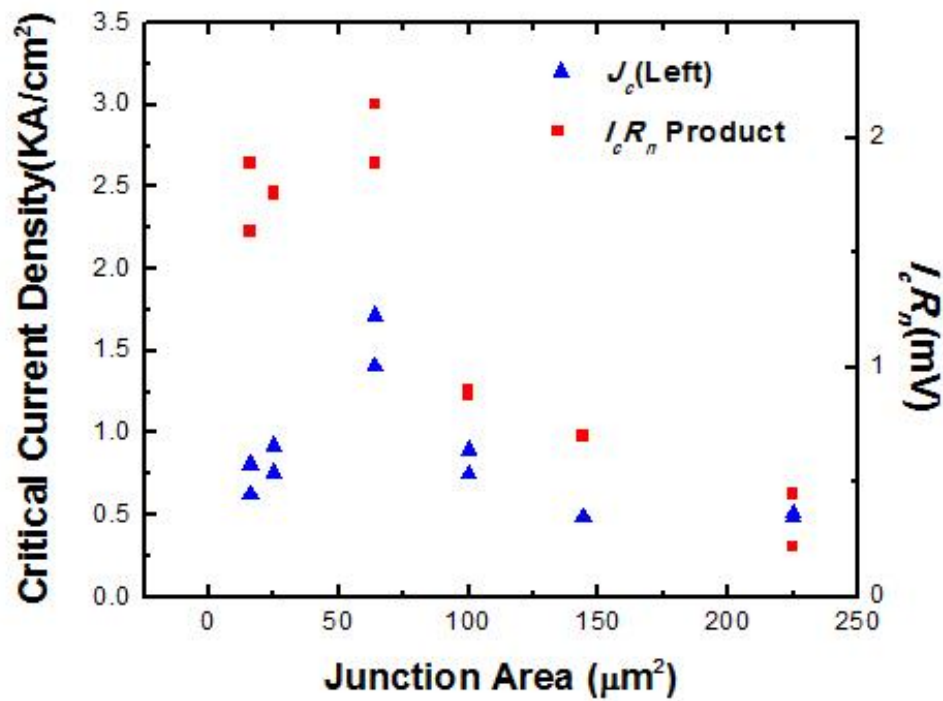


Figure 4.2. Parameter spreads of MgB_2 Josephson Junctions from a single chip after the introduction of a superconducting wiring

4.3.2 Inductors

The magnetic field used to modulate the voltage across the DC SQUID is generated by passing a current through the top arm of the SQUID (the microstrip). By taking the period of oscillations from the DC SQUIDs, we can calculate the inductance per square, L_{sq} , of the MgB₂ microstrip. One period of voltage modulation corresponds to a single flux quantum, $\Phi_0=2.067 \times 10^{-15}$ Wb, through the SQUID loop. By using the definition of inductance $L= \Phi/I$, we get the inductance of the microstrip. Taking geometry into account can yield L_{sq} . Fig. 4.3 shows the modulation of the IV curve of a SQUID with no magnetic flux and with $1/2 \Phi_0$ as generated by an external coil. The inset shows the voltage modulations of the SQUID when passing a current through the microstrip (without external field) and constantly biased at 1.5mA.

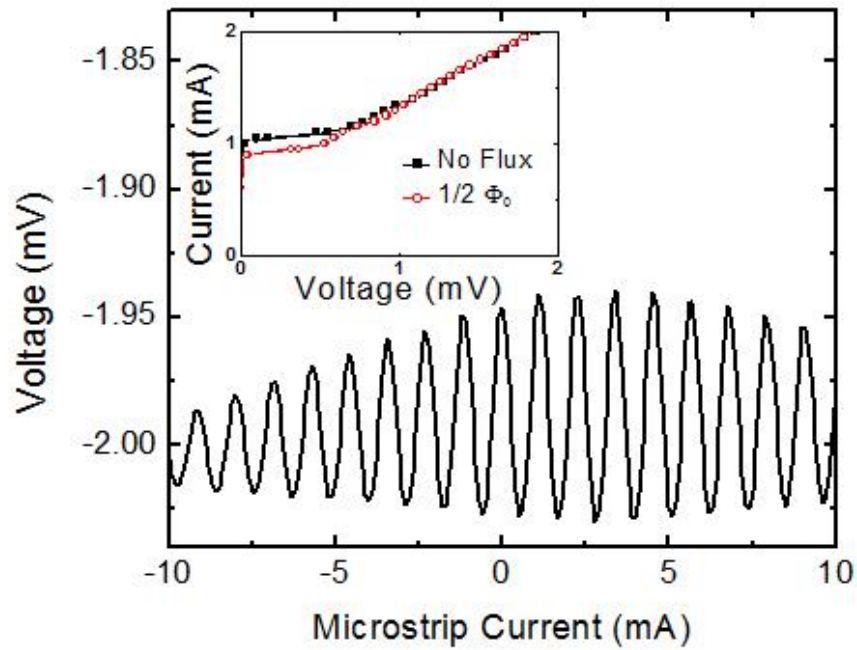


Figure 4.3. Voltage modulation of an MgB₂ DC SQUID using the microstrip to generate the field. Inset shows IV curves for maximum and minimum flux in the loop using an external field.

Measurement of the DC SQUIDs resulted in very consistent values of inductance of an MgB₂ microstrip. By controlling the thickness of the MgO insulating layer we can control the L_{sq} of an MgB₂ microstrip. The lowest L_{sq} found was 0.18pH at low temperatures for a 45 nm MgO layer and will be used in the circuit design because it allows the most freedom to change the microstrip sizes.

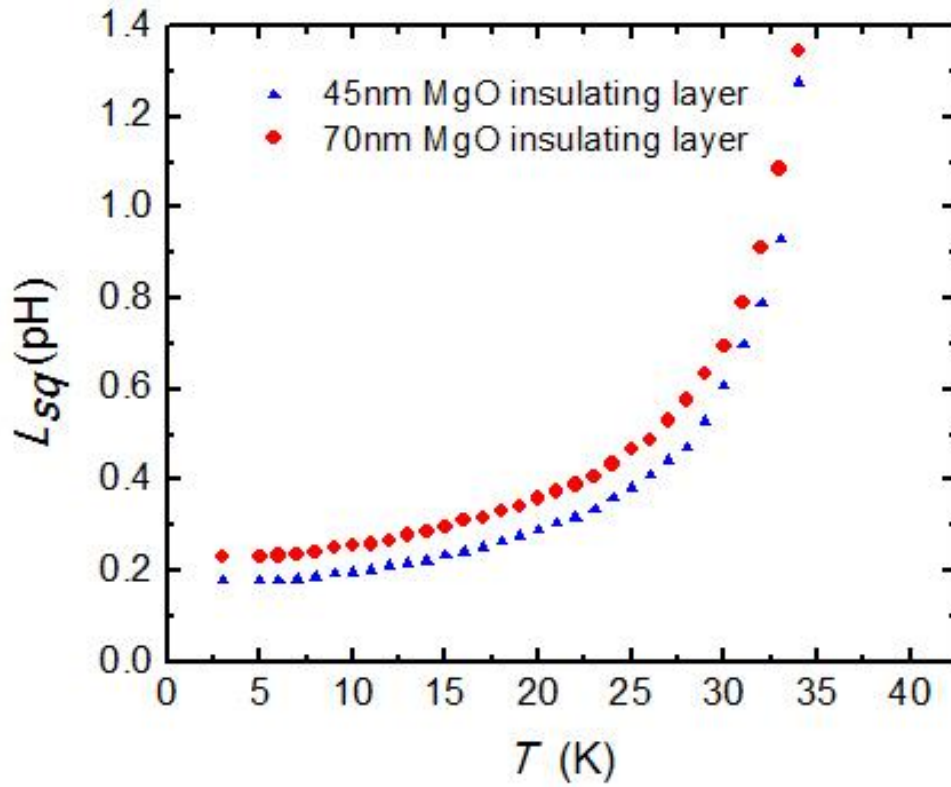


Figure 4.4. Temperature dependence of L_{sq} for two devices with different thickness insulating layer. Triangles show data from a chip with 45nm of MgO and circles show data from a chip with 70nm of MgO.

The inductances of the microstrips in a circuit need to be designed for a specific operating temperature. The DC SQUIDS in this work operate from low temperatures up to 35 K. This allows for temperature dependence measurements of the MgB₂ microstrips. Fig. 4.4 shows L_{sq} as a function of T for two different thicknesses of the MgO insulating layer. In theory, the thinner the MgO, the lower the inductance, but the thinnest film must

be thick enough to completely insulate the two conducting layers. This thickness was found to be between 45 nm and 130 nm. MgO thickness outside of this region has not yielded successful devices.

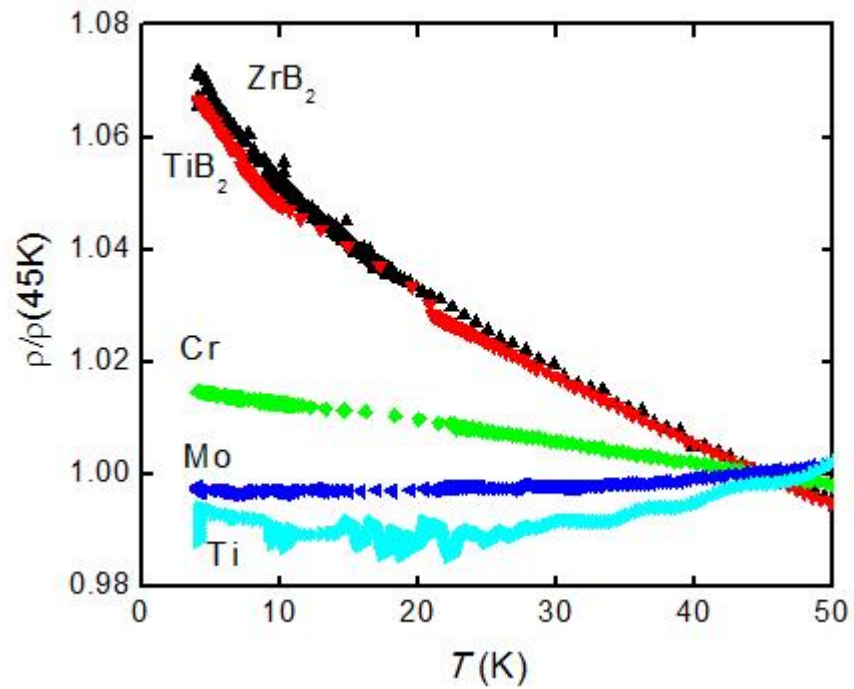


Figure 4.5. Temperature dependence comparison of different materials with good potential for MgB₂ devices.

4.3.3 Shunt Resistor

Fig. 4.5 shows the normalized resistivity of all the materials tested in this study. A material was needed which has a relatively constant resistivity in the temperature region below the T_c of MgB_2 . Mo turned out to have almost constant resistivity from 50 K all the way down to 4.2 K.

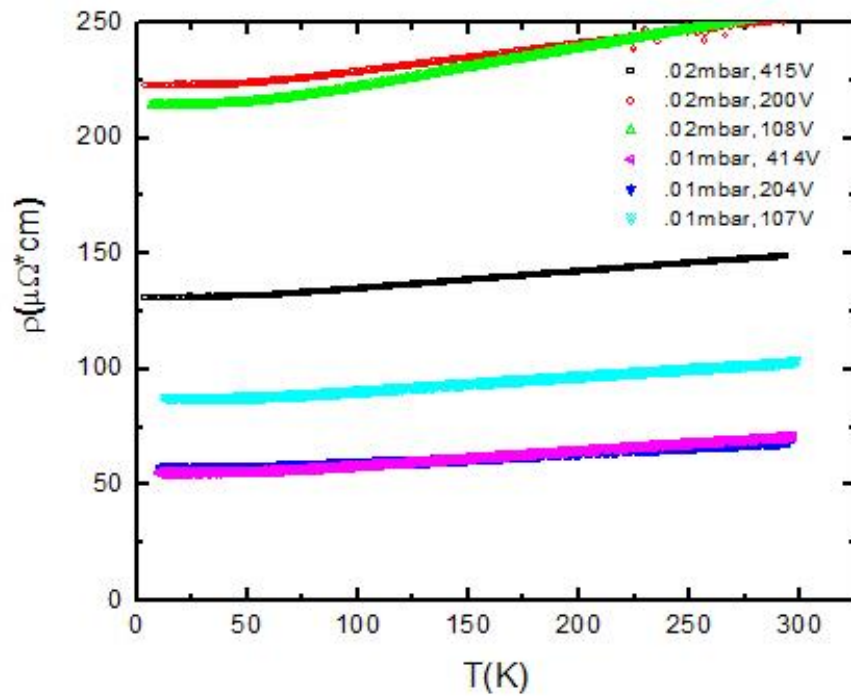


Figure 4.6. Resistivity dependence on temperature for different growth parameters of Mo.

Fig. 4.6 shows the resistivity versus temperature of Mo thin films deposited under different deposition conditions. The lowest resistivity was found to be $55 \mu\Omega\text{cm}$ in Mo films deposited in 0.01 mbar Ar partial pressure with a sputtering voltage of ~ 400 V. This resistivity will be used to design shunt resistors for JJs with hysteresis. As with inductance, lower resistivity allows more freedom in resistor geometry and size. Even more important was the compatibility of Mo to HPCVD growth of MgB_2 thin films on top of it, especially because of the high MgB_2 growth temperatures which would cause unwanted reactions with Mg for most materials. Fig. 4.7 is a resistance versus temperature curve of an MgB_2 film as grown on a Mo substrate, showing good superconducting property of the MgB_2 film. An obstacle to be overcome is the MgB_2 native oxide which prevents good contact to the Mo thin films. Fig. 4.8 shows the IV curve of an intersection of an MgB_2 strip and overlaying Mo strip, both about 0.3 mm wide. From the non-linearity in the gap region of MgB_2 around 2 mV it is clear that transport across the interface is dominated by the single-particle tunneling. It is shown on the same plot that we can avoid this non-Ohmic contact with an *in situ* ion milling step prior to the Mo deposition.

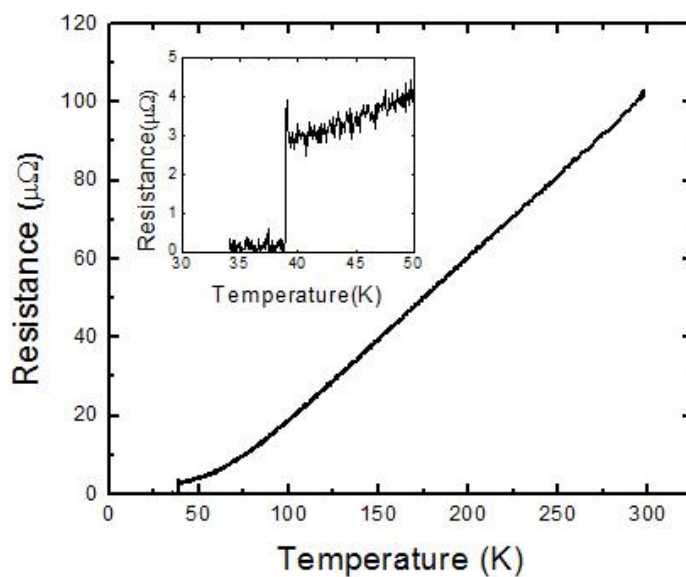


Figure 4.7. Resistance vs Temperature of an MgB_2 film as grown on top of a Mo substrate.

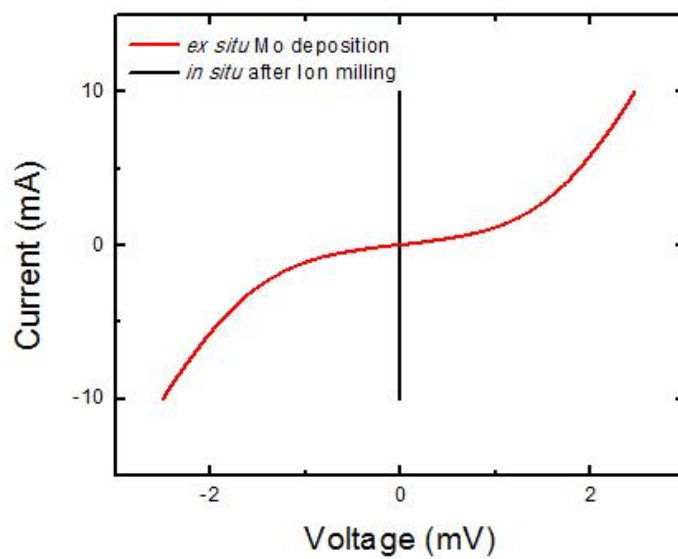


Figure 4.8. IV curve of MgB_2/Mo intersection for *ex situ* grown Mo and *in situ* grown Mo after ion milling through the native oxide.

4.4 Conclusion

The necessary parameters for the design of MgB₂ circuits, junction property spread, microstrip inductance, and shunt resistors, are studied, which can be used for circuits operating at either low or high temperatures to show the full potential of MgB₂ in high speed superconducting circuit applications. The ongoing pursuit of improved on-chip junction property spreads will help to achieve the maximum operating speeds at low temperature. A RSFQ circuit has been designed and fabricated using the microstrip inductance values reported here, for operation around 20 K. Data from this circuit is still being collected to be reported at a later time.

CHAPTER 5

MEASURING THE PENETRATION DEPTH OF MAGNESIUM DIBORIDE USING JOSEPHSON JUNCTIONS AND SQUIDS

5.1 Introduction

The penetration depth λ , which characterizes the distance into a superconductor over which a magnetic field decays is a fundamental property of the superconductor[3]. It is of both scientific and technological significance to measure the penetration depth of superconductors precisely. For example, the temperature dependence of the penetration depth $\lambda(T)$ played critical roles in revealing the *d*-wave pairing symmetry of high- T_c cuprate superconductors[10], and the two gap nature of MgB₂[118]. Further, the penetration depth is an important parameter for various applications of superconductors. The penetration depth affects the inductance of a superconducting microstrip or loop, which is an essential element of superconducting digital circuits. For superconducting RF cavities, it has been proposed that the RF breakdown field can be enhanced by coating the cavity with a multilayer consisting of superconducting layers thinner than the penetration depth[119]. A multiband model for the penetration depth of MgB₂ predicted that the *c*-axis λ is about 40 nm in the clean limit, but can be as high as 300 nm in the dirty limit[120]. The reported experimental values of $\lambda(0)$ for MgB₂ have been widely varied in the literature, ranging from 40 nm measured using a microwave technique[24] to 115 nm measured using an MFM technique[121]. Because the absolute value, anisotropic nature,

and temperature dependence of λ all depend on the cleanness of the film it is important to measure the penetration depth in the cleanest MgB₂ samples. In addition, the $\lambda(0)$ values extracted from some measurements depend on whether the single-band or multiband model is used[3]. It is desirable to obtain the $\lambda(0)$ value from experiment whose interpretation does not depend on the single-band or multiband model. In this paper, we report penetration depth measurements of clean MgB₂ films using two techniques of different mechanisms, one utilizing MgB₂ single Josephson junctions and the other using MgB₂ DC SQUIDs. Neither method requires the assumption of single-band or multiband model for the extraction of the $\lambda(0)$ value. Both techniques show that the absolute value of $\lambda(0)$ is around 40 nm.

The first approach measures the period of modulation of the critical current, I_c , of a MgB₂ Josephson junction by a magnetic field applied perpendicular to the current (see inset to Fig. 5.1), which shows a diffraction-like pattern. The I_c minima occur when integer numbers of magnetic flux quanta pass through the barrier area, which is shown as a rectangular area enclosed by the dashed line in the inset to Fig. 5.1. The length of the rectangle is that of the junction, L , and the width of the rectangle is the sum of the barrier thickness, t , and the penetration depths of both superconducting electrodes, λ_1 and λ_2 [35]. The second approach uses an all-MgB₂ DC SQUID to measure the inductance of an MgB₂ microstrip. A schematic diagram of the device along with an optical image is shown in Fig. 5.2. The microstrip is the line connecting the two all-MgB₂ junctions. A current scanned through the microstrip induces a magnetic field, which causes a voltage oscillation across the SQUID biased at a constant current. The period of oscillation

corresponds to one magnetic flux quantum passing through the SQUID loop, which can be used to determine the inductance of the microstrip and extract the penetration depth. Both methods measure the penetration depth in the normal direction of the film, which in the present case is the c direction of MgB_2 .

5.2 Experiment

The Josephson junction for the $I_c(B)$ measurement was made by first growing a c -axis oriented MgB_2 film by hybrid physical-chemical vapor deposition (HPCVD) on $\text{SiC}(0001)$ substrate[68]. The thickness of the film was 120 nm. For junctions with Nb or Pb top electrode, the barrier is the native oxide of MgB_2 formed in air after the film was taken out of the growth reactor. The $\text{MgB}_2/\text{I}/\text{Pb}$ junctions were made by painting the film with Duco cement to expose a 0.3 mm-wide strip of MgB_2 followed by thermally evaporating 0.3 mm-wide Pb strips through a shadow mask perpendicular to the MgB_2 strip[69]. The $\text{MgB}_2/\text{I}/\text{Nb}$ junctions were made by depositing the Nb electrode layer using DC magnetron sputtering on top of the MgB_2 native oxide. The $\text{MgB}_2/\text{MgO}/\text{MgB}_2$ Josephson junctions were fabricated using an RF magnetron sputtered MgO as the barrier layer between two c -axis oriented MgB_2 electrodes made by HPCVD. Both the $\text{MgB}_2/\text{I}/\text{Nb}$ and $\text{MgB}_2/\text{MgO}/\text{MgB}_2$ junctions were defined by standard UV photolithography and argon ion milling, ranging in size from $4 \mu\text{m} \times 4 \mu\text{m}$ to $70 \mu\text{m} \times 70 \mu\text{m}$, similar to the fabrication process reported earlier[78]. The DC SQUIDs were fabricated using the same process as the $\text{MgB}_2/\text{MgO}/\text{MgB}_2$ junctions except that the devices always had an MgB_2 wiring layer. The fabrication process is pictured in Fig. 5.3,

and an in depth description is given in Appendix A. The MgB_2 bottom layer also serves as a grounded conducting plane whereas the MgB_2 wiring layer doubles as a superconducting microstrip. A sputtered MgO layer between the counter electrode and the wiring layer determines the width of the SQUID loop, which ranged from 40 - 80 nm. The length of the loop is determined by the distance between the two $\text{MgB}_2/\text{MgO}/\text{MgB}_2$ junctions and ranges from 10 μm to 80 μm .

5.3 Results

The $\text{MgB}_2/\text{I}/\text{Pb}$ junctions were measured at 2 K in a Quantum Design PPMS System. An in-plane magnetic field was applied by a custom-made superconducting NbTi coil with a calibrated field rate of about 1300 G/A. A custom-made μ -metal magnetic shield covered the coil and the sample within. The $\text{MgB}_2/\text{I}/\text{Nb}$ and $\text{MgB}_2/\text{MgO}/\text{MgB}_2$ junctions and the DC SQUIDs were measured from 3.2 K to near T_c in a Janis Research Pulse Tube Cryocooler with a custom-built Cu coil and magnetic shielding.

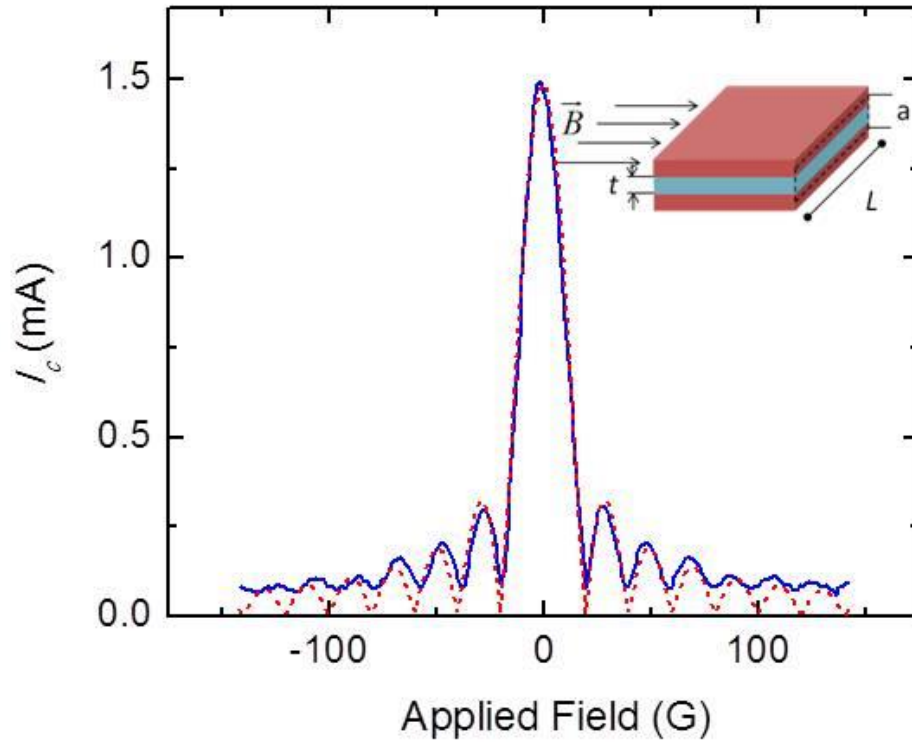


Figure 5.1. The critical current of an MgB₂/Native Oxide/Nb junction modulated by applied magnetic field (solid line) fitted by a theoretical fit with $\lambda = 37$ nm (dotted line). Inset shows a schematic of the junction in an external magnetic field \vec{B} .

Fig. 5.1 shows the modulation of I_c by applied magnetic field (the blue curve) for a MgB₂/I/Nb junction. An I_c suppression of 94 % by the applied field was observed at ± 19.3 G and I_c minima occur at approximately $\pm n\Delta H$, where n is a positive integer and the period $\Delta H \sim 19.6$ G. The experimental data can be fit well with a theoretical curve of the Fraunhofer pattern except for the incomplete I_c suppression likely due to

measurement noise and non-uniform current density across the junction area. The penetration depth can be extracted from ΔH using the following formula[35]

$$\Delta H = \frac{\Phi_0}{L(\lambda_1 \tanh \frac{d_1}{2\lambda_1} + \lambda_2 \tanh \frac{d_2}{2\lambda_2} + t)} \quad (5.1)$$

where $\Phi_0 = h/(2e) = 2.068 \times 10^{-15}$ Wb is the flux quantum, and d the electrode thickness with the subscripts 1 and 2 differentiating between the bottom and top electrodes, respectively. This formula is applicable even when d_1 and d_2 are smaller than the penetration depth. Taking the values $t = 2$ nm [78], $d_1 = 120$ nm, $d_2 = 250$ nm, and $\lambda_2 = 50$ nm for Nb[122], Eq. (5.1) gives $\lambda_1 = 37 \pm 4$ nm for MgB₂. The error arises mostly from the barrier and bottom electrode thicknesses. The top electrode is sufficiently thick to make the hyperbolic tangent term close to unity, thus the dependence on its thickness negligible. The non-uniformity of critical current density across the junction may also lower the measurement accuracy of the modulation period. It should be noted that Eq. 5.1 requires that the length of the junctions normal to the field direction is small compared to the Josephson penetration depth, λ_J . For junctions with Nb and MgB₂ top electrodes, the junction length is at least an order of magnitude smaller than λ_J . In the case of Pb junctions, it is similar to λ_J , which introduces additional error due to self-field effects. Table 5.1 shows the calculated penetration depths for 12 junctions with three different types of top electrode materials. The penetration depth ranges from 37 – 67 nm, with the most results falling close to 39 nm. The larger values in this range came from the Pb junctions, which may have a much larger error due to the long-junction effects.

Table 5.1. Penetration depth of MgB₂ calculated from 12 square-shaped junctions of different length and top electrode materials.

Top Electrode Material	Junction Length (μm)	Calculated Penetration Depth (nm)
Pb	250	67.1
Pb	250	40.2
Pb	250	38.0
Pb	250	52.2
MgB ₂	8	46.3
MgB ₂	12	37.2
MgB ₂	15	50.2
MgB ₂	20	39.9
Nb	20	42.0
Nb	12	37.0
Nb	12	38.1
Nb	10	35.3

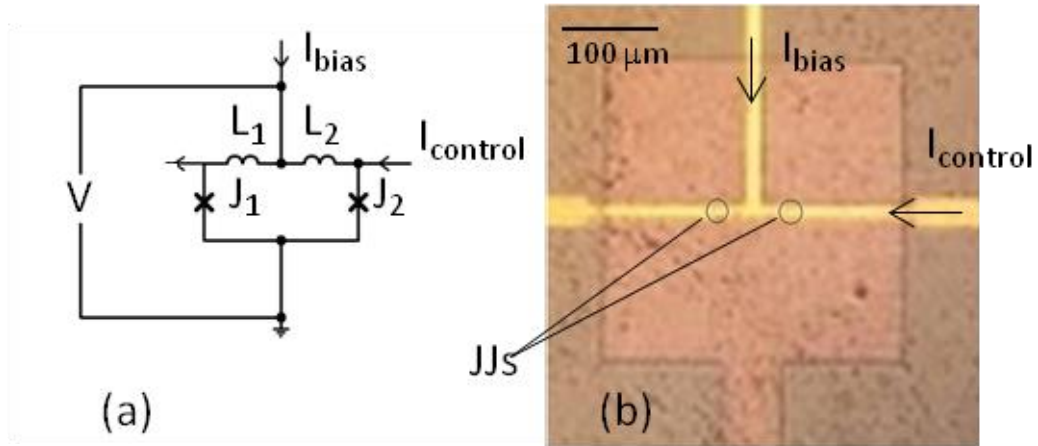


Figure 5.2. (left) Schematic and (right) optical image of DC SQUID.

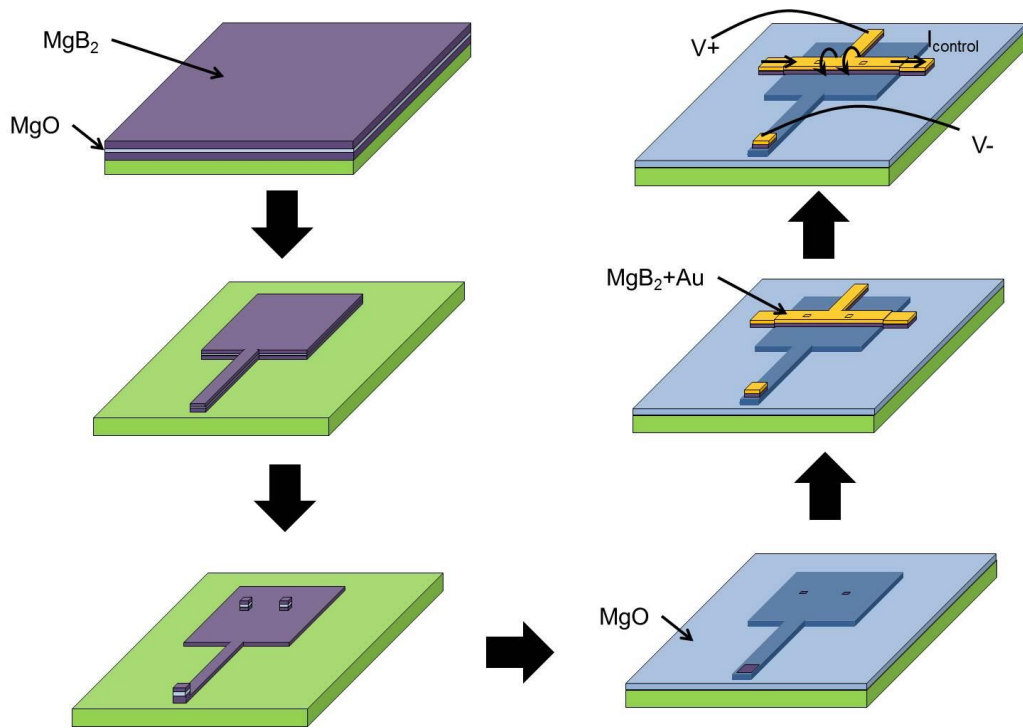


Figure 5.3 Fabrication process of a SQUID.

The measurement of a SQUID can be seen by the top right drawing in Fig. 5.3. The voltage is measured across the SQUID while a current is ran across the microstrip inductor. A typical result from the DC SQUID measurement is shown in Fig. 5.4. The SQUID voltage at different current biases and $T = 3.2$ K is plotted as a function of the control current I through the microstrip. The current bias of the SQUID was applied between the bottom and top electrodes and the control current flows through the superconducting microstrip in the top layer across the electrodes of the two $\text{MgB}_2/\text{MgO}/\text{MgB}_2$ Josephson junctions. When the control current was scanned, periodic modulations of the SQUID voltage, as large as 0.5 mV in magnitude, were observed. The shape and amplitude of the modulation depends on the bias current, and the period ΔI corresponds to one magnetic flux quantum passing through the SQUID loop. The phase shift by 180 degrees between the low and high bias currents is related to the junction capacitance, which does not affect the modulation period. More typical modulation is seen when the device is biased well above the hysteresis region (top curve). For the SQUID in Fig. 5.4, a period $\Delta I = 12.3$ mA is obtained. Almost all the magnetic flux generated by the microstrip current is through the SQUID loop, and the inductance $L = \Phi_0/\Delta I = 0.17$ pH.

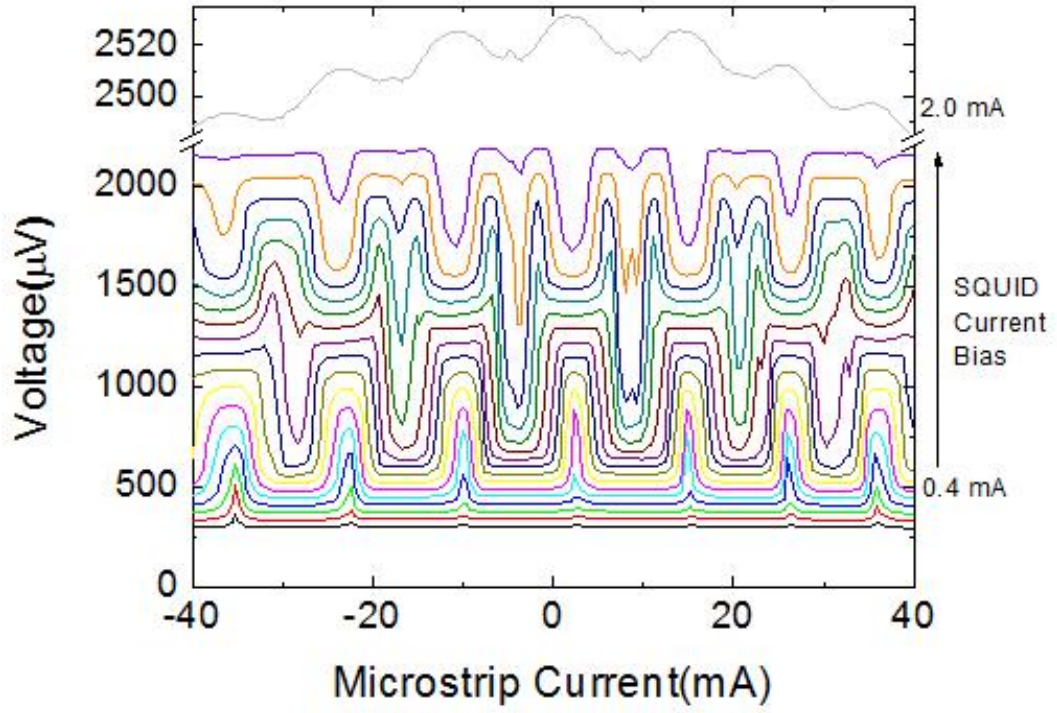


Figure 5.4. Voltage across a DC SQUID modulated by microstrip current at 3.2 K. The SQUID is biased at various current from 0.4 mA to 2 mA.

The inductance of a superconducting line on a superconducting ground plane is defined as follows [31]:

$$L = \frac{l\mu_0 d\kappa}{w} \left[1 + \frac{\lambda}{d} \left(\coth \frac{b_1}{\lambda} + \coth \frac{b_2}{\lambda} \right) \right], \quad (5.2)$$

where d is the distance between the ground plane and the line as defined by the thickness of the insulating layer between them, l the length, w the width, and b_1 the thickness of the line, b_2 the thickness of the ground plane, and κ the fringe factor of the configuration[31]. Using the values $l = 20 \mu\text{m}$, $w = 10 \mu\text{m}$, $d = 75 \text{ nm}$, $b_1 = 120 \text{ nm}$, $b_2 = 120 \text{ nm}$, and $\kappa = 0.9$ for the SQUID in Fig. 3, Eq. (5.2) yields $\lambda = 36 \text{ nm}$ at $T = 3.2 \text{ K}$. Five SQUIDs have been measured, and the absolute values of $\lambda(0)$ obtained ranged from 36 nm to 40 nm.

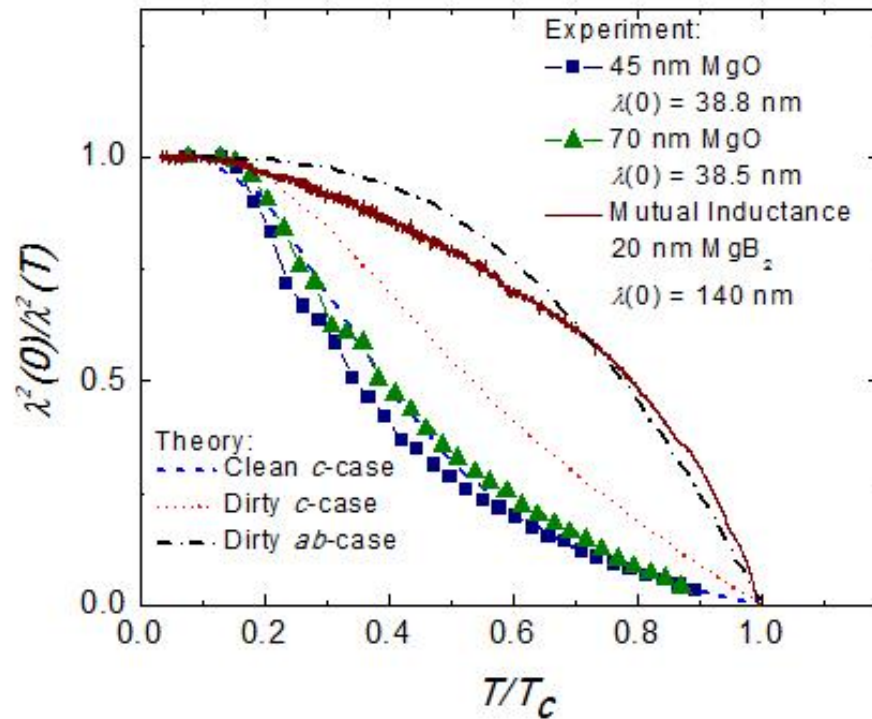


Figure 5.5. Temperature dependence of normalized inverse-squared penetration depth from the SQUIDs measurement compared with the theory proposed by Golubov *et al.* (Ref. 5) for the clean (dashed line) and dirty (dashed double dotted line) limits in the *c*-axis and dirty limit (dashed-dotted line) in the *ab*-axis. Also plotted is the result of a mutual inductance measurement (solid line) on a 20 nm-thick MgB₂ film.

The DC SQUID measurement was performed over a wide temperature range from 3.2 K to near T_c . At low temperatures when there is hysteresis in the SQUID $I - V$ curves, the period was taken when the SQUID was biased just above the hysteresis range; otherwise the period was taken when the SQUID was biased to give the maximum modulation amplitude. The temperature dependence of the penetration depth, plotted in the form of $\lambda^2(0)/\lambda^2(T)$, is shown in Fig. 5.5 for two SQUIDs with different MgO insulating layer thicknesses, $d = 45$ nm and $d = 70$ nm, respectively. The two curves are consistent with each other, confirming the robustness of the method. Also plotted in the figure are the predictions for λ_c and λ_{ab} from a two-band theory by Golubov *et al.* for MgB₂ in the clean and dirty limits[120]. The experimental data follow the clean limit λ_c curve closely. An inflection point can be seen around 12 - 15 K in the experimental curves, which may reflect the intrinsic T_c of the π band as Golubov *et al.* have predicted.

The single Josephson junction and DC SQUID methods described in this paper measure the penetration depth using different mechanisms. For the magnetic field modulation of I_c in a Josephson junction, I_c oscillates because the field changes the phase difference between the two superconducting electrodes, which depends on the barrier thickness and the field penetration into the superconductors. In a DC SQUID, the periodic oscillation of the voltage occurs because the magnetic flux in the SQUID loop must be an integral number of flux quanta. When the superconducting microstrip is used to generate the magnetic flux through the SQUID loop, the penetration depth is extracted

from the kinetic inductance of the superconducting microstrip, which depends on the superconducting carrier density. The penetration depth value obtained from the DC SQUID measurement is more accurate than from the single Josephson junction measurement, because the modulation period can be more accurately measured from more modulation cycles and is not prone to the current uniformity or short-junction limit of the Josephson junctions. This is the likely reason that the spread of the measured λ values from the DC SQUID measurements are within 10%, better than that from the Josephson junction measurements. The fact that the two methods with completely different mechanisms give the same results is a strong indication that the value we have obtained, $\lambda(0) \sim 40$ nm, is correct.

According to the first-principles calculation of Golubov *et al.*, $\lambda_{ab} = 39.2$ nm and $\lambda_c = 39.7$ nm in the clean limit and $\lambda_{ab} = 105.7$ nm and $\lambda_c = 316.5$ nm in the dirty limit at $T = 4$ K for MgB₂. The techniques in this work measure λ_c , and the result agrees with the theoretical prediction in the clean limit. Indeed, we have used tunnel junctions from the HPCVD films to observed a distribution of the gap values, which is only observable in clean MgB₂ films[22]. Further, using a sapphire resonator at 18 GHz Jin *et al.* have shown that the HPCVD films displayed the lowest resistivity and a $\lambda_c \sim 40$ nm among MgB₂ films deposited by different techniques[24]. The cleanness of our films may account for the lower λ_c values we have obtained than those reported in the literature. Also shown in Fig. 5.5 is the result for a 20 nm-thick HPCVD MgB₂ film as measured by the mutual inductance technique at 50 Hz[123]. The field is perpendicular to the film surface and thus the technique measures the penetration depth in the direction of the *ab*-

plane. The mean free path of this film is limited by the thickness (~ 20 nm), and the enhanced scattering makes the film near the dirty limit. It can be seen that this data fits well with the theoretical prediction for λ_{ab} in the dirty limit. A large value of $\lambda_{ab}(0) = 140$ nm was obtained from this measurement, which does not contradict our current measurement because the film in the mutual inductance measurement was in the dirty limit.

5.4 Conclusion

In summary, the c -axis penetration depth of clean MgB_2 films grown by HPCVD has been measured using single Josephson junctions and DC SQUIDs. Although different mechanisms were employed in the two approaches, $\lambda_c(0)$ values close to 40 nm were consistently obtained. The absolute values as well as the temperature dependence of λ_c agree with the theoretical prediction for clean MgB_2 films. The small penetration depth values in clean MgB_2 films are desirable for applications in superconducting digital circuits. For multilayers in superconducting RF cavity where a larger λ is desirable, introduction of scattering in the MgB_2 films is necessary to increase the penetration depth.

CHAPTER 6

SUPERCONDUCTING MAGNESIUM DIBORIDE TOGGLE FLIP FLOP CIRCUIT

6.1 Introduction

Rapid single flux quantum (RSFQ) circuits have emerged as a prominent superconducting integrated circuit technology[41]. The logic function of an RSFQ circuit relies on the superconducting flux quantum, allowing for high operating speed and low power consumption[111]. In an RSFQ toggle flip flop (TFF) circuit using Nb technology, operation up to 770 GHz has been demonstrated[42], which approaches the theoretical limit established by the superconducting gap parameter Δ of Nb and the junction critical current density J_c [41]. Attempts at HTS devices have been made[124-126], but the performance of most commonly used grain-boundary-type HTS Josephson junctions has been difficult to control mostly due to the short coherence length and d -wave symmetry[10]. Also, HTS and other Nb-based compounds (e.g. NbN) have large magnetic penetration depths[32, 127], making the design and fabrication of RSFQ circuits difficult[31].

MgB₂ has many properties which exceed the limitations of other superconductors for RSFQ circuits. Its high superconducting transition temperature T_c (39 K) allows for operating temperatures at about 20 K[128, 129]. The larger gap parameters ($\Delta_\pi = 2.1$ meV and $\Delta_\sigma = 7.1$ meV)[13] than Nb allow for a speed limit above 1 THz. Clean MgB₂ has a nearly isotropic magnetic penetration depth much smaller than HTS and Nb-based

compounds[120,130]. The coherence length of MgB₂ at low temperature ($\xi_c \sim \xi_{ab} \sim 5$ nm for clean samples) is much longer than that of HTS, making MgB₂ Josephson junctions easier to fabricate and control than HTS[130, 131]. Sandwich-type MgB₂/MgO/MgB₂ Josephson junctions have been reported with an $I_c R_n$ product above 3 meV and J_c as high as 275 kA/cm² at 4.2 K and non-zero up to near T_c [132]. The junction I - V curves are typically hysteretic at low temperatures, and the hysteresis disappears above 15 K, though some junctions, particularly with low J_c , do not exhibit any hysteresis. Design parameters for using these junctions in RSFQ circuits have been studied[133]. In this study, we have demonstrated the frequency division operation of a TFF circuit using MgB₂/MgO/MgB₂ Josephson junctions up to 63 GHz at 20 K and 180 GHz at 3.2 K. This is a significant step towards a superconducting integrated circuit technology using MgB₂.

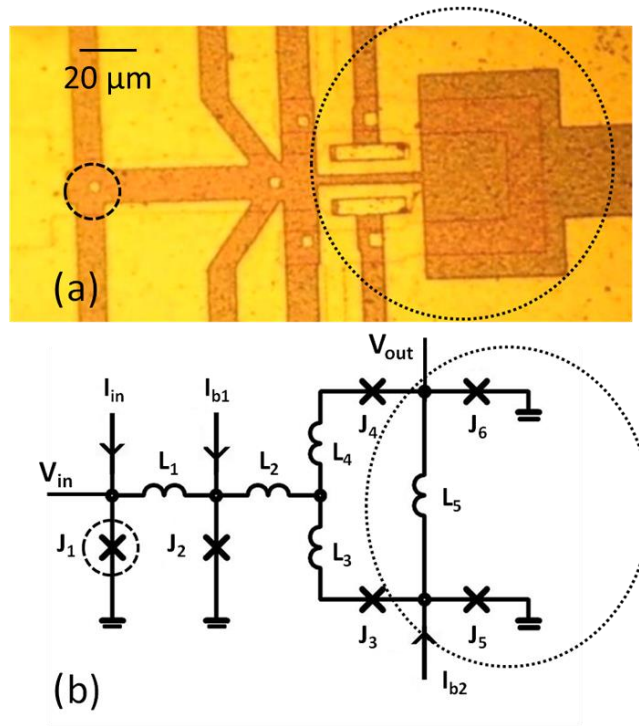


Figure 6.1. (top) Optical image and (bottom) schematic diagram of the TFF circuit. The junction J_1 is circled in both by a dashed circle and the interferometer loop is circled by a dotted circle.

6.2 Experiment

An optical image and a schematic diagram of the TFF circuit studied in this work are shown in Fig. 6.1. It consisted of six Josephson junctions ($J_1 - J_6$) and five microstrip inductors ($L_1 - L_5$). Junctions J_1 and J_2 and inductor L_1 form a voltage controlled oscillator (VCO), which generates pulses from a DC input, V_{in} , with a frequency $f = \Phi_0 V_{in}$, where Φ_0 is the flux quantum. Junctions J_3 and J_4 and inductors L_2 , L_3 , and L_4 make up a pulse splitter which sends pulses to both arms of the TFF loop. The loop is made up of

junctions J_5 and J_6 with inductor L_5 to create an interferometer which performs frequency division of the incoming pulses. A bias current I_{b2} generates flux in the interferometer loop such that the two junctions alternately switch from superconducting to normal state in response to each incoming pulse. An additional bias current, I_ϕ across L_5 from the I_{b2} node to the V_{out} node, may be used to ensure the correct flux through the interferometer loop. The output voltage, V_{out} , measured across either J_5 or J_6 which senses only half the number of the incoming pulses, should be half the input voltage. The circuit was designed to work at temperatures, normally around 20 K for our junctions, when the junctions were self-shunted with I_c high enough to overcome thermal noises. Simulations of the TFF circuit using parameters from our $MgB_2/MgO/MgB_2$ junctions indicated that the I_c values of J_5 and J_6 are the most critical parameters, and the allowable I_c spreads for them are $\pm 15\%$.

The fabrication process of the TFF circuit is described in Appendix A. There are three superconducting layers in the TFF circuit, two for the $MgB_2/MgO/MgB_2$ junctions and one for the wiring layer, with MgO as the barrier layer and insulating layer. Both of the MgB_2 electrode layers also function as ground planes for the inductors in the opposing layers. The MgB_2 layers were grown by hybrid physical chemical vapor deposition (HPCVD)[116] and the MgO layers by RF magnetron sputtering from a MgO ceramic target. The thickness of the two MgB_2 layers was 120 nm and 90 nm for the bottom and top electrodes, respectively, while the thickness of the MgO insulating layer was chosen to be about 70 nm. The barrier thickness was approximately 1.4 nm, as determined by the J_c of junctions on a sister sample. These thicknesses, along with the

penetration depth, which is about 40 nm at low temperature, are crucial in establishing the sheet inductance of the circuit inductors[133]. The junction sizes were $4 \mu\text{m} \times 4 \mu\text{m}$ for J_1 to J_4 and $5 \mu\text{m} \times 5 \mu\text{m}$ for J_5 and J_6 and the typical junction property (I_c and R_n) spreads 1σ were around 15 %, similar to the simulated allowable property spreads for the TFF circuit. Measurement of the circuit was carried out in a pulse tube cryocooler with magnetic shielding down to 3 K. The current biases were applied by batteries to reduce measurement noise.

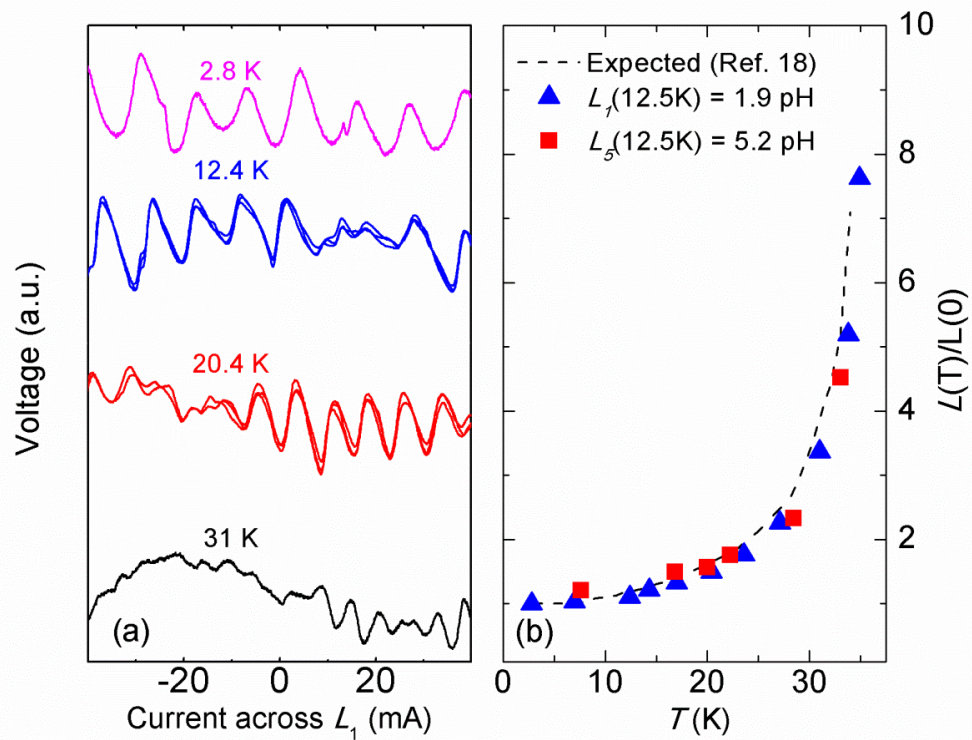


Figure 6.2. (left) Voltage modulation across J_1 and J_2 at different temperatures and constant current bias as a current is scanned across the inductor L_1 . (right) Temperature dependence of the inductance for L_1 and L_5 calculated from the period of voltage oscillations. Dotted line shows expected dependence.

6.3 Results

The voltage across the VCO formed by J_1 , J_2 , and L_1 , essentially a dc-SQUID, at constant current-bias as a function of the current through L_1 is shown in Fig. 6.2(a) for different temperatures. The period of the voltage oscillation (ΔI) corresponds to one flux quantum difference inside the SQUID loop, from which the inductance of L_1 can be obtained by $L_1 = \Phi_0/\Delta I$. At 12.5 K, L_1 thus obtained was 1.9 pH as compared to the design value of 2 pH. Similarly, by measuring the dc-SQUID formed by J_5 , L_5 , and J_6 , L_5 at 12.5 K was found to be 5.2 pH as compared to the design value of 5 pH. Figure 6.2(b) shows the temperature dependence of the inductances of L_1 and L_5 , which is in agreement with the prediction of a two-gap model for MgB_2 [131], suggesting that parasitic inductance in the circuit is negligible. It is difficult to measure the I_c of individual Josephson junction in the circuit. However, the SQUID measurements described above indicate that the Josephson junctions in the circuit functioned properly.

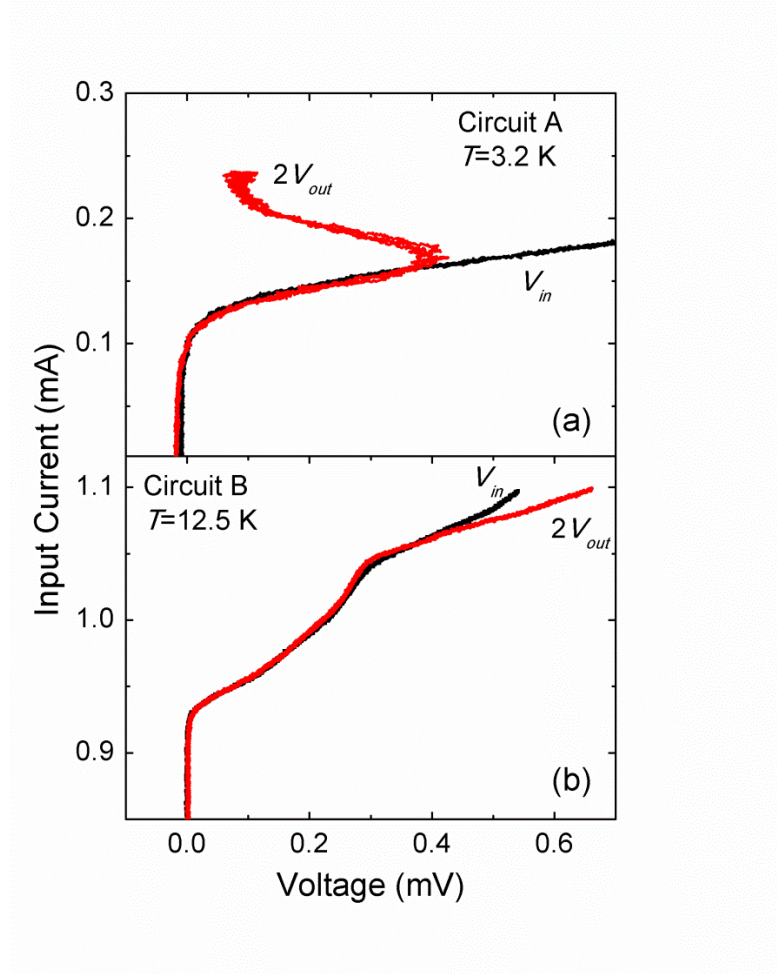


Figure 6.3. Input voltage V_{in} and twice the output voltage $2V_{out}$ versus input current I_{in} for (top) Circuit A at 3.2 K, and (bottom) Circuit B at 12.5 K.

The operation of the TFF circuit was tested by measuring V_{in} and V_{out} as the input current I_{in} was scanned, and the results for two circuits are shown in Fig. 6.3.

Temperature and bias currents I_{b1} and I_{b2} were adjusted in order to achieve the frequency division operation. The result for Circuit A [Fig. 6.3(a)] was measured at 3.2 K, with the

bias currents $I_{b1} = 0.35$ mA and $I_{b2} = 0.48$ mA. The low operating temperature indicates that the $\text{MgB}_2/\text{MgO}/\text{MgB}_2$ junctions in this circuit did not have hysteresis at this temperature. The figure shows that V_{in} and $2V_{\text{out}}$ overlap up to about 0.37 mV before they separate with each other, indicating that the TFF functioned up to a Josephson frequency of about 180 GHz. Circuit B was measured at 12.5 K, with the bias currents $I_{b1} = 4.82$ mA, $I_{b2} = 0.67$ mA, and $I_{\phi} = 0.25$ mA [Fig. 6.3(b)]. For this circuit, the range where V_{in} and $2V_{\text{out}}$ overlap is up to about 0.2 mV, indicating the operation of the TFF circuit up to a Josephson frequency of 100 GHz. Different temperature ranges and bias parameters were used for the two circuits to work properly because the Josephson junction properties and circuit element parameters were different in them. In the following, detailed characterization of Circuit B is presented.

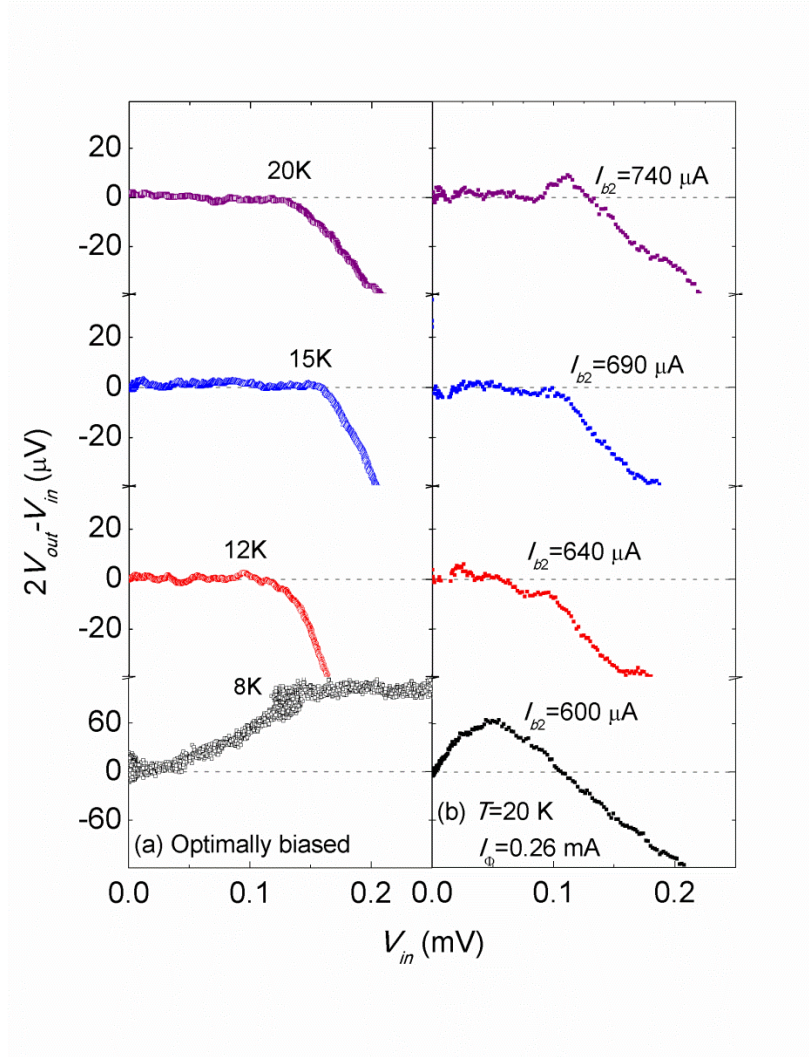


Figure 6.4. Difference $2V_{out} - V_{in}$ for Circuit B (left) at 8, 12, 15, and 20 K, all biased optimally; and (right) at 20 K and $I_{\phi} = 260\ \mu\text{A}$ for $I_{b2} = 600, 640, 690,$ and $740\ \mu\text{A}$.

To verify the toggle flip flop operation and determine the upper limit of operating frequency more precisely, we plot the difference $2V_{out} - V_{in}$ as a function of V_{in} under different conditions. Proper operation of the circuit leads to $2V_{out} - V_{in} = 0$, while the

deviation from zero signals the loss of frequency division function. Figure 6.4(a) shows the results for Circuit B at different temperatures, all biased optimally. Both the inductance of the microstrips and I_c of the junctions are functions of temperature, while their product is the most important factor for the TFF operation, which changes gradually with temperature. Circuit B showed a range of operation from 9 K to above 21 K. As seen in the figure, the difference $2V_{\text{out}} - V_{\text{in}}$ is within the measurement noise of 5-7 μV up to 0.13 mV (63 GHz) at 20 K, 0.15 mV (73 GHz) at 15 K, and 0.11 mV (53 GHz) at 12 K, beyond which it clearly deviates from zero. At higher than 21 K or lower than 9 K, $2V_{\text{out}} - V_{\text{in}} = 0$ could not be reached at any bias conditions indicating that the microstrip inductance and junction I_c were outside of the operation margin for the circuit. In Fig. 6.4(b), $2V_{\text{out}} - V_{\text{in}}$ versus V_{in} at 20 K and $I_{\phi} = 0.26$ mA is plotted for different I_{b2} values. For $I_{b2} = 640, 690,$ and 740 μA , $2V_{\text{out}} - V_{\text{in}} = 0$ was achieved up to about 0.1 mV. For $I_{b2} = 600$ μA , $2V_{\text{out}} - V_{\text{in}}$ could not reach zero at any V_{in} , indicating that the bias conditions were outside of the operation margin. Considering the variations in the inductor and junction properties, the experimental value and margin of I_{b2} are in reasonable agreement with the design parameters, which are 500 μA with approximately a $\pm 15\%$ margin.

Another way to confirm the TFF operation is to hold the input current, thus V_{in} , constant, so that the VCO generates pulses at a constant frequency, and scan I_{b2} (I_{b1} is also held constant.) When the I_{b2} value is within the range to allow for TFF operation, a constant $V_{\text{out}} = V_{\text{in}}/2$ should be observed. Unfortunately for the configuration of our circuit, changing I_{b2} also changes V_{in} . To separate the effects of I_{b2} and V_{in} , complete I - V scans were taken for different values of I_{b2} and the V_{out} having the same input current as

the desired V_{in} was used to construct the $V_{out} - I_{b2}$ curve. The result for Circuit B at 20 K is shown in Fig. 6.5 for different V_{in} from 20 μV to 120 μV . It should be noted that the method used to develop this plot has an error of about 1.5 μV . Nevertheless, the data shows regions of constant voltage for each curve with the exception of the top curve which shows no clearly constant region of $2V_{out} = V_{in}$. The circuit has a region of proper operation up to $V_{in} = 0.1 \text{ mV}$ with a I_{b2} bias margin of about 20 μA .

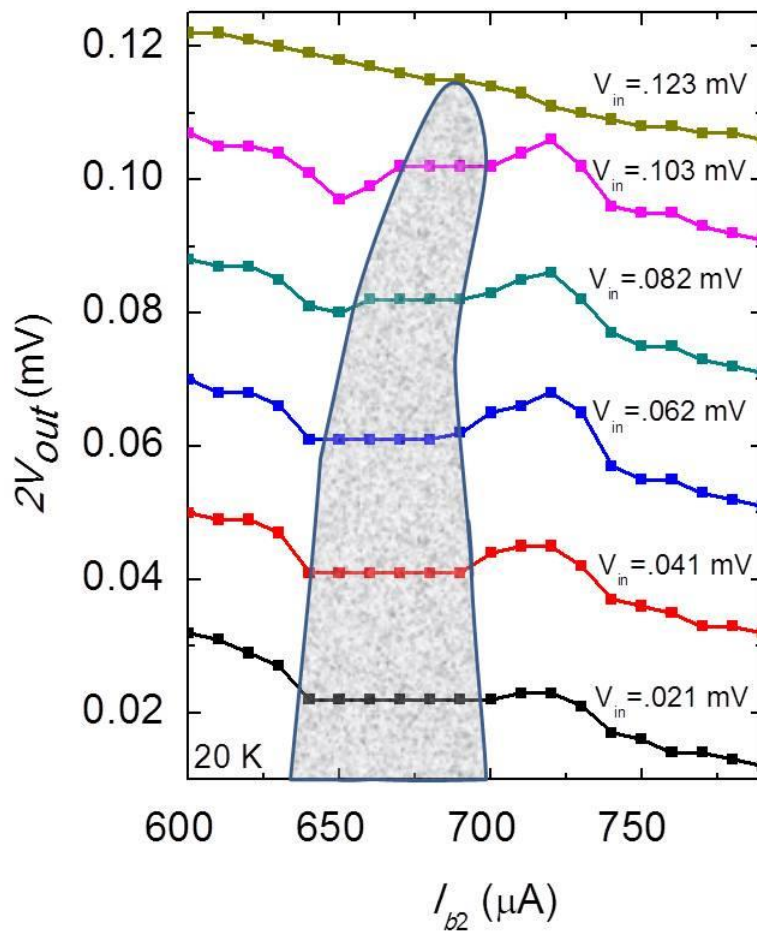


Figure 6.5. $2V_{out}$ versus I_{b2} for different operating frequencies ranging from about 10 GHz ($V_{in} = 0.021$ mV) to 50 GHz ($V_{in} = 0.103$ mV). Shaded area shows the region of operation.

6.4 Conclusion

In summary, a TFF circuit has been designed, fabricated, and tested using self-shunted $\text{MgB}_2/\text{MgO}/\text{MgB}_2$ Josephson junctions. The result shows operation of the circuit with frequencies of 180 GHz at 3.2 K in one circuit, and 63 GHz at 20 K in another circuit. It demonstrates the viability of a MgB_2 technology for superconducting integrated circuits. Further improvements include adding a ground plane and improving junction parameter control. The addition of another MgB_2 layer for a true superconducting ground plane without the gaps, which are currently unavoidable, will help control sheet inductances. To gain better control of junction parameters, alternative barrier materials such as AlN and smaller junction areas will be investigated.

CHAPTER 7

CONCLUSIONS AND FUTURE WORK

7.1 Conclusion

The MgB₂ thin films were grown using the HPCVD method on a newly developed system. As opposed to simply reproducing films to exact specifications of previous results, the system was put together so as to stabilize the growth conditions. This work is not trivial when referring to any CVD process as there are many factors which contribute to process instability. Films grown for this work were used primarily in device fabrication and thus the film surface roughness was optimized by utilizing a 5% addition of N₂ gas during the growth process. This yielded films grown in SiC substrate with a surface roughness of ~1 nm while maintaining a high T_c above 41 K and a RRR near 9 for a 120 nm film.

MgB₂ Josephson junctions were fabricated using Pb, Nb, and MgB₂ as the counter electrode. These junctions were used to study the innate superconducting properties of MgB₂. The MgB₂/MgO/MgB₂ junctions were improved with three major alterations in the fabrication process. The film thickness was minimized so as to minimize the etching time for patterning. This was done in an attempt to improve the on-chip feature non-uniformity due to lithography limitations. The growth process of the secondary and tertiary MgB₂ films was shortened by about 55%. This minimized the exposure of the

barrier layer and lower layers to the high temperature, hydrogen atmosphere which may be detrimental to any oxygenated barrier. The most significant change in the process was to change the deposition of the MgO barrier from RF sputtering of an MgO target to reactive sputtering of an Mg target in an oxygen environment. The changes made to the process yielded more consistent junctions with higher $I_c R_n$ products. Though not reported, the success rate of the previous process was below 90% while the new process has a near perfect success rate, though parameter spreads are still large.

The MgB₂/MgO/MgB₂ junctions were used to make a washer-type DC SQUID which clearly presents a large potential for MgB₂ in application. The preliminary results presented in this work were limited by the non-ideal design for high temperature operation, but still prove without question that the junction technology will suffice for this popular superconducting application. The SQUID had a large voltage modulation of 100 μ V and the effective area calculated with the period of modulation implies a focusing factor of about 5.

The junctions were also used to fabricate 100 junction series arrays. The array IV curves proved useful to qualitatively measure the parameter spread of the junctions. Although the process is premature for array applications, this work is a step in the right direction, showing that the junction success rate is near 100%. The development of these arrays is another important factor for the future of MgB₂ Josephson junctions.

Although the popularity of MgB₂ is in decline in the physics world, there is still plenty of research of a scientific nature surrounding MgB₂. The use of MgB₂ in

applications requires more intricate knowledge of the superconducting parameters than is currently available. In some cases it would be useful to alter these properties. There is a desire to increase the lower critical field for superconducting RF cavities. The penetration depth needs to be characterized precisely for many different applications, most importantly in Josephson devices. The penetration depth has not been reported previously with any continuity or theoretical sustenance. The work done using junctions and DC SQUIDS in Chapter 5 compares experimental findings of the penetration depth to a theoretical model in two opposite and limiting cases, namely, clean film with the magnetic field parallel to the film surface and dirty film with the field perpendicular to the surface. Both of these cases fit nicely to this theory, which states that the penetration depth of MgB_2 is nearly isotropic in the clean limit. This is a highly desired aspect of a material for Josephson devices.

The culmination of this work is the RSFQ TFF circuit presented in Chapter 6. The circuit is a combination of 6 junctions of different design parameters and 5 microstrip inductors working together to achieve a frequency division of input pulses. This particular circuit was chosen because it is used to determine a potential upper limit for frequency of logic operations. Although the work presented does not exceed the speed limit of similar low temperature devices, it was shown to work at 20 K. The ever increasing helium deficiency will make higher temperature operation a priority over speed limit. The ultimate speed limit is limited by the superconducting gap parameter, which is higher in MgB_2 than low temperature superconductors so the potential of MgB_2 at low temperature exceeds 1 THz while Nb devices are limited to less than 800 GHz. It

is shown here that the 20 K operation is likely to work to at least 30% of the low temperature operation. It is hoped that this promising result inspires new research into MgB₂ Josephson devices and circuits.

7.2 Future Work

In order to continue the progress being made on MgB₂ devices, there is an ever-pressing need to improve on the junction parameters. Although they have not yet reached the theoretical limits set by material parameters, the most important aspect is to improve spreads. It is assumed that a pure tunneling barrier will make this work much easier, but the high temperature H₂ atmosphere needed for HPCVD growth is not conducive to a uniform barrier layer. Therefore new ideas must be attempted to solve this issue. While it will be difficult, the energy of the deposited material is not as high as PLD depositions, so there is still hope for progress where YBCO has seen none. One likely future idea to achieve this is a nitride barrier, presumably AlN which has been used to make MgB₂ junctions previously and may not be susceptible to the H₂ environment. Another good idea is avoid using a material consisting of any metal with a melting point below the deposition temperature. If any excess metal exists in the barrier, even at the nanoscale level, it could evaporate out of the surface and generate holes in the barrier. An obvious idea to improve the barrier is to lower the deposition temperature. This is not trivial because, even though lower temperature depositions have been presented previously, Mg will condense on the film surface and generate defects in the films.

Eventually, research should be undertaken to utilize both gaps of MgB_2 . The 7.2 meV σ - gap parameter could reach RSFQ operating speeds up near 3 THz. The two dimensional nature of this gap make it extremely difficult to control with current technology, but the ever improving ability to deposit thin films at an atomic level will prove useful in surmounting obstacles like this.

The applications of Josephson arrays and DC SQUIDs require much more controllable junction properties. This is another reason for pressing forward and improving the junction technology. Utilizing the arrays as a tool for measuring improvement will help speed up this process. Changing the design parameters of these two devices will be important to show just how well they compare to current technologies. For example, separating the junctions in an array with inductors, the value of which has a designed resonant frequency, can utilize the AC Josephson relation to generate THz radiation to be used for heterodyne detection devices. This would be a simple modification to the existing design process which may produce a lot of interesting research. This resonance is closely related to the penetration depth so the ability to tune the penetration depth with temperature or film cleanliness may be used to create a tunable THz wave generator.

The DC SQUIDs are probably the easiest Josephson device to make and prepare for application. As a result, future work on these including noise measurements and design optimization should be a high priority. The goal in mind should be high temperature operation while maintaining low noise levels and high sensitivity, all of which should be reasonably easy to achieve given prior research results.

To make MgB_2 more suitable for RSFQ circuits, additional layers, including MgB_2 , normal metals, and insulators need to be added to the process. This would make the design of new and more complicated circuits much easier. The complications associated with HTS are more problematic than those for MgB_2 and as a result, MgB_2 circuits should be able to move forward at a much more rapid pace. Again, improving junction parameter spreads goes a long way in this regard. The penetration depth measurements done in this work can now be used to simulate inductance values of complex striplines for more complicated circuits. A simple next step would be to create a DC to SFQ converter and an SFQ to DC converter separated by some Josephson transmission lines. The ability to generate and display the SFQ pulses through the SIC would help to generate more interest in the field.

Overall, the MgB_2 Josephson junction community has dwindled down to one group with the capabilities needed to fabricate and measure these junctions. The overall goal of this research was to make progress and present results which might inspire more research in this field. The full potential of MgB_2 will never be reached if more research is not done. This should be kept in mind with all the future work done. Working on DC SQUIDS is a quick way to do this and should take some priority over more complicated research. Until a property spread less than 3% can be reached, there should be continuous research to achieve lower spreads. The technologies which utilize Josephson junctions have been well established using low temperature superconductors, so in theory, applying them to MgB_2 will be a simple task if the junction technology becomes mature enough.

REFERENCES CITED

- [1] H. K. Onnes, Commun. Phys. Lab. **12**, 120 (1911).
- [2] W. Meissner and R. Oschenfeld, Naturwiss. **21**, 787 (1933).
- [3] M. Tinkham “Introduction to Superconductivity”, 1996, 2nd Ed., New York, McGraw-Hill.
- [4] F. and H. London, Proc. Roy. Soc. **A149**, 71 (1935)
- [5] V.L. Ginzburg and L.D. Landau, Zh. Eksp. Teor. Fiz. **20**, 1064 (1950).
- [6] A. B. Pippard, Proc. Roy. Soc. **A216**, 547 (1953).
- [7] J. Bardeen, L. N. Cooper, and J. R. Schrieffer, Phys. Rev. **108**, 1175 (1957).
- [8] A. A. Abrikosov, Sov. Phys. JETP **5**, 1174 (1957).
- [9] G. Bednorz and K. A. Müller, Z. Phys. **B64**, 189 (1986).
- [10] C. C. Tsuei and J. R. Kirtley, Rev. Mod. Phys. **72**, 969 (2000).
- [11] J. Nagamatsu, N. Nakagawa, T. Muranaka, Y. Zenitani, and J. Akimitsu, Nat. **410**, 63 (2001).
- [12] W. Pickett, Nat. (London) **418**, 733 (2002).
- [13] H. J. Choi, D. Roundy, H. Sun, M. L. Cohen, and S. G. Louie, Nat. (London), **418**, 758 (2002).
- [14] G. R. Stewart, Rev. Mod. Phys. **83**, 1589 (2011).
- [15] M. Iavarone, G. Karapetrov, A. E. Koshelev, W. K. Kwok, G. W. Crabtree, D. G. Hinks, W. N. Kang, E. M. Choi, H. J. Kim, H. J. Kim, and S. I. Lee, Phys. Rev. Lett. **89** 187002 (2002).
- [16] F. Bouquet, R. A. Fisher, N. E. Philips, D. G. Hinks and J. D. Jorgensen, Phys. Rev. Lett. **87** 047001, (2001).
- [17] J. W. Quilty, S. Le, A. Yamamoto, and S. Tajima, Phys. Rev. Lett. **88** 087001, (2002).
- [18] T. Takahashi, T. Sato, S. Souma, T. Muranaka, and J. Akimitsu, Phys. Rev. Lett. **86** 4915, (2001).

- [19] G. Karapetrov, M. Iavarone, W. K. Kwok, G.W. Crabtree, and D. G. Hinks, Phys. Rev. Lett. **86** 4374, (2001).
- [20] R. Osborn, E. A. Goremychkin, A. I. Kolesnikov, and D. G. Hinks, Phys. Rev. Lett. **87**, 017005, (2001).
- [21] M. R. Eskildsen, M. Kugler, S. Tanaka, J. Jun, S. M. Kazakov, J. Karpinski, and Ø. Fischer, Phys. Rev. Lett. **89**, 187003 (2002).
- [22] K. Chen, W. Q. Dai, C. G. Zhuang, Q. Li, S. Carabello, J. G. Lambert, J. T. Mlack, R. C. Ramos, and X. X. Xi, Nat. Commun. **3**, 619 (2012).
- [23] M. R. Eskildsen, N. Jenkins, G. Levy, M. Kugler, Ø. Fischer, J. Jun, S. M. Kazakov, J. Karpinski, Phys. Rev. B **68**, 100508 (2003).
- [24] B. B. Jin, T. Dahm, C. Iniotakis, A. I. Gubin, E. M. Choi, H. J. Kim, S. I. Lee, W. N. Kang, S. F. Wang, Y. L. Zhou, A. V. Pogrebnyakov, J. M. Redwing, X. X. Xi, and N. Klein, Supercond. Sci. Technol. **18**, L1 (2005).
- [25] B.D. Josephson, "Possible new effects in superconductive tunneling," Phys. Lett. **1**, 251 (1962).
- [26] P. W. Anderson and J. M. Rowell, Phys. Rev. Lett **10**, 230 (1963).
- [27] R. Doll and M. Näbauer, Phys. Rev. Lett **7**, 51 (1961).
- [28] W. L. McMillan, Phys. Rev. **175**, 537 (1968).
- [29] K. K. Likharev, Rev. Mod. Phys. **51**, 101 (1979).
- [30] A. F. Andreev, Sov. Phys. JETP **46**, 1823 (1964).
- [31] T. Van Duzer and C. W. Turner, "Principles of Superconductive Devices and Circuits," 2nd Ed., Prentice Hall, New York (1999).
- [32] A. G. Sun, D. A. Gajewski, M. B. Maple, and R. C. Dynes, Phys. Rev. Lett. **72**, 2267 (1994).
- [33] Y. Kobayashi and M. Katoh, IEEE Microwave Theory Tech. Soc. **33**, 586 (1985).
- [34] E. Nazaretski, J. P. Thibodaux, I. Vekhter, L. Civale, J. D. Thompson, R. Movshovich, Appl. Phys. Lett. **95**, 262502 (2009).

- [35] A. Barone and G. Paterno, "Physics and Applications of the Josephson Effect." New York, John Wiley & Sons (1982).
- [36] D. E. McCumber, J. Appl. Phys. **39**, 2503 (1968a).
- [37] D. E. McCumber, J. Appl. Phys. **39**, 3113 (1968b).
- [38] W. C. Stewart, Appl. Phys. Lett. **12**, 277 (1968).
- [39] D. Yohannes, A. Kirichenko, S. Sarwana, and S. K. Tolpygo, IEEE Trans. Appl. Supercond. **17**, 181 (2007).
- [40] C. Kittel, "Introduction to Solid State Physics," 7th Ed., New York, John Wiley & Sons, Inc. (1996).
- [41] K.K. Likharev and V.K. Semenov, IEEE. Trans. Appl. Superconduct. **1**, 3 (1991).
- [42] W. Chen, V. Patel, A. Rylyakov, and K. Likharev. IEEE Trans. Appl. Supercond. **9**, 3212 (1999).
- [43] M. Johnson, B. Dalrymple, D. Durand, J. Luine, IEEE Trans. Appl. Supercond. **13**, 571 (2003).
- [44] X. D. Wu, B. Dutta, M. S. Hegde, A. Inam, T. Venkatesan, E. W. Chase, C. C. Chang, and R. Howard, Appl. Phys. Lett. **54**, 179 (1989).
- [45] P. Chaudhari, R. H. Koch, R. B. Laibowitz, t. R. McGuire, R. J. Gambino, Phys. Rev. Lett. **58**, 2684 (1987).
- [46] X. X. Xi, G. Linker, O. Meyer, E. Nold, B. Obst, F. Ratzel, R. Smithey, B. Strehlau, F. Weschenfelder, and J. Geerk, Z. Phys. B **74**, 13 (1989).
- [47] W. N. Kang, H. J. Kim, E. M. Choi, C. U. Jung, S. L. Lee, Sci. **292** 1521 (2001).
- [48] A. Berenov, Z. Lockman, X. Qi, J. L. MacManus-Driscoll, Y. Bugoslavsky, L. F. Cohen, M.-H. Jo, N. A. Stelmashenko, V. N. Tsaneva, M. Kambara, N. H. Babu, D. A. Cardwell, M. G. Blamire, Appl. Phys. Lett. **79**, 4001 (2001).
- [49] S. H. Moon, J. H. Yun, H. N. Lee, J. I. Kye, H. G. Kim, W. Chung, Appl. Phys. Lett. **79**, 2429 (2001).
- [50] X. H. Zeng, A. Sukiasyan, X. X. Xi, Y. F. Hu, E. Wertz, Q. Li, W. Tian, H. P. Sun, X. Q. Pan, J. Lettieri, D. G. Schlom, C. O. Brubaker, Z.-K. Liu, Q. Li, Appl. Phys. Lett. **79**, 1840 (2001).

- [51] R. Vaglio, M. G. Maglione, R. Di Capua, *Supercond. Sci. Technol.* **15**, 1236 (2002).
- [52] S. N. Ermolov, M. V. Indenbom, A. N. Rossolenko, I. K. Bdikin, L. S. Uspenskaya, N. S. Stepanov, V. G. Glebovskii, *JETP Lett.* **73**, 557 (2001).
- [53] A. Saito, A. Kawakami, H. Shimakage, Z. Wang, *Jpn. J. Appl. Phys.* **41**, L127 (2002).
- [54] R. Schneider, J. Geerk, F. Ratzel, G. Linker, A. Zaitsev, *Appl. Phys. Lett.* **85** 5290 (2004).
- [55] J. Kim, R. K. Singh, J. M. Rowell, N. Newman, L. Gu, and D. J. Smith, *J. Cryst. Growth* **270**, 107 (2004).
- [56] J. Kim, R. K. Singh, N. Newman, and J. M. Rowell, *IEEE Trans. Appl. Supercond.* **13**, 3238 (2003).
- [57] K. Ueda, M. Naito, *Appl. Phys. Lett.* **79**, 2046 (2001).
- [58] W. Jo, J.-U. Huh, T. Ohnishi, A. F. Marshall, M. R. Beasley, R. H. Hammond, *Appl. Phys. Lett.* **80**, 3563 (2002).
- [59] A. J. M. van Erven, T. H. Kim, M. Muenzenberg, J. S. Moodera, *Appl. Phys. Lett.* **81**, 4982 (2002).
- [60] C. B. Eom, M. K. Lee, J. H. Choi, L. Belenky, X. Song, L. D. Cooley, M. T. Naus, S. Patnaik, J. Jiang, M. O. Rikel, A. A. Polyanskii, A. Gurevich, X. Y. Cai, S. D. Bu, S. E. Babcock, E. E. Hellstrom, D. C. Larbalestier, N. Rogado, K. A. Regan, M. A. Hayward, T. He, J. S. Slusky, K. Inumaru, M. Haas, R. J. Cava, *Nat. (London)* **411**, 558 (2001).
- [61] C. Ferdeghini, V. Ferrando, G. Grassano, W. Ramadan, E. Bellingeri, V. Braccini, D. Marré, P. Manfrinetti, A. Palenzona, F. Borgatti, R. Felici, T.-L. Lee, *Supercond. Sci. Technol.* **14**, 952 (2001).
- [62] D. H. A. Blank, H. Hilgenkamp, A. Brinkman, D. Mijatovic, G. Rijnders, H. Rogalla, *Appl. Phys. Lett.* **79**, 394 (2001).
- [63] S. R. Shinde, S. B. Ogale, R. L. Greene, T. Venkatesan, P. C. Canfield, S. Budoko, G. Lapertot, C. Petrovic, *Appl. Phys. Lett.* **79**, 227 (2001).
- [64] H. Christen, H. Zhai, C. Cantoni, M. Paranthaman, B. Sales, C. Rouleau, D. Norton, D. Christen, D. Lowndes, *Physica C* **353**, 157 (2001).

- [65] A. Plecenik, L. Satrapinsky, P. Kus, S. Gazi, S. Benacka, I. Vavra, I. Kostic, *Physica C* **363**, 230 (2001).
- [66] J. Kim, R. K. Singh, N. Newman, J. M. Rowell, *IEEE Trans. Appl. Supercond.* **13**, 3238 (2003).
- [67] Z. K. Liu, D. G. Schlom, Q. Li, X. X. Xi, *Appl. Phys. Lett.* **78**, 3678 (2001).
- [68] X. H. Zeng, A. V. Pogrebnyakov, A. Kotcharov, J. E. Jones, X. X. Xi, E. M. Lysczek, J. M. Redwing, S. Y. Xu, Q. Li, J. Lettieri, D. G. Schlom, W. Tian, X. Q. Pan, Z. K. Liu, *Nat. Mat.* **1**, 35 (2002).
- [69] Y. Cui, Ke Chen, Qi Li, X. X. Xi, and J. M. Rowell, *Appl. Phys. Lett.* **89**, 202513 (2006).
- [70] G. Carapella, N. Martucciello, G. Costabile, C. Ferdeghini, V. Ferrando, and G. Grassano, *Appl. Phys. Lett.* **80**, 2949 (2002).
- [71] A. Saito, A. Kawakami, H. Shimakage, H. Terai, and Z. Wang, *J. Appl. Phys.* **92**, 7369 (2002).
- [72] T. H. Kim and J. S. Moodera, *Appl. Phys. Lett.* **85**, 434 (2004).
- [73] J. Geerk, R. Schneider, G. Linker, A. G. Zaitsev, R. Heid, K.-P. Bohnen, H. V. Lohneysen, *Phys. Rev. Lett.* **94**, 227005 (2005).
- [74] Y. Cui, Ke Chen, Qi Li, X. X. Xi, and J. M. Rowell, *IEEE Trans. Appl. Supercond.* **17**, 218 (2007).
- [75] H. Shimakage, K. Tsujimoto, Z. Wang, M. Tonouchi, *Appl. Phys. Lett.* **86**, 072512 (2005).
- [76] Ueda K, Saito S, Sernba K, and T. Makimoto, *Appl. Phys. Lett.* **86**, 172502 (2005).
- [77] R. K. Singh, R. Gandikota, J. Kim, N. Newman, and J. M. Rowell, *Appl. Phys. Lett.* **89**, 042512 (2006).
- [78] K. Chen, C. G. Zhuang, Q. Li, Y. Zhu, P. M. Voyles, X. Weng, J. M. Redwing, R. K. Singh, A. W. Kleinsasser, and X. X. Xi, *Appl. Phys. Lett.* **96**, 042506 (2010).
- [79] K. Chen, C. G. Zhuang, Q. Li, X. Weng, J. M. Redwing, Y. Zhu, P. M. Voyles, X. X. Xi, *IEEE Trans. Appl. Supercond.* **21**, 115 (2011)

- [80] K. Chen, Y. Cui, Q. Li, and X. X. Xi, *IEEE Trans. Appl. Supercond.* **17**, 955 (2007).
- [81] M. V. Costache and J. S. Moodera, *Appl. Phys. Lett.* **96**, 082508 (2010).
- [82] T. H. Kim, *J. Kor. Phys. Soc.* **49** (5), L1881 (2006).
- [83] J. I. Kye, H. N. Lee, J. D. Park, S. H. Moon, and B. Oh, *IEEE Trans. Appl. Supercond.* **13**, 1075 (2003).
- [84] A. Saito, A. Kawakami, H. Shimakage, H. Terai, and Z. Wang, *IEEE Trans. Appl. Supercond.* **13**, 1067 (2003).
- [85] Y. Shen, R. K. Singh, S. Sanghavi, Y. Wei, R. V. Chamberlin, B. H. Moeckly, J. M. Rowell, and N. Newman, *Supercond. Sci. Technol.* **23**, 075003 (2010).
- [86] H. Shimakage and Z. Wang, *Supercond. Sci. Technol.* **19**, S182 (2006).
- [87] H. Shimakage and Z. Wang, *Physica C* **435**, 66 (2006).
- [88] H. Shimakage and Z. Wang, *IEEE Trans. Appl. Superconduct.* **17**, 202 (2007).
- [89] H. Shimakage and Z. Wang, *IEEE Trans. Appl. Superconduct.* **19**, 265 (2009).
- [90] B. Soodchomshom, R. Hoonsawat, and I. M. Tang, *Physica C* **455**, 33 (2007).
- [91] B. Soodchomshom, I. M. Tang, and R. Hoonsawat, *Physica C* **468**, 47 (2008).
- [92] B. Soodchomshom, I. M. Tang, and R. Hoonsawat, *Solid State Comm.* **149**, 1012 (2009).
- [93] K. Ueda and M. Naito, *IEICE Trans. Electron.* **E88C**, 226 (2005).
- [94] K. Ueda, S. Saito, K. Semba, T. Makimoto, and M. Naito, *J. J. Appl. Phys.* **46**, L271 (2007).
- [95] K. Ueda, S. Saito, K. Semba, T. Makimoto, and M. Naito, *Appl. Phys. Lett.* **86**, 172502 (2005).
- [96] K. Chen, D. Cunnane, Y. Shen, X. X. Xi, A. W. Kleinsasser, and J. M. Rowell, *Appl. Phys. Lett.* **100**, 122601 (2012).
- [97] S. Shapiro, *Phys. Rev. Lett.* **11**, 80 (1963).

- [98] G. L. Kerber, A. W. Kleinsasser, B. Bumble, IEEE Trans. Appl. Supercond. **19**, 159 (2009).
- [99] D. Olaya, P. D. Dresselhaus, S. P. Benz, A. Herr, Q. P. Herr, A. G. Ioannidis, D. L. Miller, A. W. Kleinsasser, Appl. Phys. Lett. **96**, 213510 (2010).
- [100] R. C. Jaklevic, J. Lambe, A. H. Silver, and J. E. Mercereau Phys. Rev. Lett. **12**, 159 (1964).
- [101] S. K. H. Lam, R. Cantor, J. Lazar, K. E. Leslie, J. Du, S. T. Keenan, and C. P. Foley, J. Appl. Phys. **113**, 123905 (2013).
- [102] R. Gross, L. Alff, A. Beck, O. M. Froehlich, D. Koelle, and A. Marx, IEEE Trans. Appl. Supercond. **7**, 2929 (1997).
- [103] S. H. Hong, S. G. Lee, W. K. Seong, W. N. Kang, Physica C **470**, S1036 (2010).
- [104] A. Brinkman, D. Veldhuis, D. Mijatovic, G. Rijnders, D. H. A. Blank, H. Hilgenkamp, and H. Rogalla, Appl. Phys. Lett. **79**, 2420 (2001).
- [105] D. Mijatovic, A. Brinkman, D. Veldhuis, H. Hilgenkamp, H. Rogalla, G. Rijnders, D. H. A. Blank, A. V. Pogrebnyakov, J. M. Redwing, S. Y. Xu, Q. Li, and X. X. Xi, Appl. Phys. Lett. **87**, 192505 (2005).
- [106] Y. Zhang, D. Kinion, J. Chen, John Clarke, D. G. Hinks, and G. W. Crabtree, Appl. Phys. Lett. **79**, 3995 (2001).
- [107] J. M. Jaycox and M. B. Ketchen, IEEE Trans. Mag. **17**, 1 (1981).
- [108] C. J. Burroughs, S. P. Benz, IEEE Trans. Appl. Supercond. **9**, 4145 (1999)
- [109] P. Barbara, A. B. Cawthorne, S. V. Shitov, and C. J. Lobb, Phys. Rev. Lett. **82**, 1963 (1999).
- [110] D. Gupta, T.V. Filippov, A.F Kirichenko, D.E Kirichenko, I.V. Vernik, A. Sahu, S. Sarwana, P. Shevchenko, A. Talalaevskii, O.A.Mukhanov, IEEE Trans. Appl. Supercond. **17**, 430 (2007).
- [111] H. J. M. ter Brake and G. F. M. Wiegerinck, Cryo. **42**, 705 (2002).
- [112] H. Katsuno, S. Inoue, T. Nagano, and J. Yoshida, IEEE Trans. Appl. Supercond. **13**, 809 (2003).
- [113] Y. Tarutani, Y. Ishimaru, H. Wakana, S. Adachi, K. Nakayama, Y. Oshikubo, O. Horibe, Y. Morimoto, K. Tanabe, IEEE Trans. Appl. Supercond. **15** 376 (2005).

- [114] D. K. Chin and T. Vanduzer, *Appl. Phys. Lett.* **58**, 753 (1991).
- [115] W. H. Henkels, *Appl. Phys. Lett.* **32**, 829 (1978).
- [116] X. X. Xi, *Supercond. Sci. Technol.* **22**, 15 (2009).
- [117] A. W. Kleinsasser, *IEEE Trans. Appl. Supercond.* **11**, 1043 (2001).
- [118] B. B. Jin, T. Dahm, A. I. Gubin, E. M. Choi, H. J. Kim, S. I. Lee, W. N. Kang, and N. Klein, *Phys. Rev. Lett.* **91**, 127006 (2003).
- [119] A. Gurevich, *Appl. Phys. Lett.* **88**, 012511 (2006).
- [120] A. A. Golubov, A. Brinkman, O. V. Dolgov, J. Kortus, and O. Jepsen, *Phys. Rev. B* **66**, 054524 (2002).
- [121] J. Kim, N. Haberkorn, S. Z. Lin, L. Civale, E. Nazaretski, B. H. Moeckly, C. S. Yung, J. D. Thompson, and R. Movshovich, *Phys. Rev. B* **86**, 024501 (2012).
- [122] J. Bardeen and J. R. Schrieffer, in *Progress in Low Temperature Physics*, edited by C. J. Gorter (Elsevier, 1961), Vol. **3**, pp. 170.
- [123] M. S. Kim, J. A. Skinta, T. R. Lemberger, W. N. Kang, H. J. Kim, E. M. Choi, and S. I. Lee, *Phys. Rev. B* **66**, 064511 (2002).
- [124] K. Saitoh, Y. Soutome, T. Fukazawa, Y. Tarutani, and K. Takagi, *IEEE Trans. Appl. Supercond.* **11**, 791 (2001).
- [125] K. Tsubone, H. Wakana, Y. Ishimaru, S. Adachi, K. Nakayama, Y. Tarutani, and K. Tanabe, *IEEE Trans. Appl. Supercond.* **15**, 3911 (2005).
- [126] A. G. Sun, D. J. Durand, J. M. Murduck, S. V. Rylov, M. G. Forrester, B. D. Hunt, and J. Talvacchio, *IEEE Trans. Appl. Supercond.* **9**, 3825 (1999).
- [127] J. C. Villegier, N. Hadacek, S. Monso, B. Delaet, A. Roussy, P. Febvre, G. Lamura, and J. Y. Laval, *IEEE Trans. Appl. Supercond.* **11**, 68 (2001).
- [128] X. X. Xi, *Rep. Prog. Phys.* **71**, 116501 (2008).
- [129] T. Ortlev, H. Toepfer, and H. F. Uhlmann, *Supercond. Sci. Technol.* **14**, L37 (2001).

[130] D. Cunnane, C. G. Zhuang, K. Chen, X. X. Xi, J. Yong, and T.R. Lemberger, *Appl. Phys. Lett.* **102**, 072603 (2012).

[131] M. R. Eskildsen, M. Kugler, G. Levy, S. Tanaka, J. Jun, S. M. Kazakov, J. Karpinski, and O. Fischer, *Physica C* **385**, 169 (2003).

[132] T. K. Worthington, W. J. Gallagher, and T. R. Dinger, *Phys. Rev. Lett.* **59**, 1160 (1987).

[133] D. Cunnane, T. Tan, K. Chen, and X. X. Xi, *IEEE Trans. Appl. Supercond.* **23**, 1700204 (2013).

APPENDIX A

TRILAYER PROCESS

The following is a list form of the steps needed to make a Josephson Junction sample using the facilities at Temple University.

- 1) Deposit the bottom MgB_2 electrode.
 - a. Clean 7 mm by 7 mm SiC substrate using a cotton-tipped applicator in Isopropyl Alcohol (IPA). Leave substrate in sonicator in IPA until susceptor is ready for installation into the chamber.
 - b. Prepare Mg by scratching the oxide off the rod and cutting into approximately 0.25" pellets. Space them evenly around the susceptor.
 - c. Blow the substrate dry with the N_2 gun and place as close to the center of the susceptor as possible. As many as three substrates may be used successfully in one deposition.
 - d. Prepare the chamber by using the explosion-proof vacuum to remove any Mg dust and install the quartz liner tube. Install the susceptor into the heater element. Close up the chamber and pump. A background pressure less than $1\text{E-}2$ Torr is desired before purging.

- e. Purge the system for 10' in 400 sccm of H₂. Make sure that the diluting N₂ is used to ensure that the exhaust is below the flammability level.
- f. Pump the chamber until a background pressure of at least 2E-3 Torr is reached. Purge the diborane and N₂ line to ensure there is not excess gas in the lines. Turn the H₂ back on and set the pressure to 40 Torr.
- g. Heat the system and deposit the film. The heating output steps used are 16% for 4', 20% for 2' and 24.5% until deposition temperature is reached. Make sure to record the temperature of the Mg melting. 10 °C prior to deposition, turn on the N₂ to 20 sccm. Deposition temperature should be near 765 °C, although optimal temperature does vary a few degrees. Turn on diborane at deposition temperature and deposit for 2'. Turn off the diborane and wait 10' to turn off the heater.
- h. Let the sample cool. When it is near room temperature, turn off any gases flowing and pump the chamber. Vent and remove sample.
- i. For a Nb counter electrode skip to step 4.

2) Deposit MgO barrier.

- a. Attach sample using double sided copper tape. Using your bare fingertip to "dirty" the glue, decreasing the amount of glue that sticks to your sample.
- b. Install the sample holder into the chamber and pump chamber to low 10⁻⁶ Torr range. Ar flow rate should be 26 sccm and the O₂ flow rate should

be about 9 sccm. Deposition pressure should be 3.4×10^{-3} Torr. Set DC power supply to 25W and make sure to turn on the rotating motor (speed is not important). Make sure to pre-sputter for at least 5 minutes. 3-5 minutes should result in a barrier around 1-2 nm.

- c. Turn off power supply, shut down gas flow. Vent chamber and remove sample.

- 3) Deposit top layer of MgB_2 . Make sure that you clean any glue off the bottom of the sample. Do this by scratching off any glue under the microscope. Sample holders are concave so the sample can be placed face down without consequence.

- a. This deposition differs from the top because there is no cleaning of the sample after the barrier deposition. Deposition time should be just 30 “.

- 4) Deposit a Au passivation layer.

- a. Using the KJL sputtering system in the clean room, deposit first a thin layer of Cr for about 30 seconds at 25 watts, then a thicker layer of Ag using about 100 watts for 45”.

- b. For a Nb counter electrode, this deposition should be preceded with a 2’ deposition of Nb using 200 watts power. The depositions can be done sequentially in the same chamber.

- 5) First photolithography step. Recipe as follows:

- a. Spin AZ 3312 positive photoresist onto sample at 4000 RPM for 60". Soft bake for 90" at 90 °C.
- b. Exposure through mask for 5-7 seconds.
- c. Develop in 300 MIF developer:DI water solution (3:1) for about 45".
- d. Hard bake for 2' at 120 °C.
- e. The masks for the first step are shown in Fig. A.1. The four chips shown include single junctions, washer-type SQUIDs/Arrays, SQUIDs for measure stripline inductances, and a TFF circuit. The washer-type SQUID chip also contains single junctions for shunting experiments and planar DC SQUIDs.

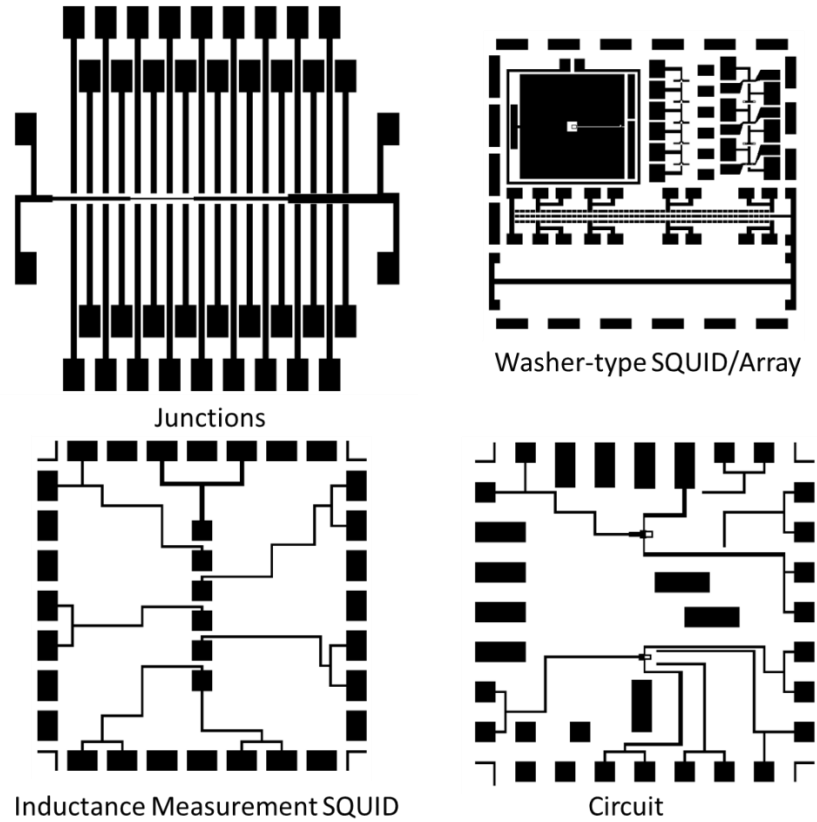


Figure A.1. First lithography step mask patterns.

6) First Ion milling Step.

- a) The recipe used calls for 600V and 200mA with 9 sccm Ar flow. The stage angle should be set 45° off normal for incident ions. Stage rotation should be turned on and stage chiller setpoint should be below 20°C . The milling rate of MgB_2 is about 25 nm/min. The milling rate of Au is about 40 nm/min. Typically the first

milling step of each is watched closely to better calculate milling times for the following steps.

- 7) Clean photoresist off of sample. Using a cotton-tipped applicator in a beaker of acetone, wipe the sample clear of photoresist. Make sure to only wipe in one direction. Use high power microscope to verify that all resist has been removed.
- 8) Second photolithography step. Follow recipe from step 5 for Photolithography to do the second patterning step. This will establish the junction area. Again, the four relevant mask patterns are shown in Fig. A.2.

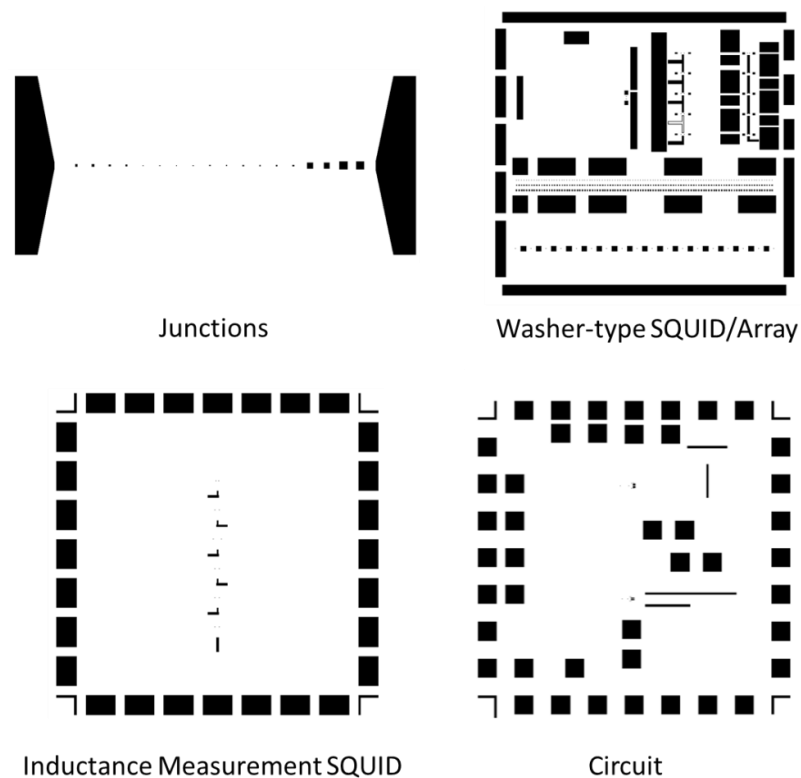


Figure A.2. Second lithography step mask patterns.

- 9) Second Ion milling step.
- a) This milling will be down to, but not through, the bottom MgB₂ layer. Make sure to utilize both the typical milling rate, and the milling time from the first ion milling step to make sure you are through the barrier, but do not leave the bottom electrode too thin.
- 10) Deposition of insulating layer. Using the same set up as the barrier deposition, deposit a thick layer (~80nm) of MgO. If the power is increased to 50W, the deposition time should be about one hour.
- 11) Lift off the photoresist.
- a) Clean the sample in acetone in the ultrasonic bath for 10-20 seconds to lift off the insulation from the junction area. If this is insufficient a cotton-tipped applicator can be used to wipe the sample as in step 7. Double check that all resist is gone using the high power microscope.
- 12) Third ion milling step.
- a) A 45'' milling step is required to remove the Au passivation layer so that an additional layer of MgB₂ can be added.
- 13) Deposit MgB₂ wiring layer.
- a) Follow procedure from step 1 to deposit another MgB₂ layer. This deposition will be for 1'20''. Make sure to remove any impurities (glue, resist) from the bottom of the sample prior to the deposition.
 - b) Skip this step for a Nb counter electrode. Au can be used as the wiring layer.
- 14) Deposit Au contact layer.

- a) Follow procedure from step 4 to deposit an Au layer to be used for bonding the sample to the chip carrier for measurement. The deposition time should be 2' for Au. Again a thin layer of Cr is needed for wetting.

15) Third photolithography step.

- a) This step establishes the wiring layer. The recipe is the same as previous photolithography steps. Alignment is most important (and difficult) in this step because your previous pattern is all covered with Au. The masks used are shown in Fig. A.3.

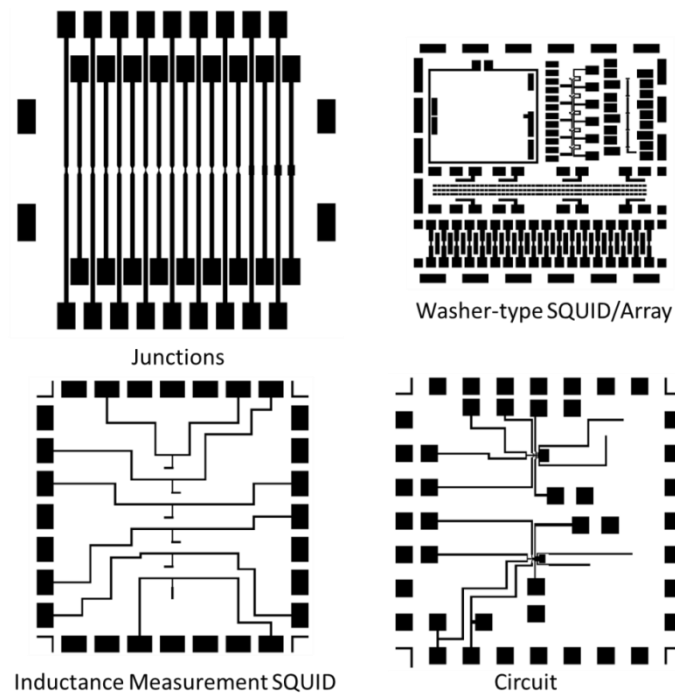


Figure A.3. Third and final lithography step mask patterns.

16) Final Ion milling step.

- a) This will mill the sample through the wiring layer and into the insulating layer.

Follow recipe from previous milling steps. Verify that the wiring layer is completely removed by measuring for conductance with a multi-meter outside the patterned region of your sample.

17) Remove Resist.

- a) Follow the procedure of step 7 to remove resist. Your sample is ready to be bonded and measured.